Paleoenvironmental Reconstructions of the Central Equatorial Pacific Ocean Using Uranium and Thorium Series Isotopes

Allison W. Jacobel

Submitted in partial fulfillment of the
requirements for the degree
of Doctor of Philosophy
in the Graduate School of Arts and Sciences

COLUMBIA UNIVERSITY

2017

ABSTRACT

Paleoenvironmental Reconstructions of the Central Equatorial Pacific Ocean Using Uranium and Thorium Series Isotopes

Allison W. Jacobel

Uranium and thorium isotopes are powerful and sensitive tracers of a wide range of oceanographic and environmental processes. This thesis makes use of these isotopes in deep sea sediments to reconstruct dust fluxes and deep ocean respired carbon storage over the last 350 kyr in the central equatorial Pacific. The paleoenvironmental information obtained through the application of these isotopes as proxies reveals important information about the Earth's ocean and atmosphere, and their connectivity on millennial and glacial-interglacial timescales.

In Chapter 1 of this thesis I introduce the proxies and principles employed in our paleoenvironmental reconstructions. Subsequently, the first section of this thesis explores the use of $^{230}Th_{xs,0}$-derived ^{232}Th fluxes as a proxy for aeolian dust deposition at three sites beneath the shifting Pacific Intertropical Convergence Zone (ITCZ). The new records presented here improve upon existing records of tropical Pacific dust fluxes by increasing the temporal resolution ~5 fold and adding almost an order of magnitude more data. Specifically, we reconstruct dust fluxes in two cores from 0-150 ka and from one core from 0-350 ka In addition to substantially improving constraints on tropical dust fluxes this work also utilizes the spatial transect of cores to infer past positions of the ITCZ on glacial-interglacial and millennial timescales. This proxy approach to reconstruct ITCZ position has only been applied and published once previously, in a relatively low-resolution study.

Chapter 2, entitled "Large deglacial shifts of the Pacific Intertropical Convergence Zone," presents evidence that the Pacific ITCZ experienced large shifts in latitudinal position, on millennial timescales during the penultimate deglaciation. The data resolve abrupt shifts in atmospheric circulation associated with deglaciation, in this case Termination II, at the

boundary between the full glacial marine isotope stage (MIS) 6 and the peak interglacial MIS 5. These shifts are significant in that they appear to have occurred at the same time as changes in the North Atlantic driven by Heinrich Stadial 11 and may have played an important role in pushing the climate system over the threshold for deglaciation. Indeed, this study is the first to show evidence of a millennial-scale ITCZ response at the time of the Heinrich Event 11 catastrophic iceberg discharge event. Additionally, the data point to the existence of a previously unidentified millennial peak in northern hemisphere dust abundance during the penultimate deglaciation.

In Chapter 3, "Climate-related response of dust flux to the central equatorial Pacific over the past 150 kyr," records of dust flux are used to provide strong evidence for an association between high latitude stadial events and tropical dust fluxes during the last 150 kyr. These high-resolution observations permit the drawing of conclusions about the meridional location of the Pacific ITCZ during six Greenland stadials. As with the shift of the ITCZ during Heinrich Stadial 11, these events were associated with perturbations of the interhemispheric thermal gradient and coincident movement of the ITCZ presents an important constraint on the sensitivity of the tropical atmosphere to high latitude perturbations.

The conclusions stemming from the interpretation of geochemical and paleoceanographic data presented in Chapters 2 and 3 are of broad relevance to a variety of geoscience disciplines that seek an understanding of the climate system. For example, these results confirm predictions made by modeling studies about the response of the ITCZ to high latitude climate forcing and provide an important new set of boundary conditions for modeling studies aimed at reconstructing changes in insolation forcing and tropical hydroclimate. The results show that paleo-reconstructions can constrain the magnitude of even abrupt ITCZ movement, demonstrating the potential to relate ITCZ changes to the magnitude of thermal forcing and to investigate thermal and hydrological components of other climate change events, past and future. Additionally, these results help improve understanding of the relationship between atmospheric dust abundance and climate, with implications for planetary albedo and micronutrient fertilization of the oceans.

The second portion of this thesis focuses on using authigenic uranium (aU) to reconstruct deep water chemistry with implications for paleocirculation. Chapter 4, "Repeated storage

of respired carbon in the equatorial Pacific Ocean over the last three glacial cycles," presents evidence that the Pacific was a significant reservoir for respired carbon during glacial periods over at least the last 350 kyr. This reconstruction is based on the precipitation of the redox sensitive metal uranium as a proxy for deep water oxygen concentrations. Because any change in oceanic storage of respiratory carbon must be accompanied by corresponding changes in dissolved oxygen concentrations, data reflecting bottom water oxygenation are of value in addressing questions of glacial carbon sequestration. The record reveals periods of deep ocean aU deposition during each of the last three glacial maxima. Export productivity data indicate these intervals are not associated with local productivity increases, indicating episodic precipitation of aU occurs in response to basin-wide decreases in deep water oxygen concentrations.

Not only does the aU record show the history of dissolved oxygen concentrations in the central equatorial Pacific, it also provides an opportunity for the reconciliation of records previously interpreted as incompatible with one another and with the storage of respired carbon. Synthesis of existing data suggests the existence of a 'floating' pool of respired carbon between 2 and 3.5 km depth in the equatorial Pacific. This hypothesis permits the interpretation of existing proxy data reflecting abyssal LGM circulation and carbon storage without invoking a glacial watermass geometry significantly different from present.

The new data and conclusions presented in Chapter 4 represent a significant advance in our understanding of where carbon was stored in the ocean during successive glacial periods. The perspective provided by the new aU time series is spatiotemporally unique and constitutes compelling evidence that hypotheses of marine carbon storage developed to explain the last glacial period are equally applicable to previous Pleistocene glacial periods.

The three studies presented in this thesis provide strong support for the utility of U and Th series isotopes in paleoenvironmental reconstructions. Not only does this work demonstrate the range of paleoclimatic proxy data that can be obtained from isotopes of U and Th, it also illustrates the value of interpretations derived from their analysis. The records presented here represent a substantial contribution to our knowledge of marine hydroclimate and ocean circulation over the last 350 kyr and motivate additional high-resolution paleoclimate work using isotopes of U and Th.

Table of Contents

List of Figures

List of Tables

Acknowledgments

Long before I ever took part in fieldwork or set foot in a laboratory I knew I wanted to be a scientist. As I meandered from biology to geology and finally to geochemistry many have helped to guide me and I am deeply grateful for their influence, support and encouragement.

The Lamont leg of my journey began before I even arrived, with the guidance of Louisa Bradtmiller who fostered my academic interest in climate science and encouraged me to pursue summer research and eventually graduate school. At Columbia I had the good fortunate to be advised by Jerry McManus whose calm reason and advice has helped me weather a storm or two, but perhaps more importantly, helped me to realize the seas are not always so furious as they may at first seem. I am grateful to Bob Anderson for shaping my interests with his unparalleled teaching, and for improving both my writing and science with his invaluable attention to both detail and the big picture. I am indebted to Gisela Winckler for the example she has set in her pursuit of challenging questions, her dedication to promoting collaboration and her generous mentorship. I am also thankful for the support of Marty Fleisher and Nichole Anest in the lab.

Of course no doctoral experience would be complete without fellow graduate students and in that group I have also found the best of friends. To Catherine Pomposi I am grateful beyond description. Her friendship has been the lifeblood of my graduate experience and my memories of the past five years are filled with her wisdom, humor, and enthusiasm for life. I owe thanks to Etienne Dunn-Siguoin for both his example of perseverance and his encouragement of culinary adventurism. I must also thank Yoni Goldsmith for being the most delightful foil I can imagine, and Jesse Farmer for camaraderie every step of the way. Finally, thanks to Karen Jackson for reminding me to come up for a breath of fresh air every once in a while.

For my family: Mum, Dad and Brian

Each of you has helped me with science in a different way: With the psychology, the practice and the perspective. This work would not have been possible without you and I cannot thank you enough for helping me reach this point.

Chapter 1

Introduction

The R/V Marcus G. Langseth undertook its inaugural coring cruise in May of 2012, spending a month mapping (Lyle et al., 2016) and sampling (Lynch-Stieglitz et al., 2015) the sediments of the central equatorial Pacific. The cruise was specifically focused on the Line Islands archipelago, a north-south trending chain of mid-Cretaceous to late Eocene volcanic ridges punctuated by atolls attributed to mid-plate hot spot activity (Schlanger et al., 1984) (Figure 1.1). The region was targeted for coring work because it is well placed to reconstruct the paleoceanographic history of the central equatorial Pacific, the marine Intertropical Convergence Zone (ITCZ) and the El Niño Southern Oscillation (ENSO). Crucially, the area's relatively shallow bathymetry is also conducive to the accumulation and preservation of carbonate-rich sediments (Lynch-Stieglitz et al., 2015) which are ideal for paleoceanographic work. This dissertation focuses on a subset of cores taken during the Line Islands cruise, representing a latitudinal transect composed of: ML1208-37BB (hereafter 37BB) at 7.04°N, 161.63°W and 2,798 m water depth; ML1208-31BB (31BB) at 4.68°N, 160.05°W and 2,857 m depth; and ML1208-17PC (17PC) at 0.48°N, 156.45°W and 2,926 m depth. These cores utilized in the studies detailed here were selected in part for their latitudinal span and in part because their accumulation rates and initial stratigraphies indicated that they would be appropriate for both millennial and glacial-interglacial reconstructions of paleoclimate and paleoceanography in the central equatorial Pacific.

This dissertation focuses on uranium and thorium series isotope work carried out on the three Line Islands cores in pursuit of two broad lines of inquiry. The first relates to records of equatorial dust flux and the information they reveal about millennial and glacial-

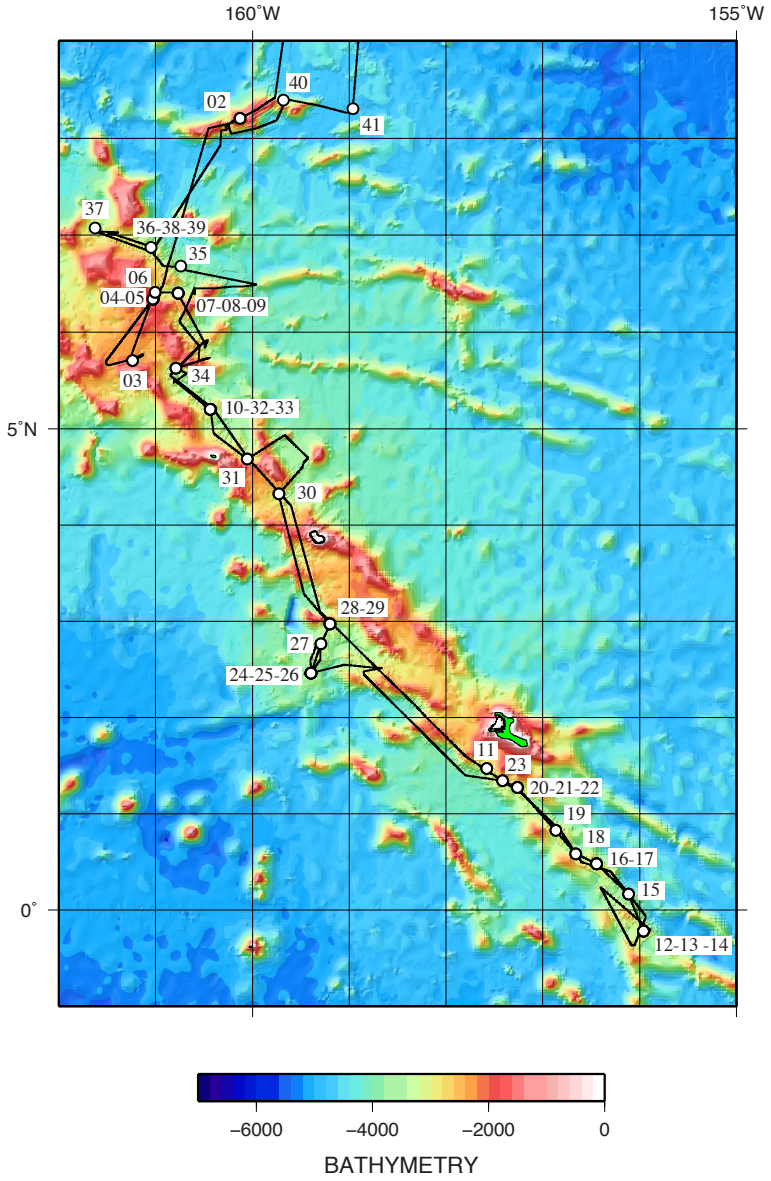

Figure 1.1: Bathymetric Map of the Line Islands Region with Core Sites Indicated

interglacial climate variability, and the insight dust fluxes can provide on the paleo-position of the ITCZ. Results from this work are contained in Chapters two and three which compose the first part (I) of this dissertation: Equatorial Pacific Dust Fluxes. The second part (II): Equatorial Pacific Deep-Water Chemistry, consists of a chapter focused on the record of marine respiratory carbon storage in the deep Pacific Ocean as preserved at the Line Islands. We use authigenic uranium (aU) as a proxy for porewater redox state to constrain oxygen limitation and, via its reciprocal relationship with respired carbon, to track deep water carbon sequestration on glacial-interglacial timescales over the last 350 kyr. Here, in this introductory Chapter 1, we provide background information about U/Th isotope systematics, aeolian dust, the ITCZ and the relationship between authigenic uranium and sedimentary redox state that underpin the subsequent chapters presented in Parts I and II.

1.1 Uranium and Thorium Isotope Systematics

The uranium (U) and thorium (Th) isotopes utilized in this work are the decay products of two primordial isotopes ^{238}U and ^{232}Th (Figure 1.2). Uranium-238 has a half life of 4.4683 ± 0.0024 billion years (Jaffey et al., 1971) and decays via alpha and beta decay to ^{234}U (with short-lived intermediate daughters ^{234}Th and ^{234}Pa). In turn,^{234}U has a half life of 245,620 ± 260 years (Cheng et al., 2013) and decays to ^{230}Th which has a half life of 75,585 ± 110 years (Cheng et al., 2013). The second primordial isotope of interest, ^{232}Th, is long lived with a half-life of 14.13 ± 0.13 billion years (Boehnke and Harrison, 2014), meaning that, on the timescales of relevance to this work, decay of this isotope is insignificant.

Thorium-230 is produced throughout the water column by the decay of its well-mixed parent ^{234}U (Bacon and Anderson, 1982). Unlike U, which behaves conservatively in oxygenated seawater, ^{230}Th is particle-reactive, causing it to be rapidly removed from solution via scavenging onto the surface of particles falling through the water column (Bacon and Anderson, 1982). Because the removal rate of ^{230}Th is fast relative to its half-life of 75.58 ± 0.11 ka (Cheng et al., 2013), the rate of ^{230}Th burial in sediments is approximately equal to its rate of production in the water column (β) (Francois et al., 2004). As a consequence of this behavior, the concentration of ^{230}Th in sediments, in excess (xs) of that supported

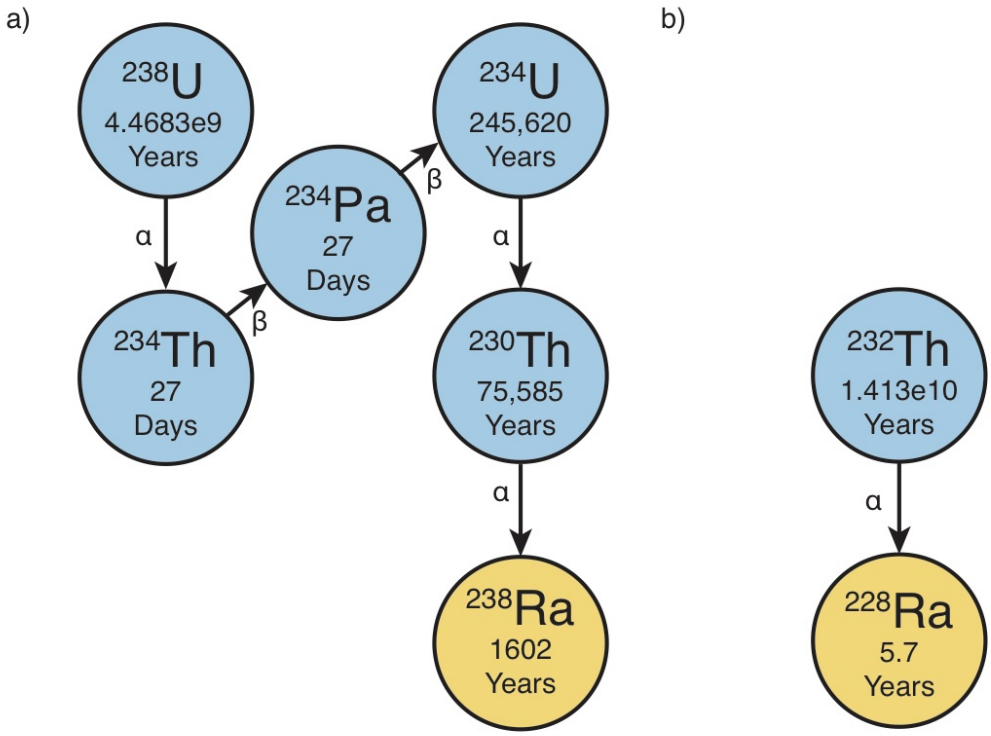

Figure 1.2: Uranium and Thorium Decay Systematics

by ^{238}U and its intermediate daughter ^{234}U, can be used to constrain the flux of particles to the seafloor. When calculating this excess we need to quantify and subtract the ^{230}Th present due to the decay of authigenic ^{238}U and ^{234}U (see below for information on authigenic uranium precipitation) and also the ^{230}Th of lithogenic (detrital) origin. This is done as follows:

$$^{230}Th_{xs} = ^{230}Th_{meas} - (0.7 * ^{232}Th) -$$
$$([^{238}U - 0.7 * ^{232}Th] *$$
$$[(1\text{-}e^{\lambda_{238} * t}) + \frac{\lambda_{230}}{\lambda_{230} - \lambda_{234}} * (e^{\lambda_{234} * t} - e^{\lambda_{230} * t}) * \frac{^{234}U}{^{238}U}_{sw} - 1])$$

with the ratio of ^{234}U to ^{238}U being that of seawater and all quantities representing isotope activities.

Because we measure the activity of ^{230}Th at some time after its deposition, we need to take into account its decay with time (t). This is done using the sediment core's age-depth model. We then apply the basic radioactive decay equation to determine the original activity of ^{230}Th$_{xs}$:

$$^{230}Th_{xs,0} = [^{230}Th_{xs} * e^{\lambda_{230} * t}]$$

The activity of ^{230}Th$_{xs,0}$ can subsequently be used to calculate mass flux history:

$$\text{Mass Flux} = (\beta * z)/(^{230}\text{Th}_{xs})$$

where β=0.00256 dpm m^{-3} yr^{-1} calculated using the concentration of ^{238}U in seawater (Owens et al., 2011) and the δ^{234}U of (Andersen et al., 2010), and z is the water depth above the site in meters. Thus, when the concentration of ^{230}Th is large, the mass flux is inferred to be small and vice versa. The ^{230}Th$_{xs,0}$ inventory integrated over the time period represented by a sedimentary interval will be close to the production rate in the overlying water column if no sediment redistribution has occurred. In contrast, when the observed ^{230}Th$_{xs,0}$ inventory is substantially greater (less) than that expected due to water column production, lateral sediment addition (removal), termed focusing (winnowing), is implicated (Suman and Bacon, 1989).

Thorium-232 is used in this study as a tracer of aeolian dust. Common thorium (so called because ^{232}Th is the most abundant isotope) is a component of continental crust

with a known range of concentrations (denoted here as γ) in dust source areas relevant for the present study (McGee et al., 2016). Because our core sites are far from landmasses from which ^{232}Th could be eroded by terrestrial weathering processes, the sole mechanism of ^{232}Th delivery to the Line Islands is as a constituent of windblown dust. Because the concentration of ^{232}Th in dust source regions has been analytically constrained (McGee et al., 2016) we can apply that relationship to determine the concentration of dust measured at our study sites. Here, as in other studies (Anderson et al., 2006; McGee et al., 2007; Winckler et al., 2008), dust fluxes based on ^{232}Th are evaluated by normalization to $^{230}\mathrm{Th}_{xs,0}$ (Francois et al., 2004) to account for dilution by changing fluxes of other sedimentary constituents.

$$\text{Dust Flux} = [(\beta * \text{z})/(^{230}\mathrm{Th}_{xs,0})] * {}^{232}\text{Th} * (1/\gamma)$$

Thorium-232 is also important for identifying the presence of authigenic uranium (aU) in sediments. Because the ratio of ^{232}Th to ^{238}U has been experimentally determined for terrestrial material likely to be integrated into deep-sea sediments, ^{238}U in excess of that expected must have been precipitated authigenically in the sediment column. Thus the aU fraction in the sediment can be determined using the known detrital ratio for the Pacific (Henderson and Anderson, 2003):

$$\text{aU} = [^{238}U - 0.7 *^{232} Th]$$

1.2 Aeolian Dust

Windblown mineral dust plays a critical role in the climate system through its alteration of radiative forcing, surface albedo, significance as cloud and ice condensation nuclei, and ability to enhance biological sequestration of carbon (see summary in Mahowald et al., 2014). Modeling studies focused on the last glacial maximum (LGM) have suggested that the radiative influence of dust is in the range of -1 W m^{-2} (Mahowald et al., 2006).

The flux of dust at a given depositional site represents a complex interplay of variables including, source area aridity, seasonality of aridity, vegetation cover, wind speed, wind gust speed, the supply of aeolian material (from erosion, glaciogenic activity, exposure of continental shelves), original particle size, rainout history and precipitation amount, with

some variables playing a larger role than others. While high resolution records of dust flux have been produced using ice cores from Greenland (Ruth et al., 2007) (to ~110 ka) and Antarctica (Lambert et al., 2012) (to ~800 ka), recent work has suggested that these records may be strongly overprinted by vapor removal signals as a consequence of strong temperature gradients between dust source areas and measurement sites (Markle et al., 2016). Because the tropics do not experience such strong rainout, as a consequence of generally increasing atmospheric moisture capacity, they are a reasonable area to reconstruct paleo dust fluxes in an attempt to differentiate dust abundance versus transport signatures. Previous work from the tropics has established the covariance between high and low latitude dust fluxes on glacial-interglacial timescales during the Pleistocene (Winckler et al., 2008) but questions remain about the hemispheric response of dust fluxes to millennial events, including those which occur predominately in the northern hemisphere.

Mineral dust is preferentially removed from the atmosphere in areas of high precipitation (Schlosser et al., 2014), such as those underlying the ITCZ. In Chapters 2 and 3 we take advantage of dust removal by ITCZ rainout to infer intervals of increased dustiness related to millennial events associated with abrupt Northern Hemisphere cooling. Because of the potential influence of ITCZ position on these records, our inferences are made using the dust fluxes observed at all three of the ML1208 sediment core sites discussed above, as well as the records of dust abundance from the high latitude northern and southern hemispheres.

1.3 The Intertropical Convergence Zone

The ITCZ is a band of intense precipitation, that migrates seasonally over the oceans, moving northwards in boreal summer and southwards in winter. The ITCZ forms where northern and southern hemisphere trade winds converge and atmospheric convection occurs. The mean position of the ITCZ is often identified as the latitude at which precipitation is at an annual maximum. On long timescales, the mean position of the ITCZ is responsive to the latitude of Earth's thermal equator (Schneider et al., 2014), with the ITCZ shifting towards the differentially warming hemisphere. The terrestrial expression of the ITCZ is integrally connected to the world's monsoon systems, which act as the life-blood for more than half

of Earth's population (Dykoski et al., 2005). Variations in monsoonal rainfall patterns and total amount of precipitation can thus have serious implications for communities that live in environments susceptible to flooding or drought. Indeed, some have suggested that rainfall variability on archaeological timescales was responsible for the turnover of dynasties in China (Dykoski et al., 2005) and even the collapse of civilizations, such as the Classical Maya (Hodell et al., 2005; Medina-Elizalde and Rohling, 2012).

Modern-day shifts in the ITCZ are closely observed, but much less is known about ITCZ position during climate states different from present. Understanding the causes of rain belt displacement and variations in intensity are important for predicting future variability, but unfortunately little quantitative information is available about the behavior of these complex atmospheric systems in the past. Several groups have reconstructed Asian Monsoon "strength" (Y. Wang et al., 2005; Yancheva et al., 2007) but these studies struggle to differentiate between true changes in monsoon strength, changes in the location of precipitation and changes in global aridity, making even simple predictive modeling efforts difficult. Moreover, authors have challenged the idea that these proxies record Asian Monsoon variability alone (Pausata et al., 2011), further complicating the interpretation of these records. Despite difficulties in clearly reconstructing the magnitude of past ITCZ movement, theory (e.g., Schneider et al., 2014), models (e.g., Chiang and Bitz, 2005; Chiang et al., 2003), and proxy reconstructions (e.g., Arbuszewski et al., 2013; X. Wang et al., 2007) suggest that the ITCZ has indeed migrated in response to perturbations of the energy balance between the hemispheres. Because the ITCZ efficiently scavenges aerosols from the atmosphere via cloud nucleation and wet deposition, reconstructing dust fluxes across a latitudinal transect beneath the shifting ITCZ can provide information about its past positions and thus movement. The location of our study site in the central equatorial Pacific allows us to constrain changes far from continental landmasses, avoiding complications presented by the spatial discontinuity of the ITCZ/Monsoon-complex over land. Additionally, our transect of sediment cores permits semi-quantitative estimation of changes in ITCZ position, providing valuable new information on the sensitivity of tropical convection to high latitude climate change.

1.4 Uranium and Sedimentary Redox State

In addition to providing useful information about the mass flux of sedimentary constituents, U-series isotopes can also act as valuable proxies for environmental conditions near the sediment-water interface on the sea floor. Authigenic U is precipitated from seawater as U(IV) under reducing conditions in sedimentary porewaters (Klinkhammer and Palmer, 1991). As a consequence of this sensitivity, the presence of aU in a sedimentary sequence is indicative of low oxygen conditions, which could be attributed to two mutually compatible environmental changes: 1) respiration of locally produced organic matter ($C_6H_{12}O_6 + 6O_2 \Leftrightarrow 6CO_2 + 6H_2O$) within the sedimentary column and/or 2) the presence of low-oxygen bottom water with a high respiratory CO_2 content (e.g., Jaccard et al., 2009). Although variability in either of these parameters could lead to the precipitation of aU, identifying which possibility is responsible for decreases in oxygen abundance can yield useful paleoceanographic information. For example, an increase in the abundance of settling organic matter is likely related to an increase in surface productivity driven either by enhanced upwelling (e.g., Dubois and M. Kienast, 2011), or increased nutrient concentrations in upwelled water (e.g., Winckler et al., 2016). In turn this variability might provide evidence about changes in surface winds or nutrient utilization at water mass source areas. Alternatively, a decrease in the oxygen content of deep water might reflect a decrease in deep ocean ventilation and a coincident overall increase in abyssal carbon storage related to ${}_pCO_2$ drawdown (Bradtmiller et al., 2010; Jaccard et al., 2009, 2010, 2016). Changes in any of these processes on millennial or orbital timescales can provide valuable information about the climate's response(s) to external forcing and help improve our understanding of Earth's coupled ocean-atmosphere system. Accordingly, Chapter 4 of this dissertation assesses the evidence for changes in the relative influence of organic carbon productivity versus deep ocean circulation on a record of aU spanning the last three glacial cycles (Jacobel et al., in revision).

Part I

Equatorial Pacific Dust Fluxes

Chapter 2

Large deglacial shifts of the Pacific Intertropical Convergence Zone

Note: A modified version of this chapter has been published in *Nature Communications* (2016), Vol. 7:10449, http://dx.doi.org/10.1038/ncomms10449 [1]

Abstract

The position of the Intertropical Convergence Zone (ITCZ) is sensitive to changes in the balance of heat between the hemispheres which has fundamental implications for tropical hydrology and atmospheric circulation. Although the ITCZ is thought to experience the largest shifts in position during deglacial stadial events, the magnitude of shifts has proven difficult to reconstruct, in part because of a paucity of high-resolution records, particularly those including spatial components. Here we track the position of the ITCZ from 150 to 110 ka at three sites in the central equatorial Pacific at sub-millennial time resolution. Our results provide evidence of large, abrupt changes in tropical climate during the penultimate deglaciation, coincident with North Atlantic Heinrich Stadial 11 (~136-129 ka). We identify this event both as a Northern Hemisphere increase in aeolian dust and as a shift in the mean position of the ITCZ a minimum of 4° southwards at 160°W.

[1]Authors: A.W. Jacobel[a*], J.F. McManus[a], R.F. Anderson[a] G.Winckler[a] [a] Department of Earth and Environmental Sciences, and Lamont-Doherty Earth Observatory of Columbia University, 61 Route 9W, Palisades, NY 10964, USA

* corresponding author: jacobel@ldeo.columbia.edu

2.1 Introduction

The Intertropical Convergence Zone (ITCZ) is a band of vigorous atmospheric convection and precipitation that varies position seasonally in connection with the latitude of maximum local insolation and on longer timescales in response to changes in the thermal equator (McGee et al., 2014; Schneider et al., 2014). This sensitivity has been reproduced in model experiments (Chiang and Bitz, 2005; Donohoe et al., 2013) and is indicated by a variety of palaeoclimate reconstructions covering the Last Glacial Maximum, last deglaciation and Holocene (Arbuszewski et al., 2013; Haug et al., 2001; X. Wang et al., 2007). Because the ITCZ monitors the hemispheric thermal balance, its past positions record the (a)symmetry of climate changes and can provide insight into the hemispheric origin of millennial and orbital climate events. As an active component of the global hydrological system, the ITCZ also propagates changes at high latitudes into the tropics by altering albedo, regional precipitation and wind fields (Seager et al., 2005). Understanding the forcings and dynamics behind these atmospheric shifts is important for predicting future changes in the ITCZ/monsoon complex with significant implications for communities living in hydrologically sensitive environments (Stager et al., 2011). On longer timescales, studies have suggested that the ITCZ may exert an influence on the positions of the Southern Hemisphere subtropical jet and westerly winds (Ceppi et al., 2013; Lee et al., 2011) which it is hypothesized are an essential element of deglacial Southern Ocean upwelling (Anderson et al., 2009). Accounting for past changes in ITCZ position is thus critical to our understanding of global ocean-atmosphere dynamics, tropical hydrology and the ocean's role in regulating atmospheric ${}_pCO_2$.

As expected, given the role of ITCZ precipitation in scavenging particles from the atmosphere, previous work has found that Pacific Ocean core sites underlying the ITCZ display a latitudinal gradient in dust flux (McGee et al., 2007) and provenance (Pichat et al., 2014; Xie and Marcantonio, 2012). When the amount of suspended dust is the same, greater precipitation yields more dust to the underlying sediments and therefore relative dust flux can be used as a proxy for ITCZ position. Specifically, the edges of the ITCZ will have higher dust fluxes than sites within the ITCZ due to lower residual dust availability towards the interior of the ITCZ (McGee et al., 2007). However, it is essential to recognize that a

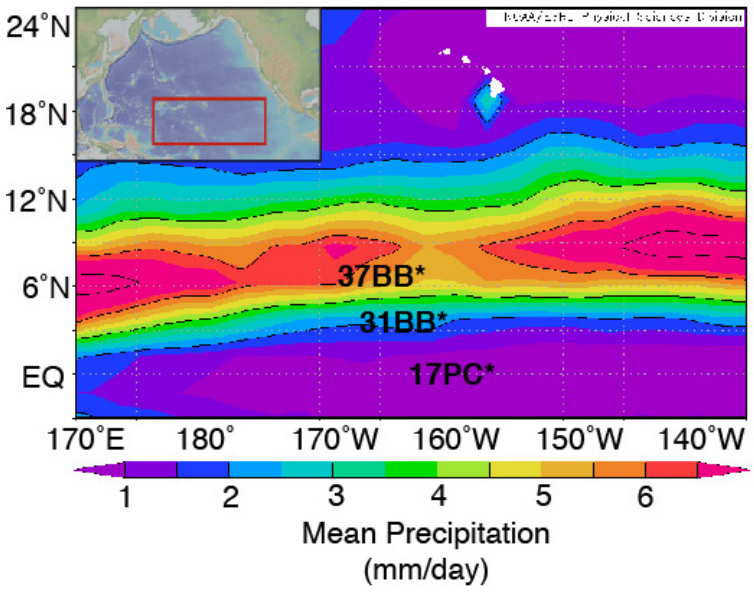

Figure 2.1: ML1208 core sites 37BB, 31BB and 17PC (black stars) are shown relative to Hawaii (white islands), and the modern mean annual position of the ITCZ, illustrated by the maximum mean annual precipitation in mm per day (coloured contours). Inset shows the location of this map (red rectangle) in the broader context of the Pacific Ocean. Basemap generated using the global precipitation climatology product (GPCP) version 2.2 from National Oceanic and Atmospheric Administration's (NOAA) Physical Sciences Division, Earth System Research Laboratory. Inset generated in GeoMapApp.

site exhibiting a temporal maximum in dust flux does not necessarily mean that the ITCZ has moved over that site, since the amount of suspended dust is not always the same above all core sites. Because the ITCZ is a barrier to cross-hemispheric dust transport (Husar et al., 1997; Xie and Marcantonio, 2012), variations in ITCZ latitude can force substantial changes in the provenance and amount of dust above a site. This nuance requires that we use independent dust flux data, in this case from Antarctica (Lambert et al., 2008), to inform our interpretations. Combined with our latitudinal transect and attention to relative dust flux variations between core sites, this approach allows us to differentiate between changes in atmospheric dust abundance and shifts in ITCZ position.

The central equatorial Pacific's Line Islands are well positioned to be sensitive to changes

in the ITCZ because at this longitude the precipitation structure is well defined, with little deflection due to continental effects. Our records are derived from a latitudinal transect of three sediment cores: ML1208-37BB (37BB) at 7.04°N, 161.63°W and 2,798 m water depth; ML1208-31BB (31BB) at 4.68°N, 160.05°W and 2,857 m depth; and ML1208-17PC (17PC) at 0.48°N, 156.45°W and 2,926 m depth (Figure 2.1). Core 37BB is located near the local modern boreal summer maximum of the ITCZ (~7 N), and 17PC is south of the local boreal winter minimum of ~5°N (Adler et al., 2015).

We present high-resolution records of dust flux from 150 to 110 ka at three sites in the Line Islands to constrain the ITCZ position during the penultimate deglaciation (Termination II or TII). These records place latitudinal constraints on the millennial scale movement of the Pacific ITCZ over this time period. Our data reconstruct a large, abrupt change in tropical Pacific climate over TII, characterized by both an increase in atmospheric dust abundance and by a shift of the ITCZ of at least 4° southwards.

2.2 Results

2.2.1 Sedimentation rates

Sedimentation rates vary between cores and within cores with average rates for the interval studied (110-150 ka) of 1.1, 4.8 and 3.0 cm ka^{-1} for cores 37BB, 31BB and 17PC respectively. A higher level of confidence is placed on conclusions when the sedimentation rate is higher, notably for the deglacial interval key to our primary interpretations in this paper. Details on the development of the age models from which these sedimentation rates are derived may be found in the methods section.

2.2.2 Dust flux data

Dust fluxes were reconstructed using $^{230}Th_{xs,0}$-normalized ^{232}Th fluxes as described in Methods. Data for sites 37BB, 31BB and 17PC (Figure 2.2b) show similar trends in time from Marine Isotope Stage (MIS) 6 through MIS5. During MIS6 (oldest part of record to ~140 ka) all cores show high dust deposition (>0.25 g m^{-2} yr^{-1}) relative to the interglacial. At the peak glacial (as marked by the maxima in oxygen isotope values; Figure 2.2a) the

northernmost core is the first to show a small increase in dust flux, followed by the two more southerly cores between ~136 and 135 ka. Deglacial dust flux maxima occur in cores 31BB and 17PC between ~133.4 and 134.5 ka, and after that values in all cores decline precipitously reaching a minimum (0.1 to 0.15 g m^{-2} yr^{-1}) during the MIS5 interglacial. This interglacial dust flux value is ~2.5 times lower than glacial values. For the remainder of the records all three cores show gradually increasing dust fluxes.

2.2.3 Oxygen isotope data

Oxygen isotope data generated on the planktonic foraminifera *Globigerinoides ruber* in ML1208 cores (Figure 2.2a) have been published elsewhere (Lynch-Stieglitz et al., 2015), but here we provide additional interpretation of these data in the context of our inferences about MIS6-5. Planktonic oxygen isotope ($\delta^{18}O$) data record a combination of surface water conditions including ambient temperature, salinity and the global $\delta^{18}O$ of sea water. These variables in turn reflect changes in sea-surface temperature, local precipitation, upwelling and global ice volume. Variations in $\delta^{18}O$ may reflect either local processes or the signature of waters advected to our study sites, or a combination of both. Although we cannot parse the contributions of each of these variables to observed changes in the records, it is instructive to consider the relationship between $\delta^{18}O$ data from the three cores and how it changes over time.

From 150 and 140 ka, oxygen isotope values for cores 37BB and 31BB are between 1.28 and 0.8‰, representing substantially fresher or warmer conditions than at site 17PC (0.5 to 0.02‰). As the deglaciation begins (~140 ka) $\delta^{18}O$ values freshen and warm at all three sites in response to rising global temperatures and reduced ice volume. However, during HS11 (136-129 ka), site 17PC shows the largest change (1.07‰), indicating that freshening and/or warming was most strongly felt at the southernmost site. At the peak of MIS5e (~120 ka), the $\delta^{18}O$ recorded by foraminifera at sites 37BB, 31BB and 17PC is similar.

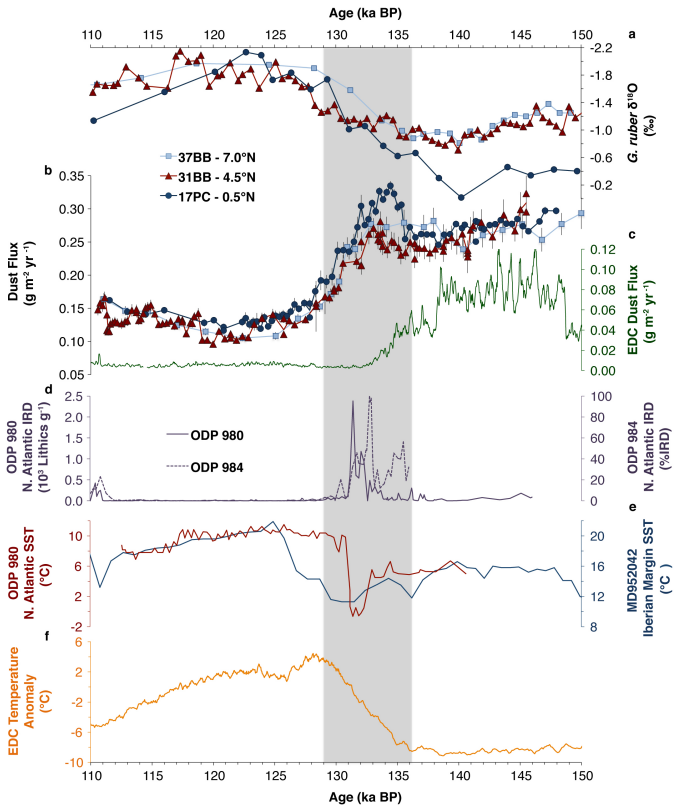

Figure 2.2: Planktonic foraminifera δ^{18}O stratigraphy for cores 37BB (light blue squares), 31BB (red triangles) and 17PC (navy circles) (Lynch-Stieglitz et al., 2015) **(a)**. Dust flux records from 37BB, 31BB and 17PC. Symbols as in panel a, error bars are 2 s.d. Lines connect data points and the mean value of replicates. **(b)**. Dust flux from Antarctic ice core EDC (Lambert et al., 2008) (75°06'S, 123°21'E) on AICC2012 chronology (Veres et al., 2013) (5pt smoothed) **(c)**. North Atlantic ice rafted debris (IRD) abundance from sites ODP 980 (55°29'N, 14°42'W) and ODP 984 (61°25'N, 24°4'W) (Mokeddem et al., 2014) **(d)**. North Atlantic temperature proxy records from ODP 980 (Oppo et al., 2006) on the timescale of (Mokeddem et al., 2014) (red line) and MD952042 (Pailler and Bard, 2002) (navy blue) **(e)**. Antarctic EDC temperature anomaly record (Jouzel et al., 2007) on AICC2012 chronology (Veres et al., 2013) (5pt smoothed), where the anomaly is relative to the last 1000 yrs **(f)**. Grey shading represents Weak Monsoon Interval II (WMI-II) (Cheng et al., 2009) correlated with HS11 in the North Atlantic. Principles underlying the interpretation of proxies in e and f are discussed in Section 2.5.3.

2.3 Discussion

Few dust flux records exist from the central equatorial Pacific, but a low-resolution record from TT013-72PC (72PC) at 0.1°N, 139.4°W (Anderson et al., 2006; Winckler et al., 2008) provides an important comparison for our sediment cores. Data from 72PC show a similar decrease in dust flux from 145 to 118 ka, followed by an increase from 118 to 110 ka, in agreement with our results. Given the paucity of high-resolution marine dust flux records covering TII, the Antarctic EPICA Dome C (EDC) dust record is a valuable companion data set (Figure 2.2c). Antarctic and equatorial dust fluxes co-vary at coarse resolution between hemispheres during the late Pleistocene ice-age cycles (Winckler et al., 2008), and in this context it is the differences between our high-resolution records and the EDC record that are the most significant. Specifically, the decline in EDC dust flux at the MIS5/6 boundary (TII at ~134 ka; from ~0.036 to 0.007 g m^{-2} yr^{-1}) trends oppositely to the increase in dust flux observed at sites 37BB, 31BB and 17PC during HS11 (grey shading in Figure 2.2). Because of the relatively high resolution of the EDC ice core and a comparable decline in dust flux in at least one other high-resolution, Southern Hemisphere record (Martínez-Garcia et al., 2014), we hypothesize that the absence of a HS11 dust peak in the ice core record indicates that the observed dust peak in the central equatorial Pacific does not reflect an increase in global or Southern Hemisphere dust abundance, but rather an increase in northern hemisphere sources alone. Independent behaviour of Northern and Southern Hemisphere dust sources has been repeatedly observed for Heinrich stadials over the last glacial cycle (Lambert et al., 2008; Ruth et al., 2007) (Figure 2.4c, d), and we propose that a similar hemispheric dust flux asymmetry characterized TII during HS11. Although no high-resolution dust records exist from the Northern Hemisphere covering HS11, we suggest that the increase in Northern Hemisphere dust that marked previous Heinrich stadials also characterized HS11 (McGee et al., 2010), especially since the relatively long duration of HS11 (Marino et al., 2015) would likely have allowed for the full expression of stadial conditions. Other indicators of stadial conditions have also identified HS11, including high ice-rafted debris (IRD) abundance in North Atlantic sediments (Figure 2.2d) and cold sea-surface temperatures (Figure 2.2e). While not causally related to dust fluxes, these stadial indicators are repeatedly seen to change in concert with increases in Northern Hemisphere

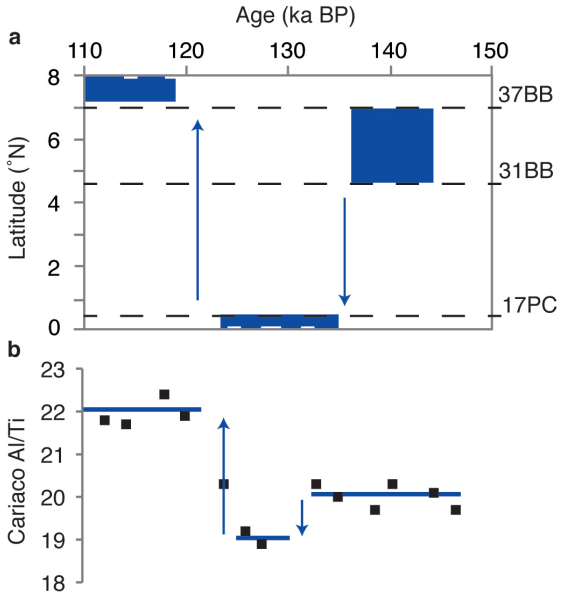

Figure 2.3: Blue boxes indicate range of possible latitudes of the mean ITCZ position, black dashed lines denote core latitudes **(a)**. Cariaco Basin Al/Ti record (black squares) (Yarincik et al., 2000) with blue bars indicating estimates of the relative ITCZ position through time **(b)**.

dust abundance. Recurrent intervals of high dust flux during Heinrich stadials, in combination with the clear evidence for decreased dust abundance in the Southern Hemisphere, strongly support the idea that the dust flux increases in our central equatorial Pacific cores are due to a Northern Hemisphere dust increase.

Although atmospheric dust abundance clearly varies on deglacial timescales, it cannot explain the time-variant differences in dust flux among our three sites. Instead, we attribute inter-core differences to changes in the position of the ITCZ (Figure 2.3a). Our interpretations of ITCZ movement take into account our new dust flux records, planktonic oxygen isotope data from the same three sites, variations in Southern Hemisphere dust abundance as recorded in Antarctica (Lambert et al., 2008) and temperature proxy records that indicate the thermal gradient between poles (Figure 2.2e, f and Section 2.5.3).

During MIS6 (~145 ka) dust fluxes at the three sites do not show a sufficiently clear relationship to infer confidently, on dust flux data alone, the position of the ITCZ. Instead

we suggest that the similar oxygen isotope values seen at sites 37BB and 31BB indicate an ITCZ positioned approximately equidistant between the two cores. Fresher conditions at these two sites would be consistent with ITCZ-derived precipitation located directly above the sites. Colder and/or more saline conditions at 17PC are also consistent with this interpretation, as cross equatorial winds could have driven enhanced upwelling at this southernmost site as they do seasonally at present when the ITCZ is at its northernmost position (Koutavas and Lynch-Stieglitz, 2004).

Between ~136 and 135 ka, coincident with the onset of HS11 in the North Atlantic (grey bar Figure 2.2), dust fluxes increase in 31BB and 17PC, which we interpret as indicative of a southward shift in the northern edge of the ITCZ. Because dust fluxes decrease in the Southern Hemisphere from 138.5 ka into MIS5, and because an increase in dustiness is repeatedly associated with Heinrich stadials, increasing dust fluxes in cores 31BB and 17PC indicate that they are likely receiving dust from the Northern Hemisphere. Since the ITCZ acts as a barrier to dust, the observed dust increases at 31BB and 17PC imply that the ITCZ must have been south of both of these sites. Additional evidence for an ITCZ south of 0.48 N during HS11 comes from contrasting the 24% increase in dust flux at the southernmost site (17PC), with the record from the intermediate core (31BB); this shows only a 9% increase, despite a higher sedimentation rate in core 31BB during this interval of ~3.9 cm ka^{-1} relative to a rate of ~2.9 cm ka^{-1} in core 17PC over the same time interval (see Methods). These increases in dust flux represent mean values for a range of data points before HS11 and during the dust flux maximum, with a maximum change in core 17PC of 32% and a minimum of 15%, and a maximum for core 31BB of 21% and a minimum of 1%. Here more efficient dust scavenging at 17PC suggests that the northern edge of the ITCZ was closer to that site, since at this time the source of dust to all three cores was most likely in the Northern Hemisphere. The hemispheric thermal gradient (Section 2.5.3) supports this interpretation, as it shows rapid, deglacial Antarctic warming at a time when North Atlantic foraminifera assemblages and alkenone unsaturation indices record cold sea-surface temperatures (cf. Figure 2.2e, f). This millennial-scale response of the ITCZ to changes in the hemispheric thermal gradient is consistent with models that predict ITCZ shifts in response to North Atlantic Heinrich stadials (Chiang and Bitz, 2005).

Planktonic oxygen isotope data from the three sites are consistent with our inference of a southward-shifted ITCZ during the deglaciation. All three cores show a shift towards values indicating warmer, fresher conditions, but the change is largest at 17PC where a southward-shifted ITCZ may have warmed that site and/or more ITCZ precipitation may have freshened surface waters. In contrast, sites 31BB and 37BB experienced more muted freshening and warming over this time period as might be expected if the δ^{18}O signal from decreasing precipitation opposed the effect of warming deglacial temperatures and decreasing ice volume.

The small lag in the onset of dust flux increases in cores 31BB and 17PC relative to the onset of HS11 is likely an artefact of uncertainty in our age models (see Methods) and we therefore do not interpret this offset as a climate system lag. Interestingly, core 37BB does not appear to show an increase in dust flux coincident with the records from our other two cores. We suggest two possible reasons for this observation. First, core 37BB may be seeing relatively little dust deposition during this otherwise high-dust-abundance time period. Because it would lie significantly (~7°) north of the ITCZ at this time, it is possible that dust is inefficiently scavenged from the air column above the site. Alternatively, it could be that core 37BB experienced a significant increase in dust flux during HS11, an increase that has been subsequently obscured due to relatively lower accumulation rates and the effects of bioturbation (Sections 2.5.1 and 2.5.2).

Dust levels remain above the interglacial baseline in the southernmost core until ~126 ka, which could indicate that the ITCZ was in its southernmost position until that time. However, we suggest that it is more likely that the ITCZ actually began to shift northwards around 129 ka when dust fluxes dropped below pre-stadial values, coincident with interglacial warming with stronger warming in the Northern Hemisphere. Our data display a slightly longer duration of HS11, probably due to the smoothing effects of bioturbation. This would cause HS11 to appear longer in our dust records than reconstructed from other proxies such as speleothems (Cheng et al., 2009), which have better age control and higher resolution but do not directly record dust fluxes or shifts in the ITCZ.

During MIS5e, all three cores record a decrease in dust flux to minimum values between 123 and 119 ka. On the basis of near--dentical dust flux data for the two more northerly

cores 37BB and 31BB, we suggest that at MIS5e the ITCZ was northwards of 7 N and that it was not influencing any of our sites during the peak interglacial. Planktonic oxygen isotope values which are indistinguishable at the three sites during MIS5e, are consistent with this argument, as an ITCZ located north of all three cores would be unlikely to differentially influence surface hydrography or temperature at any of the three sites. It is notable that after the ITCZ retreats northward during MIS5e that the δ^{18}O at site 17PC does not show a 0.8‰enrichment relative to cores 37BB and 31BB, as it did during the peak of MIS6. As suggested previously by the work on a larger set of ML1208 δ^{18}O records (Lynch-Stieglitz et al., 2015), this could be due to differences in the salinity of water carried by the North Equatorial Counter Current during glacial versus interglacial times. If the North Equatorial Counter Current carried fresher water from the western Pacific warm pool during MIS6 than during MIS5, a larger δ^{18}O gradient would be predicted between equatorial and more northerly cores.

Our interpretation of an ITCZ located north of 7°N during MIS5e is consistent with a strong hemispheric thermal gradient, with the North Atlantic experiencing peak warmth at this time. At the end of MIS5e (~119 ka) interglacial temperatures subsided in both hemispheres and dust fluxes began to rise, but the differential rate of cooling appears to have been small enough that the ITCZ was not displaced southward of 37BB, since 37BB and 31BB show comparable dust fluxes to the end of our record at 110 ka.

Only one other record of ITCZ movement exists for the penultimate deglaciation, a record of variations in the Al/Ti ratio from the Cariaco Basin (Yarincik et al., 2000). The Cariaco Basin records ITCZ-driven changes in terrestrial runoff with higher (lower) ratios indicating more (less) runoff and therefore a relatively more northerly (southerly) ITCZ (Figure 2.3b). Given that the Cariaco record is interpreted as recording relative movement of the terrestrial ITCZ, the agreement between our data sets is noteworthy and is consistent with the idea that ITCZ movement is likely coherent across large distances (Schneider et al., 2014) even on short timescales.

Model reconstructions of past ITCZ migrations have been challenging in part because of the sensitivity of the ITCZ to small changes in cloud feedbacks and energy balances (Schneider et al., 2014). Here we have shown that palaeo reconstructions can constrain the

magnitude of even abrupt ITCZ movement, demonstrating the potential to relate ITCZ changes to the magnitude of thermal forcing and to investigate thermal and hydrological components of other climate change events. Our results provide evidence that an abrupt, millennial climate oscillation was a prominent feature of the penultimate deglaciation, both at high and low latitudes. During HS11, in concert with North Atlantic cooling (Oppo et al., 2006), ice rafting (J. F. McManus et al., 1999), increases in northern hemisphere dust abundance, and a shift in the interhemispheric thermal gradient (Oppo et al., 2006; Parrenin et al., 2007), the ITCZ migrated southwards by at least 4° relative to MIS6, and 6.5° south of its present latitude. This shift likely had significant consequences for global atmospheric circulation (Ceppi et al., 2013) and could thus have contributed to tipping the climate system over the threshold for deglaciation.

2.4 Methods

2.4.1 Age model development and uncertainty

Age-depth relationships for cores ML1208-37BB, 31BB and 17PC were developed on the basis of planktonic oxygen isotope stratigraphies (Lynch-Stieglitz et al., 2015) tied to the LR04 benthic stack (Lisiecki and Raymo, 2005), with the assistance of a modified Monte-Carlo-enabled cross-correlation maximization scheme and random walk algorithm (MonteXCM) (Hoffman et al., 2015). A record of coeval planktonic and benthic oxygen isotopes values was previously reconstructed in the Eastern Equatorial Pacific (Lea et al., 2006), which showed zero offset between the timing of deglaciation in the two stratigraphies. This observation gives us confidence that our use of planktonic oxygen isotope stratigraphies is not introducing a significant systematic bias into the timing of our events relative to data from the ice cores.

The use of the random walk algorithm in MonteXCM allows us to quantify age uncertainty at each data point. On average, over the interval studied, 2 s.d. uncertainties are 1.5, 1.5 and 1.7 ka for cores 37BB, 31BB and 17PC, respectively. Specifically, for the HS11 interval (129-136 ka), uncertainties are ~1.3, 1.4 and 1.4 ka for the same three cores. The magnitude of these uncertainties means that it is probable that the small offsets in event

timing observed between our three sediment cores are artefacts of the age model and do not represent true differences in the timing of the reconstructed dust flux changes or ITCZ shifts. However, our age constraints are sufficient to indicate that it is unlikely that these events are temporally disconnected, and a lag between the onset of HS11 and our inferred initiation of tropical changes is not inconsistent with the interpretations we present.

2.4.2 Dust flux reconstruction

We reconstruct dust fluxes through the quantification of $^{230}Th_{xs,0}$-normalized ^{232}Th fluxes in marine sediments, which act as a proxy for dust flux (Anderson et al., 2006; McGee et al., 2007; Winckler et al., 2008). Terrestrial sediments contain ^{232}Th at a mean concentration of 10.7 p.p.m., which varies 1 p.p.m. or less over a range of dust provenance (McGee et al., 2007). A more recent summary of ^{232}Th concentrations in dust source areas found evidence that the fine fraction (<5 mm) of dust samples from a range of provenance had ^{232}Th concentrations closer to 14±1 p.p.m. (McGee et al., 2016). We note that changing the ^{232}Th concentration used to reconstruct dust fluxes would decrease the absolute magnitude of the dust fluxes reconstructed at our study sites but does not alter our interpretations. As our core locations are a great distance from continental sources of lithogenic material, we expect ^{232}Th at our sites to be delivered predominately by aeolian processes. Indeed, grain size analyses show that the average size of lithogenic sediments at ~1°N 131°W is 3.1 μm (Rea and Hovan, 1995), unlikely to have been derived from hemipelagic sedimentation. Here, as in other studies (Anderson et al., 2006; McGee et al., 2007; Winckler et al., 2008), dust fluxes based on ^{232}Th are evaluated by normalization to $^{230}Th_{xs,0}$ (Francois et al., 2004).

2.4.3 Uranium and thorium geochemistry

Sediment samples from ML1208-37BB, 31BB and 17PC were analysed for uranium and thorium isotopes by isotope dilution and inductively coupled plasma mass spectrometry (Element XR, ICP-MS) at the Lamont-Doherty Earth Observatory of Columbia University. Between 100 and 200 mg of sediment per sample was spiked with ^{236}U and ^{229}Th before sediment dissolution and digestion with HNO_3, $HClO_4$ and HF (Fleisher and Anderson,

2003). Anion-exchange column chemistry was also used to isolate the U/Th fraction (Kraus et al., 1956).

Samples were run with an external in-house standard (mirroring the physical and geochemical properties of our samples) to determine measurement reproducibility, yielding relative s.d.s of 0.74% for ^{238}U 1.94% for ^{230}Th and 0.87% for ^{232}Th. Background contamination was evaluated in each run via blanks, which were spiked and digested, but contained no sediment. Results show ^{238}U blanks (0.4 ng), ^{230}Th blanks (0.009 pg) and ^{232}Th blanks (1.1 ng) all of which are <1% of even the lowest sample values. Errors reported in Figure 2.2 represent 2 s.d. uncertainty estimates unique to each sample, including the propagated error due to uncertainty in counting statistics, mass bias corrections (from measurements of a natural ^{238}U/^{235}U standard), counting gain corrections, spike measurements, the lithogenic fraction (0.7±0.1) (Bradtmiller et al., 2010) and a 1% age uncertainty. The average s.d. of replicate dust flux values is ~6.4% of sample values. Samples for which dust flux values differed from a same-depth replicate, or an average of four nearest-neighbour data points by more than 4 s.d., have been excluded from the data set. The number of data points excluded using this method is <5% of the total number of data points reported.

2.4.4 Data archiving

Line Islands dust flux data are archived at the National Oceanic and Atmospheric Administration National Centers for Environmental Information (NCEI) database.

2.5 Supplementary Notes

2.5.1 Age model development and uncertainty

Age-depth relationships for cores ML1208-37BB, 31BB and 17PC were developed on the basis of planktonic oxygen isotope stratigraphies (Lynch-Stieglitz et al., 2015) tied to the LR04 benthic stack (Lisiecki and Raymo, 2005) with the assistance of a modified, Monte-Carlo-enabled cross-correlation maximization scheme and random walk algorithm (MonteXCM) (Hoffman et al., 2015). A record of coeval planktonic and benthic oxygen isotopes values was previously reconstructed in the Eastern Equatorial Pacific (Lea et al., 2006) which showed

zero offset between the timing of deglaciation in the two stratigraphies. This observation gives us confidence that our use of planktonic oxygen isotope stratigraphies is not introducing a significant systematic bias into the timing of our events relative to data from the ice cores. The use of the random walk algorithm in MonteXCM allows us to quantify age uncertainty at each data point. On average, over the interval studied, 2 s.d. uncertainties are 1.5, 1.5 and 1.7 ka for cores 37BB, 31BB and 17PC respectively. Specifically, for the Heinrich Stadial 11 (HS11) interval (129-136 ka), uncertainties are approximately 1.3, 1.4 and 1.4 ka for the same three cores. The magnitude of these uncertainties means that it is probable that the small offsets in event timing observed between our three sediment cores are artifacts of the age model and do not represent true differences in the timing of the reconstructed dust flux increase and ITCZ shift. However, our age constraints are sufficient to indicate that it is unlikely that these events are temporally disconnected and a lag between the onset of HS11 and our inferred initiation of tropical changes is not inconsistent with the interpretations we present in the main text.

2.5.2 Effect of bioturbation on ML1208 dust flux records

Open ocean sediment accumulation rates vary widely in response to local geography, bathymetry, bottom current activity, surface productivity, water column dissolution and many other variables. Other variables held constant, higher sedimentation rate regions are typically considered more ideal for paleoceanographic reconstructions, as cores can be sampled at higher resolution with lower amounts of signal disturbance due to bioturbation. Benthic and infaunal organisms moving along and burrowing into the ocean floor cause stochastic mixing of surrounding sediments, known as bioturbation. The cumulative effect of these actions is that, on a small scale, individual sediment constituents do not necessarily adhere strictly to laws of chronographic superposition. The effect of bioturbation on a sediment core can be modeled as a diffusive process (Boudreau, 1994) whereby proxy values at a given depth represent a combination of values at, above and also below that depth (Ruddiman and Glover, 1972). When the amount of bioturbation is the same, the smoothing effect is greater on cores with lower sedimentation rates. Several studies have attempted to quantify the length scale of bioturbation but the results vary greatly depending on the measure-

ment method, season of measurement, faunal assemblage present (Teal et al., 2008) and organic content of the sediment (Ruddiman and Glover, 1972). Despite these challenges, considering the effects of bioturbation can be important for interpreting climate data as the precise timing, character and even frequency (Goreau, 1980) of events can be altered by this post-depositional processes. Bioturbation is likely an important process in sediment cores from the productive Line Islands region and should be considered when interpreting the changes in dust flux values between our three sediment cores. Given the geographic proximity and comparable water depths of the three ML1208 sites in this study, we make the assumption that these cores experienced similar rates of bioturbation. Thus, for the same magnitude of proxy change in all three cores (for example the dust flux increase during HS11), the core with the highest sedimentation rate (31BB) would be expected to retain a larger event signal than a lower sedimentation rate core (such as 37BB or 17PC). This effect of bioturbation is particularly important for our interpretations at HS11 because the core that records the largest dust flux excursion during HS11 (17PC) is not the highest sedimentation rate core. This suggests that the magnitude of the event at site 17PC was truly larger than at site 31BB (which has a higher sedimentation rate by ~1.0 cm ka^{-1}, supporting our inference that the ITCZ was likely closer to site 17PC during HS11.

2.5.3 Interpretation of the hemispheric thermal gradient

The ITCZ has been shown to vary its position in response to seasonal shifts in the temperature contrast between hemispheres and on longer timescales in response to changes in solar forcing (Schneider et al., 2014). Typically, the ITCZ is positioned at the latitude where the atmospheric energy flux changes sign from positive to negative (Schneider et al., 2014), that is where one branch of the Hadley circulation transports energy southwards and the other transports energy northwards. When one hemisphere is warmer, heat is transported from that hemisphere into the cooler hemisphere with the latitude of zero heat flux located in the warmer hemisphere. The larger the temperature difference between the hemispheres, the higher the latitude of the thermal equator. Specifically in this study, this would indicate that the warmer the southern hemisphere relative to the northern hemisphere, the further southwards the ITCZ.

Other than estimates of the position of the ITCZ, no paleo record exists which reveals the integrated thermal relationship between Earth's hemispheres. However, comparing temperature records from each of the poles allows us to roughly approximate this balance through time. Ideally, this comparison would be made using the same proxy at comparable northern and southern hemisphere latitudes. Ice core records would be preferable since the conventional interpretation of deuterium isotopes (δD_{ice}) is directly related to surface temperature (Jouzel et al., 2007). For the southern hemisphere we use a record of δD_{ice} from the Antarctic EPICA Dome C ice core (Jouzel et al., 2007). Unfortunately, Greenland's ice core records do not currently extend to the penultimate deglaciation (Termination II) so another proxy is required. Here, we use two proxies, a North Atlantic reconstruction of sea surface temperatures (SSTs) using the modern analogue technique (MAT) (Oppo et al., 2006) and another reconstruction of SSTs from the Iberian Margin derived from alkenones (Pailler and Bard, 2002). These are imperfect proxies for comparison to Antarctic surface temperatures but nonetheless provide a useful first-order constraint on the relative magnitudes and rates of warming in the two hemispheres. A more nuanced quantification of the magnitude of thermal forcing expressed during the penultimate deglaciation and its relationship to ITCZ position/shifts would be valuable, particularly for modeling efforts, but is beyond the scope of this paper. Despite their spatio-temporal limitations, the records from the northern and southern hemispheres presented in Figure 2.2 panels e and f, are in agreement with our ITCZ interpretations, as the sense of movement is entirely consistent with the large-scale changes in the thermal balance between hemispheres.

Our argument for the out of phase deglacial temperature variations in the North Atlantic and southern hemisphere during MIS6-5 is strengthened by the similar pattern associated with Termination 1 (Figure 2.4 panel a). During both deglaciations Antarctic temperatures began to rise while the North Atlantic and Greenland remained cold (Figure 2.4 panels a and b, and Figure 2.2 panels e and f). An increase in seasonal sea ice cover likely further decreased winter temperatures and may have led to iceberg rafting which delivered IRD (Figure 2.2 panel d and Figure 2.4 panel e) and freshwater to the North Atlantic (Barker et al., 2015). Other authors have previously observed these and other parallels between the last two deglaciations (Cheng et al., 2009) so while coincident behavior of interhemispheric

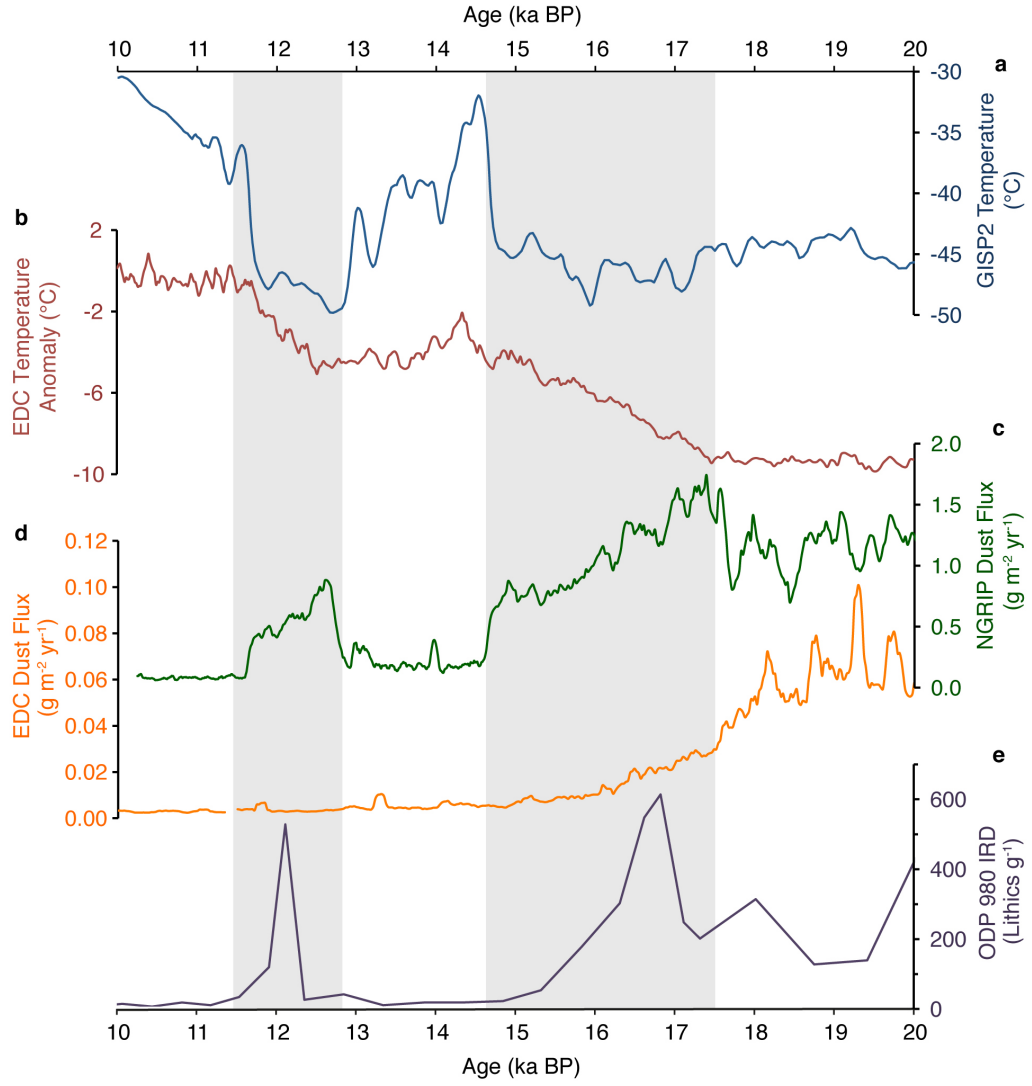

Figure 2.4: Greenland GRIP (72°35'N 37°38'W) temperature record (3pt smoothed)(Alley, 2000) **(a)**. Antarctic EDC (75°06'S, 123°21'E) temperature anomaly (relative to the last 1,000 yrs) on AICC2012 chronology (5pt smoothed) (Jouzel et al., 2007; Veres et al., 2013) **(b)**. Greenland NGRIP (75°05'N, 42°19'W) dust flux on AICC2012 chronology (5pt smoothed) (Ruth et al., 2007; Veres et al., 2013) **(c)**. Antarctic EDC dust flux on AICC2012 chronology (5pt smoothed) (Lambert et al., 2008; Veres et al., 2013) **(d)**. North Atlantic ODP 980 (55°29'N, 14°42'W) ice rafted debris (IRD) abundance (J. F. McManus et al., 1999) **(e)**. Grey shading indicates the Younger Dryas and Heinrich Stadial 11 (Y. J. Wang et al., 2001).

temperature patterns is not a new finding, the millennial scale influence of the thermal balance on ITCZ position during Termination II is a striking observation.

2.6 Acknowledgements

We thank the core repository at Lamont-Doherty Earth Observatory for providing samples, Marty Fleisher for assistance in the lab and R. Jacobel for helpful discussions. Special thanks to Jeremy Hoffman whose generous assistance with the MonteXCM algorithm improved ML1208 age models and permitted robust quantification of chronostratigraphic uncertainty. We also wish to acknowledge the contributions of Jean Lynch-Stieglitz, Pratigya Polissar, and the ML1208 science party, including the planning for and collection of the sediment cores used in this study. The manuscript was improved through the thoughtful comments of Sylvain Pichat and two anonymous reviewers. This research was funded in part by an award from the US National Science Foundation AGS-1502889 (J.F.M. and G.W.), and benefited from previous support from NSF OCE-1003374, OCE-1159053, and OCE-1158886, and the Comer Science and Education Foundation.

Chapter 3

Climate-related response of dust flux to the central equatorial Pacific over the past 150 kyr

Note: A modified version of this chapter has been published in *Earth and Planetary Science Letters* (2017), Vol. 457, pp 160-172 http://10.1016/j.epsl.2016.09.042 [1]

Abstract

High resolution paleoclimate records from low latitudes are critical for understanding the role of the tropics in transmitting and generating feedbacks for high-latitude climate change on glacial-interglacial and millennial timescales. Here we present three new records of $^{230}Th_{xs,0}$-normalized ^{232}Th-derived dust fluxes from the central equatorial Pacific spanning the last 150 kyr at millennial-resolution. All three dust flux records share the "sawtooth" pattern characteristic of glacial-interglacial cycles in ice volume, confirming a coherent response to global climate forcing on long timescales. These records permit a detailed examination of millennial variability in tropical dust fluxes related to abrupt perturbations in oceanic and atmospheric circulation. Increases in dust flux in association with at least six of the longest Greenland stadials provide evidence that abrupt, high-latitude climate oscillations

[1]Authors: A.W. Jacobel[a*], J.F. McManus[a], R.F. Anderson[a] G.Winckler[a] [a] Department of Earth and Environmental Sciences, and Lamont-Doherty Earth Observatory of Columbia University, 61 Route 9W, Palisades, NY 10964, USA

* corresponding author: jacobel@ldeo.columbia.edu

influenced the atmospheric aerosol load in the equatorial Pacific, with implications for both direct and indirect effects on the tropical energy balance. Our latitudinal transect of cores captures shifts in the position of the Intertropical Convergence Zone (ITCZ) in response to variations in the interhemispheric thermal gradient associated with cooling in Greenland and bipolar seesaw warming in Antarctica. These observations demonstrate that changes in the energy and hydrologic balance of the tropics were repeated features of the penultimate deglaciation, last glacial inception and last glacial cycle, and highlight the role of the tropical atmosphere as a dynamic and responsive component of Earth's climate system.

3.1 Introduction

Windblown mineral dust plays a critical role in the climate system through its alteration of radiative forcing, surface albedo, significance as cloud and ice condensation nuclei, and ability to enhance biological sequestration of carbon (review in Mahowald et al., 2014). Long, high-resolution records of mineral dust flux exist from sites in Antarctica (Lambert et al., 2012) and Greenland (Ruth et al., 2007), but no equivalent reconstructions exist from the tropics where the atmospheric load of dust can be especially important due to high incoming solar radiation and large convective potential. Previous work has reconstructed dust fluxes in the tropics at low resolution (Anderson et al., 2006; McGee et al., 2007), and has been critical in establishing that global dust fluxes demonstrate coherent cyclicity over at least the last 500 kyr (Winckler et al., 2008). Despite these advances, the temporal and spatial resolution of existing tropical dust flux records has limited our ability to draw conclusions about low latitude climate responses and feedbacks. For example, the identification of millennial stadial events in equatorial dust fluxes has been challenging due to insufficient data resolution. Abrupt dust flux changes that would be smoothed out by bioturbation in low sedimentation rate environments, or hidden in noisy proxy reconstructions are important for interpreting the far-field implications of high latitude climate shifts with significant consequences for tropical radiative balance. Additionally, although geographically proximal dust flux reconstructions have the potential to inform our understanding of spatially variable dust removal processes, the temporal span of such records is limited (McGee et al., 2007).

Multiple archives yielding proxy data with high temporal resolution and a low signal to noise ratio have the potential to reveal information about regional climate variability. The value of this type of approach was recently demonstrated using dust flux records to identify major shifts in tropical hydrology at the termination of the penultimate glacial period (Jacobel et al., 2016). Reconstructing records of tropical dust fluxes over glacial cycles at sub-millennial scale resolution is important as we try to understand linkages between high and low latitude climate and the mechanisms of climate forcing and feedbacks. In tropical ocean basins, far from continental sources, the most important removal mechanism for dust is wet deposition by the Intertropical Convergence Zone (ITCZ), which efficiently scavenges particles from the atmospheric column (McGee et al., 2007; Schlosser et al., 2014) and acts as a barrier to interhemispheric dust transport (Pichat et al., 2014; Xie and Marcantonio, 2012). The mean position of the ITCZ is often identified via satellite imagery as the latitude at which precipitation, and consequently wet-deposition of aerosols (Schlosser et al., 2014), is at an annual maximum. The ITCZ forms where northern and southern hemisphere trade winds converge and convection occurs. On long timescales, the mean position of the ITCZ is responsive to the latitude of Earth's thermal equator (Schneider et al., 2014) with the ITCZ shifting towards the differentially warming hemisphere. This behavior has been demonstrated in model simulations and paleoclimate reconstructions for glacial-interglacial climate shifts (Arbuszewski et al., 2013; Chiang et al., 2003), abrupt stadial events (Chiang and Bitz, 2005; Jacobel et al., 2016; X. Wang et al., 2004), and even changes during the historical period arising from hemispherically asymmetric aerosol loading (Ridley et al., 2015). This interplay of forces influencing ITCZ position adds complexity that makes a simple determination of ITCZ sensitivity to thermal perturbations difficult, hindering our predictive capabilities.

Addressing questions about past ITCZ shifts and their causes is important not only in establishing the range of responses to asymmetric climate forcing, but also because perturbations of the ITCZ may act to alter global atmospheric circulation patterns. Modeling work has shown that changes in ITCZ latitude influence the position of the Southern Hemisphere Westerlies (Lee et al., 2011), a key component of the Southern Ocean deglacial upwelling hypothesis (Anderson et al., 2009). Recent work has indicated that a southward shift of the

Pacific ITCZ at least 4.5 degrees south of its present day latitude accompanied the deglacial stadial event that punctuated the penultimate deglaciation (~150-120 ka) (Jacobel et al., 2016). This shift of the ITCZ may have driven significant changes in global atmospheric circulation patterns, contributing to the conditions required for deglaciation. In sum, existing evidence suggests the position of the ITCZ is a key indicator of and intermediary player in global climate change, making long, high spatiotemporal resolution records of its behavior essential in developing a comprehensive picture of past climate. Here we present high-resolution records from a latitudinal transect of three sediment core sites in the central Equatorial Pacific to constrain ITCZ movement and position via the quantification of dust fluxes from the penultimate deglaciation, through the last glacial inception, last glacial maximum and last deglaciation. Our records are the first to constrain equatorial Pacific dust fluxes at sub-millennial resolution over this entire time period, allowing us to examine the sensitivity of both tropical dust fluxes and the ITCZ to a range of perturbations, occurring over a variety of timescales. Here we focus our discussion on the last glacial inception and the last glacial period ~120-20 ka, as we have previously considered the penultimate deglaciation at high resolution (Jacobel et al., 2016) and a detailed comparison of the last two deglaciations (Terminations I and II) is forthcoming (Jacobel, in prep.).

3.2 Study Area, Sediment Cores and Age Models

Three cores were selected for this study, forming a north-south transect in the central equatorial Pacific (cruise ML1208) (Figure 3.1). All cores were taken near the Line Islands archipelago, a north-south trending chain of atolls. Core ML1208-37BB (hereafter 37BB) was recovered from 2,798 m of water at 7.04°N, 161.63°W, core ML1208-31BB (31BB) from 2,857 m of water at 4.68° N, 160.05°W and core ML1208-17PC (17PC) at 0.48°N, 156.45°W from a water depth of 2,926 m. Core sediments are composed primarily of foraminifer sands with correspondingly high calcium carbonate content. Site 37BB is located near the maxima in mean annual precipitation associated with the modern ITCZ (~7°N) (at 160°W), site 31BB is just south of both the boreal winter and mean annual precipitation maxima,, and site 17PC is consistently south of the seasonally shifting ITCZ (Figure 3.1). Age models

for the cores (Figure 3.11) are based on G. ruber (planktonic) foraminifera δ^{18}O isotope stratigraphies and radiocarbon dates (Lynch-Stieglitz et al., 2015), a portion of which were newly obtained for this study (Section 3.8.1 and 3.1). Planktonic isotope stratigraphies were used to constrain chronologies beyond the range of radiocarbon via tuning to the LR04 benthic stack (Lisiecki and Raymo, 2005) using MonteXCM (Hoffman et al., 2015), making these chronologies distinct from those previously published by (Lynch-Stieglitz et al., 2015). MonteXCM is a modified Monte-Carlo-enabled cross-correlation maximization scheme coupled with a random walk algorithm to assign age-depth relationships at control points based on the statistical match between the input data (planktonic δ^{18}O) and a target chronology (the LR04 stack) within the analytical uncertainties of both data sets. Age control points from MonteXCM were passed into Bchron's 'Bchronology' function (Haslett and Parnell, 2008) to better constrain the age uncertainty associated with each data point using the Compound Poisson-Gamma chronology model available in Bchron. Resulting age model uncertainties average 4.1, 2.8 and 4.6 ka for 37BB, 31BB and 17PC respectively (2 sigma). Because each age model is developed independently from the others, small offsets between the timing of dust flux events exist between the records. However, we have no reason to suspect that these differences represent significant lead or lag relationships between the three sites and attribute these apparent differences to the uncertainties inherent in our age models. Unless otherwise noted, ice core data used for comparison are presented on the AICC2012 age model (Veres et al., 2013). General comments on the significance of accumulation rate differences and bioturbation in the ML1208 cores can be found in Section 3.8.2 while interval-specific details are in Section 3.6.2, where the signatures of millennial events are discussed and interpreted.

3.3 Proxies and Application

3.3.1 ^{232}Th as an aeolian dust proxy

In this study we employ $^{230}Th_{xs,0}$-normalized ^{232}Th fluxes as a proxy for dust accumulation at our sites. Lithogenic sediments have been shown to contain ^{232}Th at average concentrations of 10.7 ppm varying 1 ppm or less over a wide range of provenance (McGee et al., 2007)

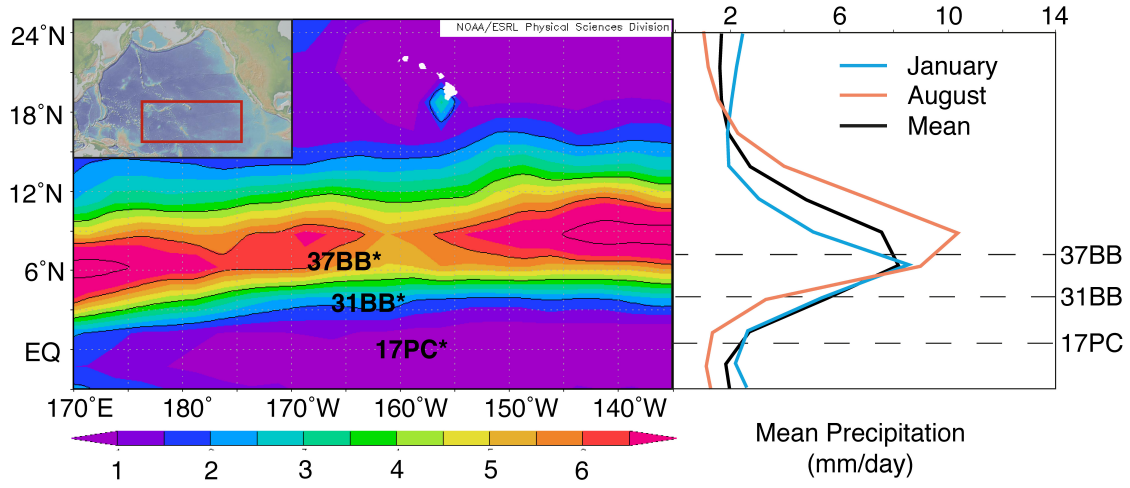

Figure 3.1: ML1208 core sites 37BB, 31BB and 17PC (black stars) are shown relative to Hawaii (white islands), and mean annual precipitation in mm per day (colors) at left of figure. Inset shows the location of this map (red rectangle) in the broader context of the Pacific Ocean. Panel at right indicates the mean annual distribution of precipitation (black line) at 160°W as well as the long term mean precipitation during the months of January (blue line) and August (orange line). Basemap generated using the global precipitation climatology product (GPCP) version 2.2 and histograms generated using Climate Prediction Center long term mean data, both from National Oceanic and Atmospheric Administration's (NOAA's) Physical Sciences Division, Earth System Research Laboratory. Inset generated in GeoMapApp. Figure and caption modified from Jacobel et al., 2016.

including those areas likely to be sources for our sites (Section 3.8.3). The quantification of $^{230}Th_{xs,0}$-normalized ^{232}Th fluxes as a terrestrial dust proxy is also supported by work that demonstrates a tight correlation between ^{232}Th and terrigenous ^{4}He (McGee et al., 2016; Winckler et al., 2005).

3.3.2 $^{230}Th_{xs,0}$ normalization

Sediment mass accumulation rates and dust fluxes were evaluated by normalization to $^{230}Th_{xs,0}$ (Francois et al., 2004) (Section 3.8.4 and references therein). The fundamentals underlying the use of $^{230}Th_{xs,0}$-normalization to account for dilution and post-depositional sediment changes have been the subject of much research and debate, with recent work suggesting that $^{230}Th_{xs,0}$ may be problematic for reconstructions of coarse fraction mass accumulation rate (MAR) in areas where focusing factor corrections are large (Lyle et al., 2014). Our study avoids the potential pitfalls identified by these authors because we use $^{230}Th_{xs,0}$ to normalize ^{232}Th concentrations and both isotopes reside predominately in the fine fraction.

3.3.3 Dust flux as a proxy for ITCZ position

Open ocean $^{230}Th_{xs,0}$-normalized ^{232}Th records the flux of aeolian dust. Mineral dust is preferentially removed from the atmosphere in areas of high precipitation, like those underlying the ITCZ. Observations of ocean chemistry in the tropical Atlantic Ocean show a linear correlation between ITCZ precipitation and dissolved iron from mineral dust (Schlosser et al., 2014). Existing paleorecords confirm that sites within the ITCZ are characterized by latitudinal gradients in dust flux (McGee et al., 2007) and provenance (Reimi and Marcantonio, 2016; Xie and Marcantonio, 2012). Thus, we can use the scavenging of dust by the ITCZ to determine its position, taking into consideration that dust at the northern edge of the ITCZ will be primarily sourced from the Northern Hemisphere (NH) and that which is deposited at its southern edge will be predominately sourced from the Southern Hemisphere (SH). Here, we compare our equatorial dust flux records to independent records of dust flux from Greenland, the Southern Ocean, and Antarctica. These records, combined with our latitudinal transect approach, allow us to differentiate between changes in atmospheric dust

abundance and changes in ITCZ position.

3.4 Methods

A total of 604 samples from cores 37BB, 31BB and 17PC (109, 286 and 209 respectively) were analyzed for uranium and thorium by isotope dilution and inductively coupled plasma mass spectrometry on an Element 2 ICP-MS at the Lamont-Doherty Earth Observatory of Columbia University. For each sample 100 to 200 mg of sediment was spiked with ^{236}U and ^{229}Th prior to dissolution and digestion using HNO3, HClO4 and HF (Fleisher and Anderson, 2003). Anion exchange column chemistry was used to isolate the U and Th fractions from the bulk digestate (Kraus et al., 1956). Samples were run with an internal sediment standard to determine measurement reproducibility (n=29), yielding relative standard deviations of 2.7% for ^{238}U, 2.3% for ^{230}Th and 3.7% for ^{232}Th. Background contamination was evaluated in each run via blanks that were spiked and carried through column chemistry, but contained no sediment. Results show ^{238}U blanks (0.3 ng), ^{230}Th blanks (0.09 pg) and ^{232}Th blanks (0.8 ng), values that are smaller than 1.2% of even the lowest sample values. Errors reported in the figures represent 2 sigma uncertainty specific to each sample, including the propagated error due to uncertainty in counting statistics, mass bias corrections, counting gain corrections, spike measurements and uncertainty in the fraction of sediment that is lithogenic in origin (Francois et al., 2004).

3.5 Results

3.5.1 Mass accumulation rates

Data used to derive ^{232}Th-based dust fluxes are presented in Figure 3.2 for each of our three new sediment core records. Variations in $^{230}\mathrm{Th}_{xs,0}$based mass flux are displayed in panel 2 (a) and account for changes in the rain of particulate matter from the surface after correcting for sediment focusing and winnowing (Section 3.8.5). The data display both millennial variability and long-term changes in sedimentation, but mass fluxes vary similarly between the three core sites, with fluxes highest at the equator and decreasing with increasing

latitude. This pattern is as expected given enhanced organic and calcareous productivity associated with equatorial upwelling. The importance of flux-normalizing concentration data is readily illustrated by a comparison of Figure 3.2 (b) with (c), demonstrating that mass flux normalization removes sedimentary effects which might otherwise create the false impression of differences between the magnitude of dust deposition between cores and within cores. The value and significance of the mass flux correction is especially evident in 37BB in which ^{232}Th concentrations approach values twice the magnitude reconstructed in the other two cores. Higher concentrations of ^{232}Th at site 37BB are due primarily to the lower rain of biogenic particles that dilute the dust concentration there less compared to other sites. Normalization to $^{230}\mathrm{Th}_{xs,0}$ corrects the ^{232}Th concentration for variable dilution by biogenic phases, which contain negligible amounts of ^{232}Th.

3.5.2 Dust fluxes

Reconstructed dust fluxes show the largest amplitude changes on 100 kyr timescales in all three sediment cores, with smaller but well-resolved oscillations on millennial time scales occurring during both glacial and interglacial periods Figure 3.3. The highest dust fluxes are observed during glacial MIS 2, 4 and 6 (29-14, 71-57 and 191-130 ka respectively), and the lowest fluxes are recorded during interglacial MIS 1 and 5 (14-0 and 130-71 ka respectively). Dust fluxes increase through the glacial inception (~115 ka), continue to increase slowly through the remainder of MIS 5, rise sharply during MIS 4 and then experience a termination-like decrease from MIS 4 into MIS 3. Indeed, early MIS 3 dust fluxes are at less than full glacial levels, although still greater than MIS 5. Dust fluxes rise somewhat into MIS 2 and then decline during glacial Termination (T) I as they do during TII at the end of MIS 6. All three cores indicate that MIS 4 was as dusty or dustier than MIS 2, with some variability in the amount of dust present at MIS 4 relative to MIS 6.

Superimposed on this orbital variability are millennial changes in dust flux including (1) an increase in dust flux at the time of Heinrich Stadial (HS) 11 (~136-129 ka) (most notably in 17PC and 31BB), (2) small but coherent and well-resolved oscillations in dust flux at 31BB from ~109.3-103.7, 114.1-109.3 and 121.0-117.1 ka, and (3) an increase in dust flux between approximately 93 and 81 ka in cores 31BB and 17PC with a "late"

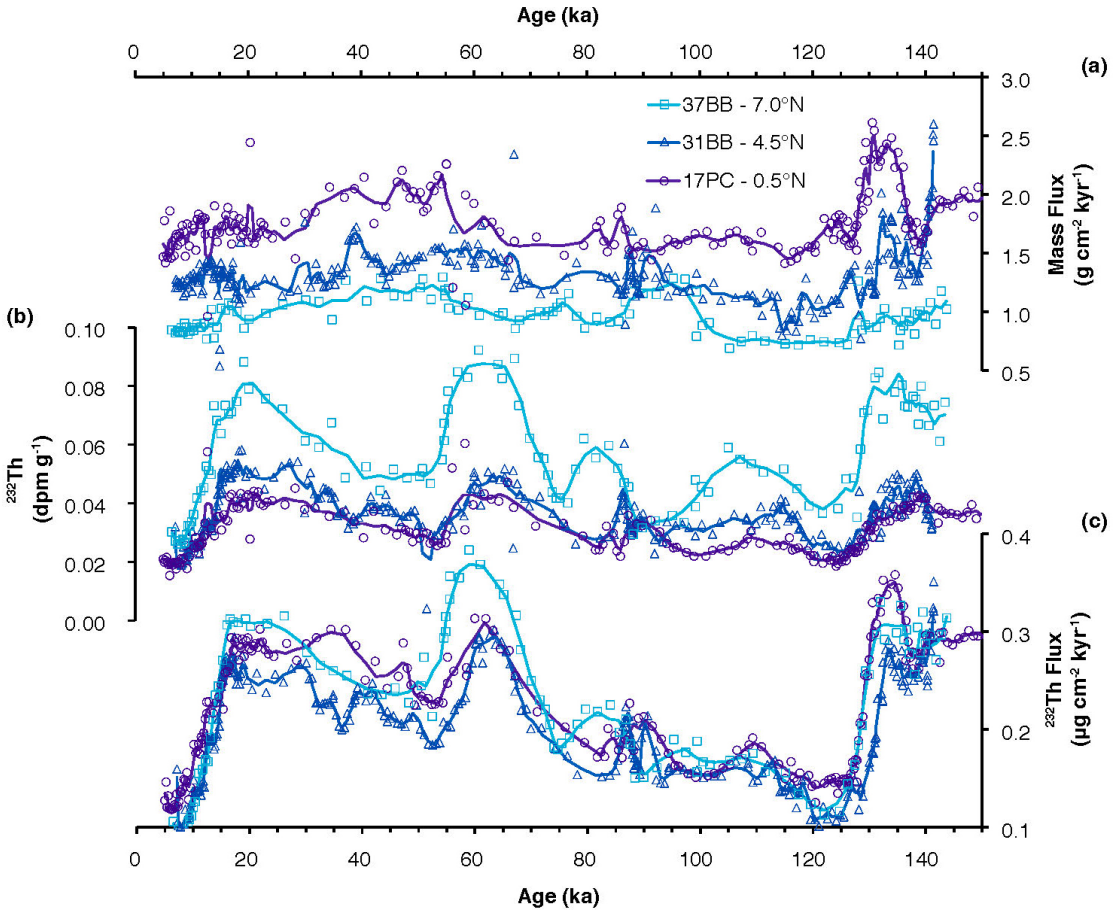

Figure 3.2: Mass flux (a), ^{232}Th activity (b) and ^{232}Th flux (c) data from sites 37BB (teal squares), 31BB (blue triangles) and 17PC (purple circles). Lines (matching colors) represent values after the application of a 3-point, 1st order Savitsky-Golay filter.

intensification in dust fluxes at 37BB from ~88 to 74 ka. Some of these events are visible only at the highest sedimentation rate site (31BB) possibly due to bioturbation elsewhere, lower sediment accumulation rates, or to the barrier effects of the ITCZ on cross convergence zone dust transport. These alternatives will be evaluated in detail in Section 3.6.5.

Because our analytical uncertainty is smaller than the differences between our three records at several intervals over the 150 kyr record, we are also able to examine spatial gradients in dust flux across our section Figure. 3.4c. High HS11 dust fluxes in the equatorial core 17PC have previously been discussed (Jacobel et al., 2016), so here we focus on the data from 120 ka to the last glacial maximum. Most notably, during MIS 4 significantly higher dust fluxes are observed at 37BB, the northernmost and lowest sedimentation rate site, relative to those at 31BB or 17PC. An average of the three highest MIS 4 dust flux values at each site shows that fluxes at 37BB are 20% higher than at 31BB and 16% higher than at 17PC.

3.6 Discussion

3.6.1 Coherent glacial-interglacial variability

Previous studies have noted a strong covariance on long timescales between equatorial Pacific dust fluxes, Antarctic dust fluxes and global ice volume (as reconstructed by the LR04 benthic stack), using this observation to suggest that dust generation processes in each hemisphere respond similarly to global climate changes over at least the last 500 kyr (Winckler et al., 2008). Here, a comparison of our new data to highly resolved records of dust flux from Greenland (Ruth et al., 2007) and Antarctica (Lambert et al., 2012) Figure 3.4, as well as the Southern Ocean (Anderson et al., 2014) (Figure 3.6e), are consistent with this observation. Broadly, the glacial-interglacial pattern of dust fluxes shows low interglacial dust fluxes with glacial dust fluxes ~3 times higher. Although this correlation is striking, it does not directly illuminate the element(s) of global climate variability driving changes in the dust flux. In a comprehensive review of the drivers of glacial dustiness, McGee and coauthors suggest that the most important factor may be increased wind gustiness which is dependent upon meridional thermal gradients and increased high and mid latitude seasonality (McGee

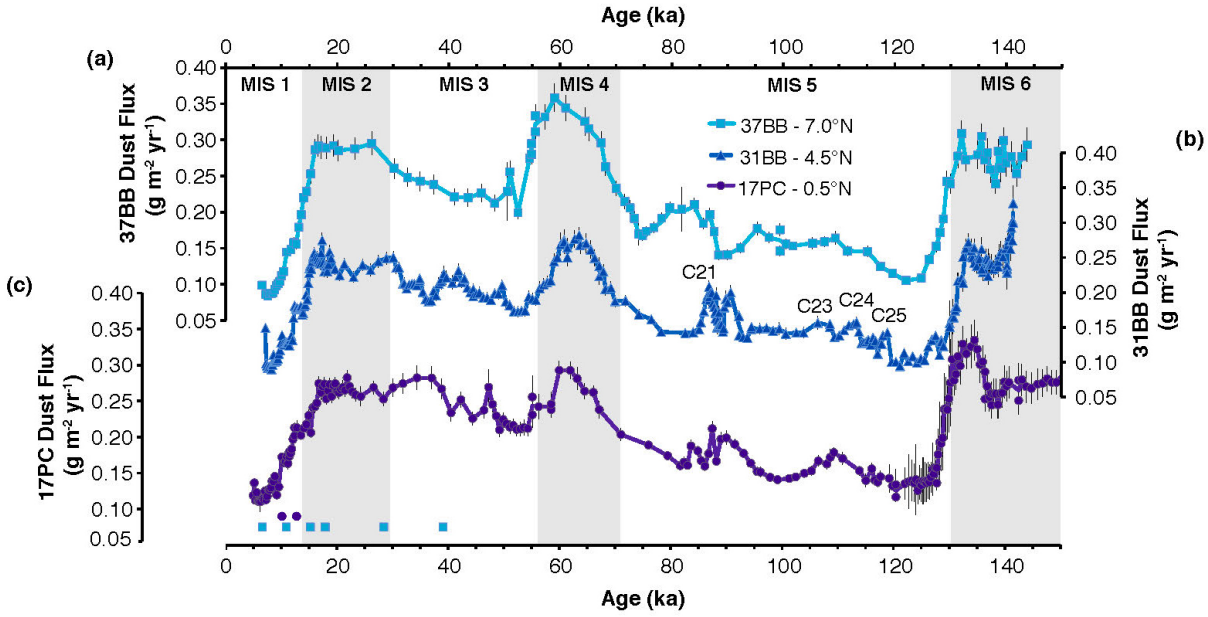

Figure 3.3: Dust fluxes and 2 sigma uncertainties for sites 37BB (teal squares), 31BB (blue triangles) and 17PC (purple circles). Lines (matching colors) represent the average of replicate points. Radiocarbon control points are indicated at the bottom of the figure in filled symbols for 37BB and 17PC using the same symbol and color scheme as above. Note that radiocarbon ages from 31BB were not used to determine the age model for that core. Marine Isotope Stage boundaries are at the top of the plot with grey shading indicating glacial stages. Note that all axes have identical scales.

et al., 2010). Changes in wind gust frequency and maximum speed may thus be driven by the growth of ice at the poles or by orbital variability in insolation gradients (and the seasonality of maximum contrast), inducing large scale changes in atmospheric circulation that translate on a regional scale to enhanced dust entrainment and transport. In this context it is interesting to observe that equatorial dust fluxes more closely track "sawtooth" changes in global ice volume than do high latitude dust flux records from the poles, which show similar baseline dust fluxes during MIS 5 and MIS 3 (Figure 3.4 b and d). Enhancement of westerly winds during glacial periods has previously been demonstrated in modeling experiments that attributed the strengthening primarily to the growth of ice sheets rather than a reduction in CO_2 (summary in Chiang and Friedman, 2012).

3.6.2 Dusty details and millennial events

Whereas previous studies have noted the strong first-order correlation between high latitude and tropical dust flux records on ~100 kyr timescales (Winckler et al., 2008), the increased temporal resolution of our new records allows for a more detailed evaluation and reveals shorter-lived features in the equatorial Pacific records that are correlative with events also observed at high-latitudes. Recent work, using the same sediment cores and techniques employed here, reconstructed a previously unknown millennial dust flux in association with the penultimate deglaciation and Heinrich Stadial 11 (Jacobel et al., 2016) and previous work in the far eastern equatorial Pacific identified an increase in dust in concert with Heinrich Stadial 1 (S. S. Kienast et al., 2013). Here we identify the signature of other stadial events that influenced equatorial Pacific dust fluxes over the last 150 kyr. In this section, we emphasize observations made using our highest resolution record, 31BB, focusing first on the identification of millennial increases in dust flux and then discussing the relationship between millennial stadial events and ITCZ movement in Section 3.6.5.

Stadial events have several different naming conventions depending on their origin and the paleoclimate archive in which they are identified. For example, intervals of depleted $\delta^{18}O$ corresponding to cold temperatures reconstructed from Greenland ice cores are called Greenland Stadials (GS) (S. O. Rasmussen et al., 2014). These GS events are frequently accompanied by increases in the flux of dust to ice core sites and sometimes include Heinrich

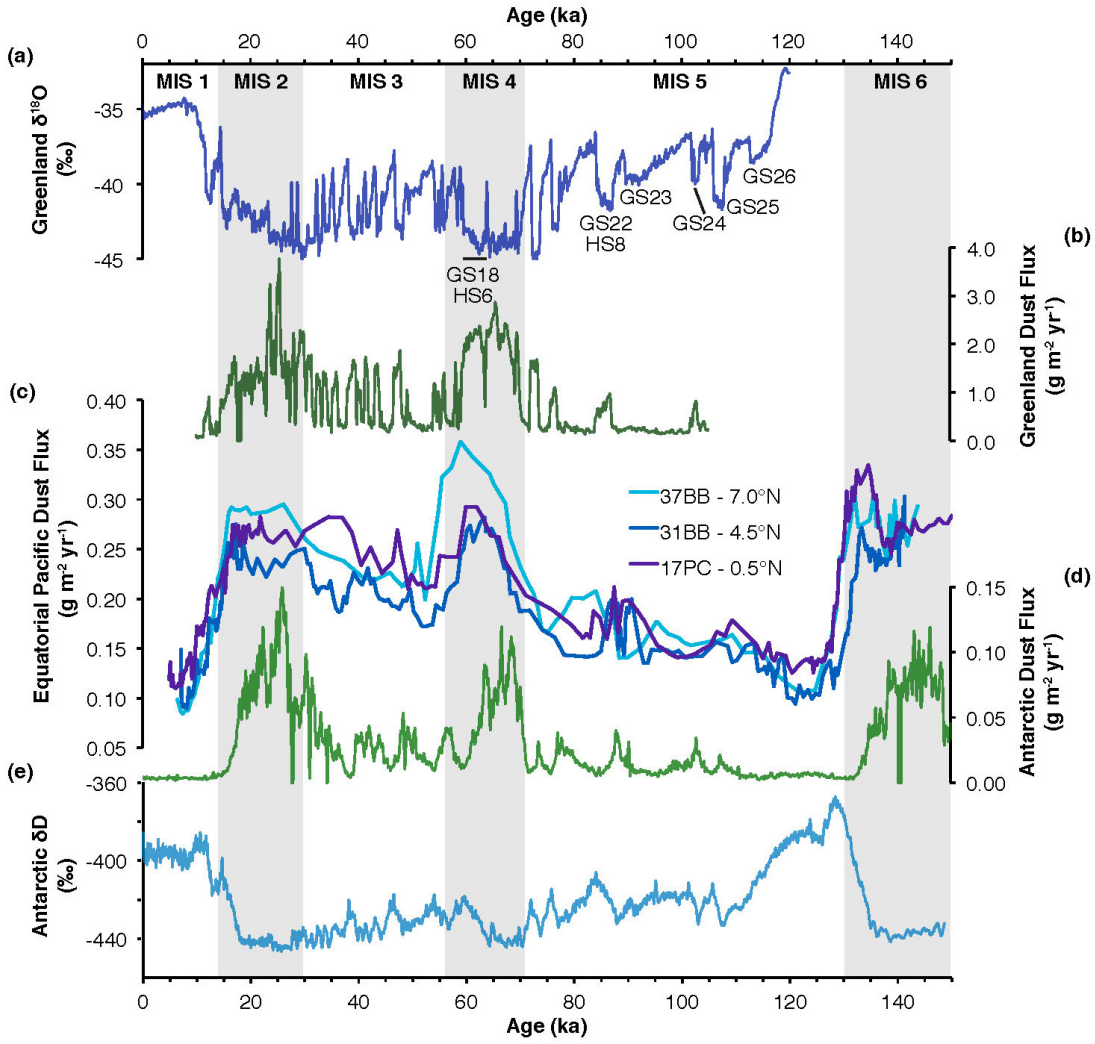

Figure 3.4: Oxygen isotope composition of the Greenland NGRIP ice core in blue (North Greenland Ice Core Project members, 2004) (a). Greenland dust flux record from NGRIP in dark green (Ruth et al., 2007) (b). Dust fluxes from the central equatorial Pacific (this study) with colors as in Figure 3.3 (c). Dust fluxes from the Antarctic EDC ice core in light green (Lambert et al., 2012) (e). Deuterium isotopic ratio of the Antarctic EDC ice core in light blue (Jouzel et al., 2007) (f). Records presented in panels a, b, d and e have been filtered for clarity (Section 3.8.6). Marine Isotope Stages labeled as in previous figure with selected Greenland and Heinrich stadial events labeled following (S. O. Rasmussen et al., 2014). All time series on the AICC2012 age model of (Veres et al., 2013).

Events, recognized as intervals of high ice rafted debris (IRD) in marine sediment cores, or C-Events characterized by intervals of cold SST in marine sediment records (J. McManus et al., 1994). The term Heinrich Stadial (HS) is often used to describe a cold interval that includes a Heinrich Event but is characterized by a proxy other than IRD. Previous work has established that nearly all intervals of widespread cooling in the NH correspond with intervals of warmth in Antarctica, a phenomenon known as the bipolar seesaw (summary in Landais et al., 2015). The exception to this rule is event GS26 (Capron et al., 2012), which occurs during the glacial inception when temperatures are decreasing globally. As a consequence of paired NH warming and SH cooling, most Greenland stadial events are associated with perturbations of the interhemispheric thermal gradient and are therefore thought to have resulted in shifts of the ITCZ (Landais et al., 2015).

Greenland Stadials 24, 25 and 26 During the last glacial inception beginning at ~123 ka, three stadial events occurred which are recognized in Greenland ice as GS 24, 25 and 26 (~105.4-104.5, 110.6-108.3 and 119.1-115.4 ka on the GICC05 age model (Seierstad et al., 2014)) (~103.2-102.2, 107.9-105.6 and 116.5-112.3 ka on the AICC2012 age model (Veres et al., 2013) Figure 3.5. These events have been identified both as intervals of cold temperatures in Greenland and cool SSTs in the North Atlantic (J. McManus et al., 1994; Oppo et al., 2006) and subtropical North Atlantic (Lehman et al., 2002; Pailler and Bard, 2002). Unfortunately, dust flux records from Greenland only extend to 108 ka and thus capture only GS 24 and its associated dust flux increase. Within the uncertainty of our age model and the two different age models for the ice core, the three GS events correspond with dust flux increases in core 31BB from ~109.3-103.7, 114.1-109.3 and 121.0-117.1 ka Figure 3.5. The three abrupt GS events appear somewhat more gradual in our records, likely due to the influence of bioturbation. Indeed, in a modeling exercise simulating bioturbation of an abrupt input function under constraints similar to those in 31BB, the synthetic dust flux record clearly mirrors our reconstructed dust fluxes (Section 3.8.6) (Figure 3.13). The identification of GS 24, 25 and 26 in the tropics is an intriguing result because it provides evidence that even millennial perturbations in ocean circulation had an impact on tropical climate via atmospheric dust abundance and associated climate variables. This conclusion

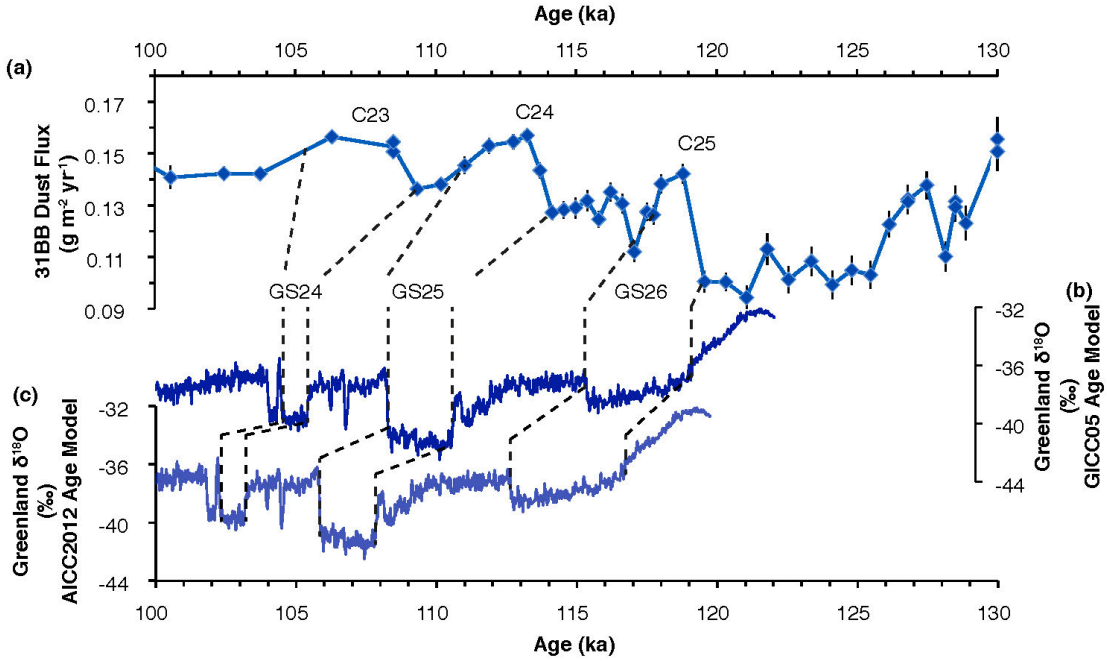

Figure 3.5: Dust fluxes from ML1208 31BB in blue (a). Oxygen isotope data from Greenland (NGRIP) (North Greenland Ice Core Project members, 2004) on the GICC05 age model (Seierstad et al., 2014) (navy blue) (b) and AICC2012 (Veres et al., 2013) (purple) (c) timescales.

complements data from the eastern equatorial Pacific suggesting ITCZ moisture shifts occurred in concert with North Atlantic stadials over the last 90 ka (Leduc et al., 2007). We suggest that abrupt climate perturbations previously identified in paleoclimatic records from Greenland and the North Atlantic, including those during MIS 5, may have had a more significant effect on Earth's radiative balance and other climate variables than previously appreciated.

Greenland Stadial 22 From 87.2 to 84.0 ka the Northern Hemisphere experienced a stadial event known in various climate archives as GS22, HS8 or C21 Figure 3.6 (Lehman et al., 2002; S. O. Rasmussen et al., 2014; T. L. Rasmussen et al., 2003). Greenland ice records indicate that this was a time of cold temperatures and increased dust fluxes (North Greenland Ice Core Project members, 2004; Ruth et al., 2007), North Atlantic

sediments show cooling and the deposition of ice-rafted debris (J. McManus et al., 1994), and speleothem data from Sanbao, China are interpreted as indicating a weakened East Asian summer monsoon over the same interval (H. Wang and Mehta, 2008). The abrupt dust flux increase in Greenland during GS22 contrasts with data from East Antarctica (Lambert et al., 2012) and the Southern Ocean (Anderson et al., 2014), which shows GS22 to be an interval of declining dust fluxes, preceded by an Antarctic dust increase (Figure 3.6). Because these two ice core records have had their age models synchronized using methane matching (Veres et al., 2013), we can be confident that the dissimilar dust fluxes observed in opposite hemispheres are indeed two separate events.

The interval between 95 and 85 ka is exceptionally well resolved in core 31BB with 34 data points yielding an average resolution of 350 years (not including replicates) (Figure 3.6d). Reconstructed dust fluxes exhibit a double peak with local maxima at ~90.7 and 87.0 ka. The more recent of these two dust peaks is almost certainly correlative with GS22/HS8/C21, but attribution for the earlier peak is more difficult. For the older dust flux maxima to be correlative with the SH dust increased observed in Antarctica, sedimentation rates would need to approach 12 cm ka^{-1}. Given the pelagic setting of this core and the observation that sedimentation rates at the site are more typically in the 3-5 cm ka^{-1} range, we find this scenario unlikely. Alternatively, the early dust flux peak in 31BB may be correlative with GS23/C22. However, in Greenland GS23/C22 is characterized by only a small oxygen isotope anomaly (North Greenland Ice Core Project members, 2004) and has no observable dust flux signature, in contrast with GS22/C21 which is identified by a larger isotope anomaly and significantly enhanced dust accumulation. In the subpolar North Atlantic C22 is similarly muted, being characterized by only a small decline in SST and negligible IRD deposition (J. McManus et al., 1994; Oppo et al., 2006). In contrast, SST underwent a brief, sharp decline in the subtropical Atlantic (Lehman et al., 2002) and Chinese speleothems record a decline in East Asian monsoon precipitation during GS23/C22 (H. Wang and Mehta, 2008).

The mismatch between records from the high and subtropical latitudes thus leaves open the possibility that GS23 was a significant event in NH climate that had particular implications for the tropics. If this is the case then it would appear that dust associated with

GS23 did not reach Greenland, possibly due to anomalous atmospheric circulation. For site 31BB to approximately match the relative timing and duration of GS23 and GS22, as recorded at Sanbao Cave, would require a change in sedimentation rate (~2 cm ka^{-1} increase) precisely at the trough between the two dust flux peaks. We find this to be a more likely scenario than the 12 cm ka^{-1} rate required for the peak to be of Southern Hemisphere provenance. Constraining the origin of the pre-GS22 dust peak is an important goal because 1) an abrupt shift of the hemispheric origin of dust deposited at site 31BB might indicate an abrupt, if small, shift of the ITCZ and 2) if the early dust flux peak we have identified is associated with GS23, it points to changes in the atmospheric pathway associated with the transport of Asian dust to Greenland, which may have been a unique feature of GS23. Site 37BB shows a different pattern from the two more southerly cores during GS22 and GS23 and immediately afterwards ((Figure 3.3). We suggest that the reason for this difference is an age model problem that makes the age of the increase in dust flux observed at 37BB between ~88 and 74 ka too young. The calculated one sigma age model uncertainty for the onset of this event is 88 ± 2.5 ka, which means that this event is probably coincident in the three cores. Site 37BB does demonstrate a much longer event duration relative to 31BB which cannot be attributed solely to age model differences and instead likely reflects the smoothing effects of bioturbation due to the low accumulation rate of 1.2 cm ka^{-1} in 37BB during this interval.

3.6.3 Marine Isotope Stage 4

Our tropical dust flux records show that MIS 4 was at least as dusty as MIS 2, and our lowest accumulation rate core (37BB at 7.0°N) suggests that MIS4 was dustier than MIS 2 in agreement with the record from Greenland (excepting the two brief dust peaks associated with Heinrich Stadials 1 and 2). This is an interesting observation given globally lower ice volume, higher CO2 concentrations and warmer temperatures during MIS 4 relative to MIS 2 (Petit et al., 1999). The apparent discord between observations of these climatic parameters thought to exert control on dustiness (summary in McGee et al., 2010) and the magnitude of dust flux observed at MIS 4 relative to MIS 2 leads to several hypotheses: 1) dust sources were more productive for other reasons (Rea, 1994), 2) uplift and transport of dust was more

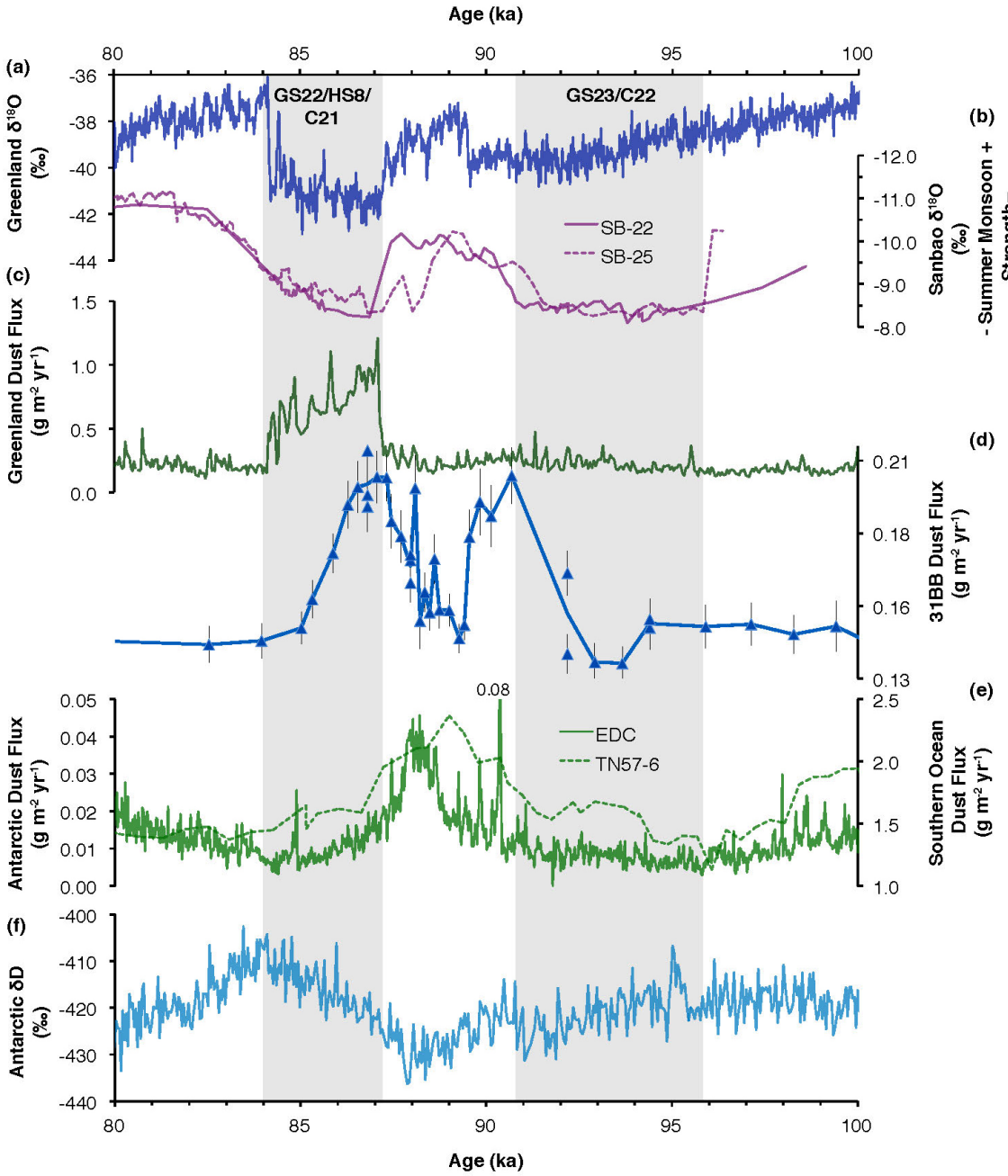

Figure 3.6: Oxygen isotope data from Greenland's NGRIP ice core (dark blue) (North Greenland Ice Core Project members, 2004) (a). Oxygen isotope data from Sanbao Cave, China (H. Wang and Mehta, 2008) (purple) (b). NGRIP dust flux data (dark green) (Ruth et al., 2007) (c). Dust flux data for core 31BB (blue) (d), EPICA Dome C dust flux data (light green line) (Lambert et al., 2012) and dust flux data from Southern Ocean core TN57-6 (light green dotted line) (Anderson et al., 2014) (e). Deuterium isotope ratio of the Antarctic EDC ice core (light blue) (Jouzel et al., 2007) (f).

efficient (McGee et al., 2010), 3) additional sources of dust contributed to tropical and NH fluxes, or 4) depositional processes were stronger. Without provenance data for the dust at the ML1208 sites it is difficult to assess hypothesis 3, but a record of dust flux from the North Pacific (Serno et al., 2017) also shows MIS 4 dust fluxes to be greater than during MIS 2, in support of the idea that increases in dust availability, entrainment and transport from Asian sources (hypotheses 1 and 2) may have played a significant role at latitudes north of, or within, the seasonally shifting ITCZ. This interpretation is strengthened by data indicating that during MIS 4 the median diameter of wind-blown quartz grains in China's Luochuan Loess increased (Porter and Zhisheng, 1995), and the flux of aeolian quartz to Japan's Lake Biwa was large (Figure 3.7c), coincident with a decrease in the flux of fluvial quartz to the same lake (Xiao et al., 1999). The authors of these records interpret the results to indicate that MIS 4 winter monsoon winds were stronger (Porter and Zhisheng, 1995; Xiao et al., 1999), and that the summer monsoon was weaker, leading to drier conditions (Xiao et al., 1999). Additional support for strengthened NH westerly winds comes from the Iberian margin where a sediment core taken from within the modern wind belt shows sea surface temperature cooling during MIS 4 to temperatures 3-4 degrees cooler than at the LGM (Pailler and Bard, 2002) (Figure 3.7b). Pailler and co-authors attribute this cooling to the combined influence of cold North Atlantic waters advected to the site during HS6 (63.55-59.23 ka) (North Greenland Ice Core Project members, 2004) and strengthened wind-driven upwelling.

Data also exist in support of strengthened MIS 4 southeast trade winds in the SH. For example grain size records from South Africa show enhanced coarse fraction delivery during MIS 4 above average MIS 2 values (Stuut et al., 2002). The SH may also have had active dust source areas that could have contributed dust to the central equatorial Pacific during its MIS 4 glacial maxima, but data are currently lacking to evaluate this hypothesis. In sum, more arid summers in Asia and globally strengthened winds during MIS 4 may have led to increased deflation and transport of dust, resulting in the larger dust fluxes observed in Greenland and at our equatorial sites.

The fourth mechanism for increased MIS 4 dust fluxes at the ML1208 sites is stronger tropical depositional processes. In light of the large increase in North Pacific dust fluxes

coincident with those in the tropics (Serno et al., 2017), we suggest if depositional processes were enhanced they were not the primary factor contributing to higher dust fluxes. Although our records cannot be interpreted simply as indicative of the amount of precipitation or wet-scavenging occurring over our three sites, we do suspect hydrological changes may have played a role in the relative differences in dust deposition (as discussed in Section 3.6.5).

The observation of comparable (sites 31BB and 17PC) or enhanced (Greenland, site 37BB) dust deposition during MIS 4 relative to MIS 2 is unexpected given traditional models of the climatic parameters driving global dustiness. Of the four hypotheses evaluated to explain this apparent inconsistency, evidence exists in support of enhanced dust supply, suspension and transport (1 and 2). Additional data are needed to constrain the potential role of unidentified dust source areas (3) and changes in the strength of tropical hydrology (4).

3.6.4 Orbital cyclicity

Previous work has sought to identify connections between the position and/or strength of the ITCZ (Liu et al., 2015) and dust abundance (Larrasoana et al., 2003) with variations in Earth's orbit related to parameters of eccentricity, obliquity and axial precession. In this study, despite more than sufficient sampling to resolve even the highest frequency orbital components, spectral analysis of 37BB and 31BB reveals little power above background at frequencies associated with orbital parameters (Figure 3.8). The time series from core 17PC does visually demonstrate some power in the 41 kyr and 23 kyr bands, and these periodicities are statistically significant in the power spectral density, but power is not concentrated there. We suspect the absence of strong coherence between orbital periodicities in the cores is because these dust flux records reflect the combined influence of dust generation, entrainment, transport and possibly periodic ITCZ deposition, and thus either do not respond in a simple way to changes driven by orbital variability, or there are other more dominant controls on their variability.

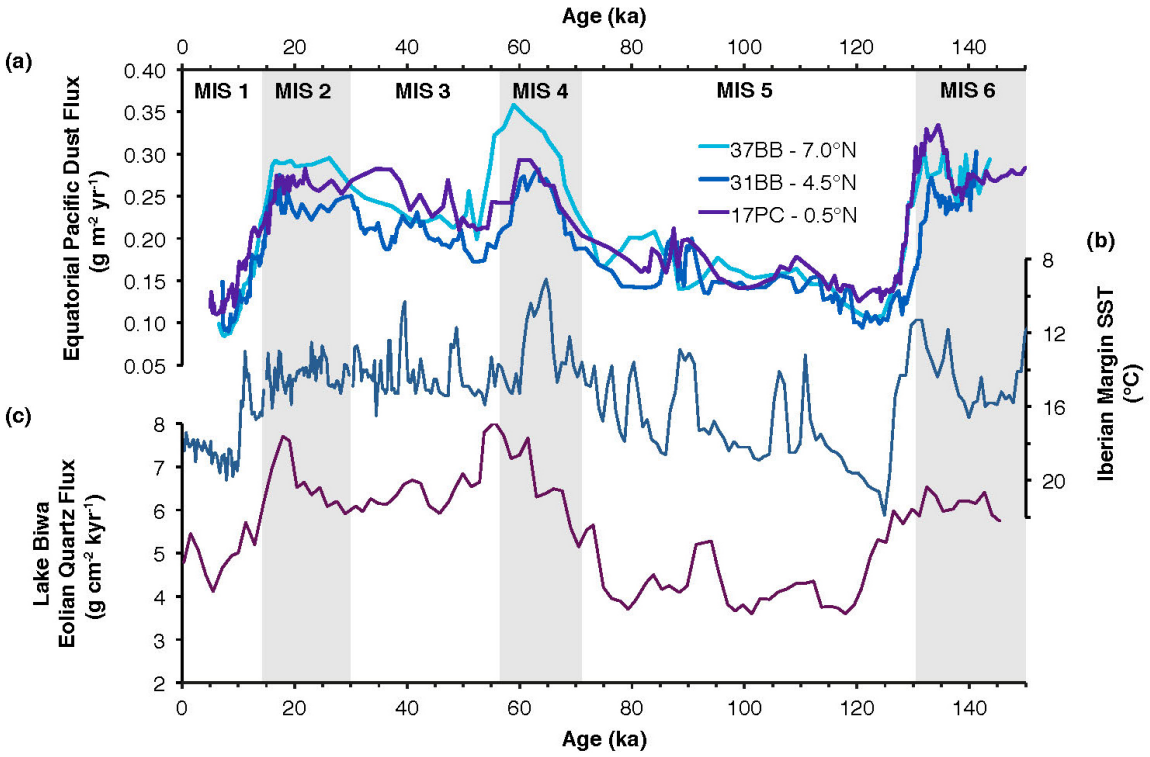

Figure 3.7: Dust fluxes for the three ML1208 cores (colors as in previous figures) (a). Iberian margin alkenone-based sea surface temperature record (Pailler and Bard, 2002) (navy) (b). Lake Biwa eolian quartz flux (purple) (Xiao et al., 1999) (c). Marine Isotope Stages labeled as in previous figures.

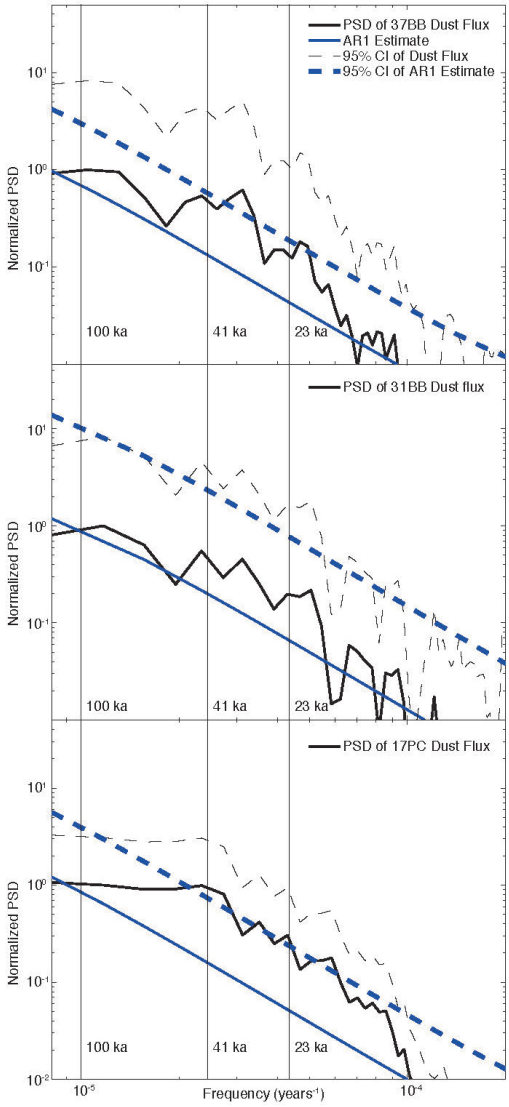

Figure 3.8: Estimated power spectral density (PSD) for dust fluxes at 37BB (a), 31BB (b) and 17PC (c) using the Thompson Multitaper Method, normalized to the power of the 100 kyr cycle in each PSD plot. The significance of spectral peaks (solid black lines, dotted black lines 95% confidence intervals) is tested against the null hypothesis of a first order autoregressive process (solid blue line, dotted blue line 95% confidence interval). Solid vertical lines represent frequencies associated with the orbital periodicities of 100, 41 and 23 ka. Peaks of the solid black line above the dotted blue line indicate frequencies with significant concentrations of power at the 95% confidence level.

3.6.5 ITCZ movement

Glacial/Interglacial position Recent modeling work has suggested that long term shifts of the ITCZ are difficult to sustain without significant and persistent perturbations of the cross equatorial heat flux (e.g., McGee et al., 2014), which are not supported by paleoceanographic reconstructions on glacial-interglacial timescales (Böhm et al., 2014). On these timescales increases and decreases in the magnitude of dust delivered to our three study sites are largely coherent, making it difficult to distinguish the hemispheric origin of dust delivered at each site. However, during MIS 2, from approximately 29 to 14 ka, and during MIS 4 from 71 to 57 ka, site 37BB displays the highest dust fluxes of any of the three sites (Figure 3.4) despite having the lowest overall sedimentation rates. This observation indicates that the ITCZ likely delivered relatively more precipitation and dust to the northernmost site (7.0°N), pointing to a Pacific ITCZ at a latitude similar to its present day position (Figure 3.1) consistent with work from the Eastern Equatorial Pacific (Xie and Marcantonio, 2012), dust provenance data from the same ML1208 sites studied here (Reimi and Marcantonio, 2016), and modeling results (McGee et al., 2014). Conclusions about the average position of the ITCZ during MIS 3 and MIS 5 are much harder to draw because of the frequency of millennial events in both hemispheres, which are not always well resolved by our records.

Millennial shifts Previous intercomparison of a time-subset of the three dust flux records presented here identified an abrupt shift of the ITCZ during TII in concert with the North Atlantic HS11 (Jacobel et al., 2016). Here, we examine whether significant features of our new 150 kyr records might also be indicative of ITCZ shifts. Key to our reconstruction is the observation that while global dust fluxes respond in a coherent way to glacial-interglacial variability, millennial dust increases in the northern and southern hemispheres are frequently out of phase, with maximum Antarctic dust fluxes preceding or nearly coincident with the onset of enhanced dust deposition in Greenland (Figure 3.9. An example of the temporal offset between dust fluxes in Antarctica and Greenland is the relationship observed from 95 to 80 ka, when dust fluxes in Antarctica peaked and began to decline before Greenland dust fluxes increased rapidly in association with GS22 (Figure 3.6).

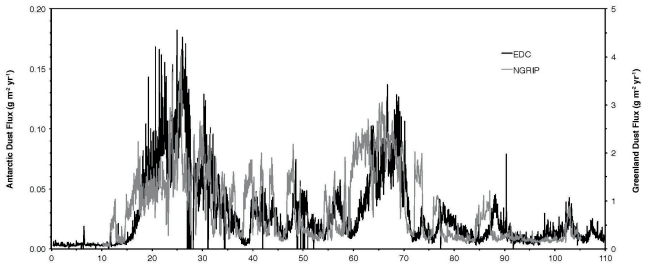

Figure 3.9: Dust fluxes from the Antarctic EDC ice core (Lambert et al., 2012) (black) and Greenland NGRIP ice core (Ruth et al., 2007) (grey) displayed on the AICC2012 timescale (Veres et al., 2013).

Greenland stadials Over the last 150 kyr our highest resolution dust flux record, 31BB, records the signatures of abrupt dust flux increases associated with HS11, GS26, GS25, GS24, GS22, most likely GS23 (Jacobel et al., 2016, and our Section 3.6.2) and possibly GS18 (discussed below). These Greenland stadials are among the longest duration cooling events and show the largest magnitude of corresponding Antarctic warming and adjustment of the interhemispheric thermal gradient, epitomizing the biopolar seesaw (Figure 3.10). The location of site 31BB is on the southern edge of the ITCZ and precipitation at 4.5°N is largest during boreal spring (Figure 3.1) when Asian dust storms are common due to cyclogenesis (Roe, 2009; Serno et al., 2015). Thus, while the observation of Northern Hemisphere dust events in 31BB is not necessarily indicative of a large change in ITCZ position, the presence of NH dust events in 31BB does require an ITCZ shift south of its modern position.

During GS24, GS25 and GS26 site 17PC has sedimentation rates very similar to 31BB (2.4 vs 2.7 cm ka^{-1}), however the signature of these events is not easily identifiable at 17PC (Figure 3.3c). At least two possible mechanisms could explain this difference. First, a sedimentary modeling experiment suggests that a mixed layer depth of 11 cm would largely obscure the dust flux signatures of GS24, 25 and 26 at 17PC. This mixed layer depth is twice that simulated for site 31BB and at the upper limit of "diffusive" mixing attributed to benthic activities (Smith et al., 1997). However, we do not have in situ data on bioturbation at site 17PC and thus we cannot evaluate this hypothesis. A second possibility is that the contribution of NH dust reaching 0.5°N during these stadials was negligible, indicating

that the ITCZ shifted southwards but not far enough to contribute NH dust to 17PC. An analogous situation may have occurred during GS22 and 23 when multiple peaks of dust are observed at 17PC (Figure 3.3). During this interval, accumulation rates at 17PC average 2.7 cm ka^{-1} while at 31BB they are closer to 4.2 cm ka^{-1}. The early part of the increase between 95 and 86 ka probably corresponds with a SH dust flux increase from 95-88 ka (Figure 3.6e), however we cannot eliminate the possibility that the peak from 86-83 ka is related to GS22/HS8. If the dust flux increase at 17PC is indeed related to GS22/HS8, a substantial shift of the ITCZ southwards would have to have occurred, allowing NH-sourced dust to reach the equator.

Marine Isotope Stage 4 In Section 3.6.3 we discussed a substantial body of evidence indicating dustier and windier conditions during MIS 4. However, the hypotheses explored in that section do not explain the higher dust flux at core 37BB relative to fluxes at sites 31BB and 17PC. The observation of the highest fluxes at the northernmost site is remarkable considering that sedimentation rates at site 37BB (1.2 cm ka^{-1}) are almost three times lower than at 31BB (3.3 cm ka^{-1}) and less than half those at 17PC (2.6 cm ka^{-1}) between 80 and 60 ka (Figure 3.11). These large differences in accumulation, in combination with bioturbation, would be expected to lead to smoothing of the signal's amplitude at 37BB relative to the records at the other two sites. Instead, dust fluxes at 37BB are at maximum ~20% higher beginning at ~64.4 ka (allowing for 2 sigma age and analytical uncertainty in our data), a difference that cannot be attributed to more intense bioturbation at the southern sites. We propose that the reason for the substantial difference in dust flux between the northernmost and two more southern sites is that the mean ITCZ was positioned northwards at that time relative to GS26, 25, 24, 23 and 22. An increase in the total amount of dust in the tropical atmosphere alone would not yield the observed pattern because atmospheric dust removal and deposition at all sites would be proportionally larger. During GS18/HS6 cold stadial conditions characterized Greenland ((Figure 3.4a) while Antarctica experienced warming associated with Antarctic Isotopic Maximum (AIM) 18 (Figure 3.6e). This asymmetry would have caused a shift in the thermal gradient and may have pulled the ITCZ southwards from a northerly position associated with MIS 5a warmth in the North

Atlantic. In sum it appears that the MIS 4 and/or GS18/HS6 position of the ITCZ may represent a southward shift, albeit to a latitude northwards of its position during MIS 5 millennial events. It remains unclear whether that latitude was north, south or similar to the modern day ITCZ.

Other millennial shifts Atlantic ITCZ hydrological shifts in response to North Atlantic HS have been previously observed for HS4, 5 and 6 as recorded by Brazilian speleothems (X. Wang et al., 2004) and a salinity reconstruction from the eastern equatorial Pacific has been used to suggest decreases in moisture transport in association with HS during MIS 2-4 (Leduc et al., 2007). Given that the duration of these events and magnitude of associated Antarctic warming is in line with other events we do identify (Figure 3.10), we strongly suspect that dust flux increases associated with HS4 and 5 are present in our records. Unfortunately, identification of these events is challenging because the frequency of dust flux increases in the SH and NH (the latter due to GS events) is increased during MIS 3 relative to MIS 4 and 5 (Figure 3.4). Given the limitations of our age models, the influence of bioturbation and the sampling resolution of our new records, we are thus unable to unequivocally identify these events or to associate them with shifts of the Pacific ITCZ. Two of the best-studied Heinrich Stadials (HS1 and HS0/YD) also occurred during the interval presented in this paper. Because these events occurred during the last deglacial termination, in the same way that HS11 occurred during the penultimate termination, they are the focus of a separate, detailed comparison study of deglaciations (Jacobel, in prep). Here, we note that in contrast with the penultimate deglaciation, core 17PC (the southernmost site) shows no evidence of having received NH dust associated with H1 or the YD during TI (Figure 3.4b and c). However, there is some evidence in 31BB of structure similar to that observed in the Greenland ice core record during both deglacial stadial events. This leads us to conclude that the position of the ITCZ during TI stadial events may have been very similar to its position during GS 24, 25 and 26. This inference stands in contrast with data from TII indicating a more substantial southwards shift of the ITCZ during that deglaciation. Indeed our data suggest that the southward shift of the ITCZ that occurred during TII (Jacobel et al., 2016) has been unparalleled over at least the last

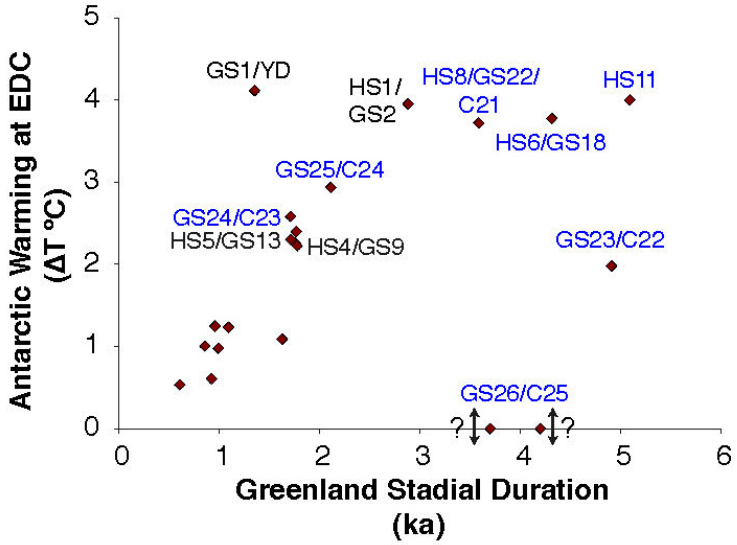

Figure 3.10: Cross plot of Greenland stadial duration (ka) and associated Antarctic warming at EPICA Dome C. Events with blue labels have been identified in the ML1208 cores presented in this study. Data and figure adapted from (Marino et al., 2015). Additional data points added as described in Section 3.8.7, employing data from (Masson-Delmotte et al., 2010; Seierstad et al., 2014; Veres et al., 2013; H. Wang and Mehta, 2008).

150 kyr.

3.7 Conclusions

Dust plays a crucial role in the climate system as both a force that can drive climate and as feedback to environmental change. Here we have reconstructed millennial-scale resolution records of dust flux from the tropics, the first to cover MIS5-3. Our latitudinal transect of cores sheds light on both the atmospheric load of dust in the tropics and the relative position of the ITCZ over the last 150 kyr. These new records highlight the complex role dust generation, deflation, transport and deposition processes play in influencing the tropical record of dust flux. On glacial-interglacial timescales these processes result in a scenario where dusty glacial periods abruptly transition to interglacial periods with ~3 times lower

dust fluxes, returning to dustier conditions in step with cooling global temperatures and ice volume growth. Our data suggest that any shifts of the ITCZ in response to glacial-interglacial changes in the interhemispheric thermal gradient were likely to have been small in the central equatorial Pacific, at least over the last interglacial and glacial cycle. On millennial timescales our new records reveal marked changes in dust abundance, and small shifts in ITCZ position relative to modern in response to changes in hemispheric thermal gradients driven by a handful of the longest North Atlantic stadial events. These new data provide evidence that high-latitude cooling and circulation changes have repeatedly influenced the tropical radiation balance via changing dust fluxes and have occasionally caused significant perturbations in tropical hydrology on relatively short timescales. Our inferences strongly support the utility of highly (temporally and spatially) resolved records of paleoclimate, and should encourage the development of high-resolution records from the tropics to constrain other components of the climate system and responses to high-latitude climate forcing.

3.7.1 Data archiving

Line Islands dust flux data are archived at the National Oceanic and Atmospheric Administration National Centers for Environmental Information (NCEI) database.

3.8 Supplementary Notes

3.8.1 Radiocarbon dates

Age models for all three cores were initially constrained using a combination of radiocarbon dates (Table 3.1) and planktonic δ^{18}O data, as described in the main text. All new radiocarbon ages were measured on G. ruber from the 250-500 m size fraction at the National Ocean Sciences Accelerator Mass Spectrometry (NOSAMS) facility of Woods Hole Oceanographic Institution. Radiocarbon ages were converted to calendar date using the marine calibration curve (MARINE13) (Lambert et al., 2012; Reimer et al., 2013). Radiocarbon data for core 31BB indicate that between 0 and 12 cm core depth there is an age reversal and thus radiocarbon dates and planktonic δ^{18}O above 12 cm depth were not used to

provide age constraints. Consequently, the age-depth model for this core begins at 13 cm and no data from above this interval are presented in the paper due to the likelihood that younger sediments are disturbed. After the initial age models were generated, the observation was made that the age of the last glacial termination in core 31BB did not appear consistent with timing of deglaciation in either of the other two planktonic δ^{18}O models or the LR04 stack. Recalculating the age model for 31BB based solely on planktonic δ^{18}O data (removing radiocarbon-based age constraints) generated an age model with a slightly improved correlation between planktonic δ^{18}O and the LR04 stack (R2 of 0.89 for the δ^{18}O-only model vs 0.85 for 14C and δ^{18}O combined). The new δ^{18}O-only model is different from ages at 36, 40, 48, 56, 72 and 100 cm depth by 0, 0, 1.04, 1.55, 0 and 0.75 kyr respectively (using 2 sigma uncertainties for radiocarbon ages and the δ^{18}O-only model).

Given that both δ^{18}O and 14C were measured on the same species of foraminifera the inconsistency in 31BB at 48, 56 and 100 cm is a perplexing observation. How can it be that radiocarbon dates provide less reliable age constraints than δ^{18}O measured on the same proxy archive (G. ruber)? We propose that the process that led to the apparent biases in the radiocarbon data did also affect the δ^{18}O. However, because the rate of change in the oxygen isotope data is small at these specific depths, foraminifera from a few centimeters above or below can be moved without creating obvious anomalies in the δ^{18}O data. Close inspection of 31BB at 48 cm and 56 cm does actually reveal some unusual variability in the δ^{18}O, but the magnitude is small enough that it does not bias the age model. This is in contrast with 14C, which has a relatively constant rate of change down core and thus small-scale bioturbation, dissolution or focusing can have a larger impact on observed values.

3.8.2 Sedimentation rates and bioturbation

Open ocean sedimentation rates are affected by variations in accumulation rates, post-depositional redistribution and preservation processes that are especially important to consider when differences between cores are used to interpret past climate. In the suite of sediment cores examined here, apparent accumulation rates are almost always highest at site 31BB and lowest at site 37BB. Rates exhibit variability at all three sites (Figure 3.11)

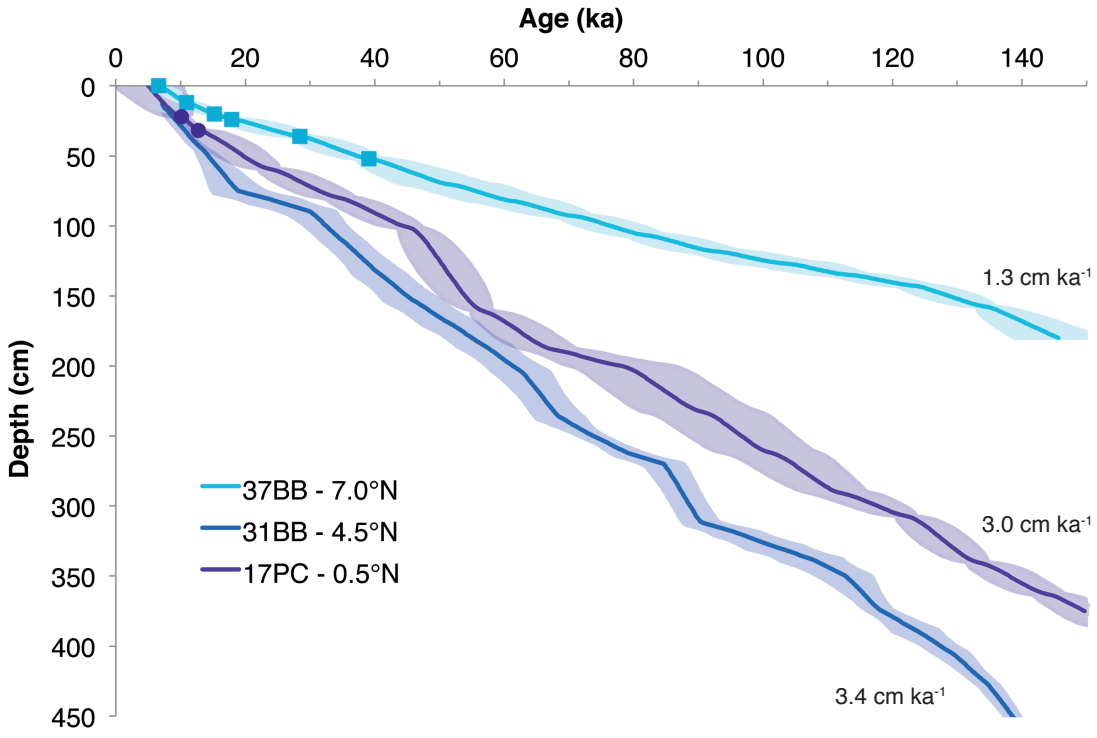

Figure 3.11: Data for cores 37BB (teal line), 31BB (blue line) and 17PC (purple line) with shading indicating two sigma uncertainties (95% confidence intervals) for each age model. Average accumulation rates for the 150 kyr interval discussed here are depicted.

but average 1.3 cm ka^{-1} at 37BB, 3.0 cm ka^{-1} at 17PC, and 3.4 cm ka^{-1} at 31BB. One of the implications of spatial variation in sedimentation rates is that the bioturbational activities of benthic organisms are likely to have affected the three records to varying degrees. The cumulative effect of bioturbation is to mix the sediment, causing material at a given depth to reflect a mixture of sediment at, below, and to a lesser extent above that interval. If the mixing depth is held constant, lower sediment accumulation rates will lead to greater smoothing of the proxy record. Because bioturbation is typically greater at higher organic contents (Smith et al., 1997), we expect mixing to be greatest at site 17PC where the organic carbon flux is greater due to the influence of equatorial upwelling. In this study the site with the lowest accumulation rate (37BB) and the site with the largest supply of organic matter (17PC) are most likely to be affected by bioturbation.

3.8.3 Concentration of ^{232}Th in dust

Previous work has suggested that, the average concentration of ^{232}Th in dust sources which may contribute to our study area is ~10.7 ppm (McGee et al., 2007; Xie and Marcantonio, 2012). More recently, a survey of records found that a value of 14 ppm may more accurately describe the ^{232}Th concentration of fine grained lithogenic dust (McGee et al., 2016), like that present at our core sites. This would suggest that studies using a value of 10.7 ppm may have consistently overestimated the amount of dust present by as much as 30%. While this difference may be significant for records focused on comparing the absolute amount of dust between study sites using different concentration conversions, here our interpretations are based on the relative differences within and between cores. To facilitate comparisons with previously published records from these sites which used 10.7 ppm as the ^{232}Th concentration, we continue to use that value here and encourage readers comparing our work to other studies to carefully note the use of this parameter when making quantitative comparisons.

3.8.4 Usage of ^{230}Th$_{xs,0}$

^{230}Th is produced by radioactive decay of well-mixed, soluble ^{234}U throughout the water column, and ^{230}Th burial in the sediments is approximately equal to its rate of production because it is highly particle reactive and thus has a short residence time relative to its half-life (Bacon, 1984; Bacon and Anderson, 1982; Francois et al., 2004). Because of these characteristics, the concentration of ^{230}Th in sediments not supported by sedimentary ^{234}U is primarily a function of water depth (with greater depths providing for more ^{230}Th) and the bulk flux of particles to the seafloor (mass accumulation rate-MAR) (Henderson and Anderson, 2003). In sediments where the integrated burial of ^{230}Th$_{xs,0}$ is greater (less) than expected due to water column production, lateral sediment accumulation or focusing (removal, winnowing or dilution) is typically implicated (S. S. Kienast et al., 2007). To account for these differences and isolate changes in the variable of interest (in this case ^{232}Th) ^{230}Th$_{xs,0}$-normalization is commonly employed (Anderson et al., 2006; McGee et al., 2007, 2016; Serno et al., 2015; Winckler et al., 2008).

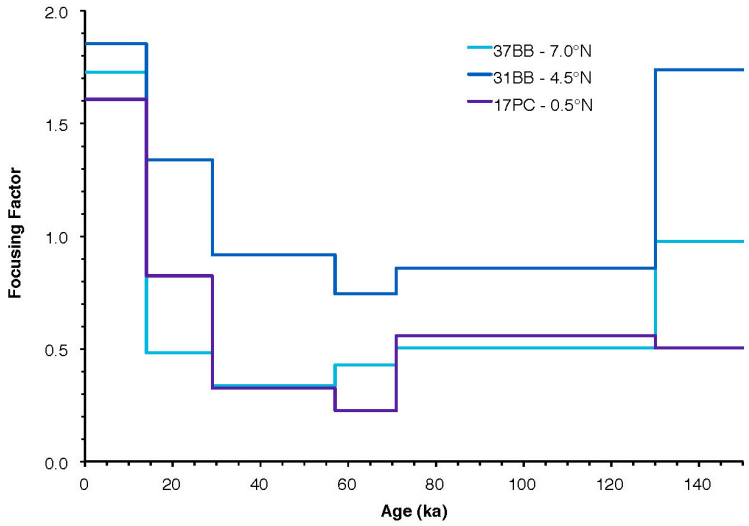

Figure 3.12: Focusing factor data for cores 37BB (teal line), 31BB (blue line) and 17PC (purple line). Values less than one indicate winnowing and values greater than one indicate lateral addition of sediment (focusing). Focusing factors are calculated between each MIS boundary (Lisiecki and Raymo, 2005).

3.8.5 Focusing factors

Focusing factors are presented in Figure 3.12 with values greater (less) than one indicating that sediment has been added (removed) from the site due to focusing (winnowing). Values for all three sites are below 2, with a small increase in lateral sediment redistribution to all three sites during the Holocene. A significant decrease in focusing factors from Marine Isotope Stage (MIS) 6 to MIS 5 occurs in the two northernmost cores, 37BB and 31BB, but site 17PC remains relatively constant over this interval. During MIS4 (71-57 ka) all three cores demonstrate slight decreases in focusing factors and more generally indicate winnowing from 130 ka to at least 29 ka. Despite winnowing in all cores, it is notable that during all intervals studied, site 31BB has consistently higher focusing factors. This explains its generally higher sedimentation rate relative to the other two cores, despite its off-equator location.

3.8.6 Filtering of panels in Figure 3.4

The ice core records presented in panels a, b, d and e of Figure 3.4 have been filtered for clarity. This was accomplished using a Savitzky-Golay smoothing filter with frame lengths of 25, 11, 19 and 11 points for panels a, b, d and e respectively. These frame lengths were chosen such that a filter of ~0.5 ka would be applied at 60 ka in each record. The resolution of our most highly resolved sediment core, 31BB, is on average 0.5 ka. Because of the variable down core data resolution inherent with ice cores, the filter lengths imposed do not have a fixed time interval. Changing the length of filters used in this figure does not appreciably alter the picture presented and has no significance for the interpretations and comparisons made here.

3.8.7 Dust flux input function and bioturbation

Figure 3.13 depicts the results of an experiment in which an abrupt increase in dust flux input is simulated (black line, panel 2), similar to the dust flux input that is likely to have occurred over MIS5d. We then simulate the effects of bioturbation on that input function by assuming a constant sedimentation rate of 2.75 cm ka^{-1} (the accumulation rate of core 31BB over this interval) and a mixed layer depth of 5 cm (Boudreau, 1994). The resulting record (red line, panel 2) illustrates what we would expect the input function to look like under conditions similar to those experienced by core 31BB over the same time interval. The similarity between the synthetic bioturbated record and the dust fluxes reconstructed in 31BB supports our interpretation of these events as related to abrupt increases of dust flux associated with GS 24, 25 and 26.

3.8.8 Origin of Figure 3.10

Manuscript Figure 3.10 displays a summary of Greenland stadials relevant to our new records. This figure follows from the work of (Marino et al., 2015) whose original display item did not include the YD, HS1/GS2, GS23/C22, or GS26/C25. These events were added using the age constraints described in the figure caption and in-text (which for 26 includes both the GICC05 and AICC2012 age models). The duration of GS23 was determined using the U/Th dated speleothem record from Sanbao Cave (H. Wang and Mehta, 2008). The

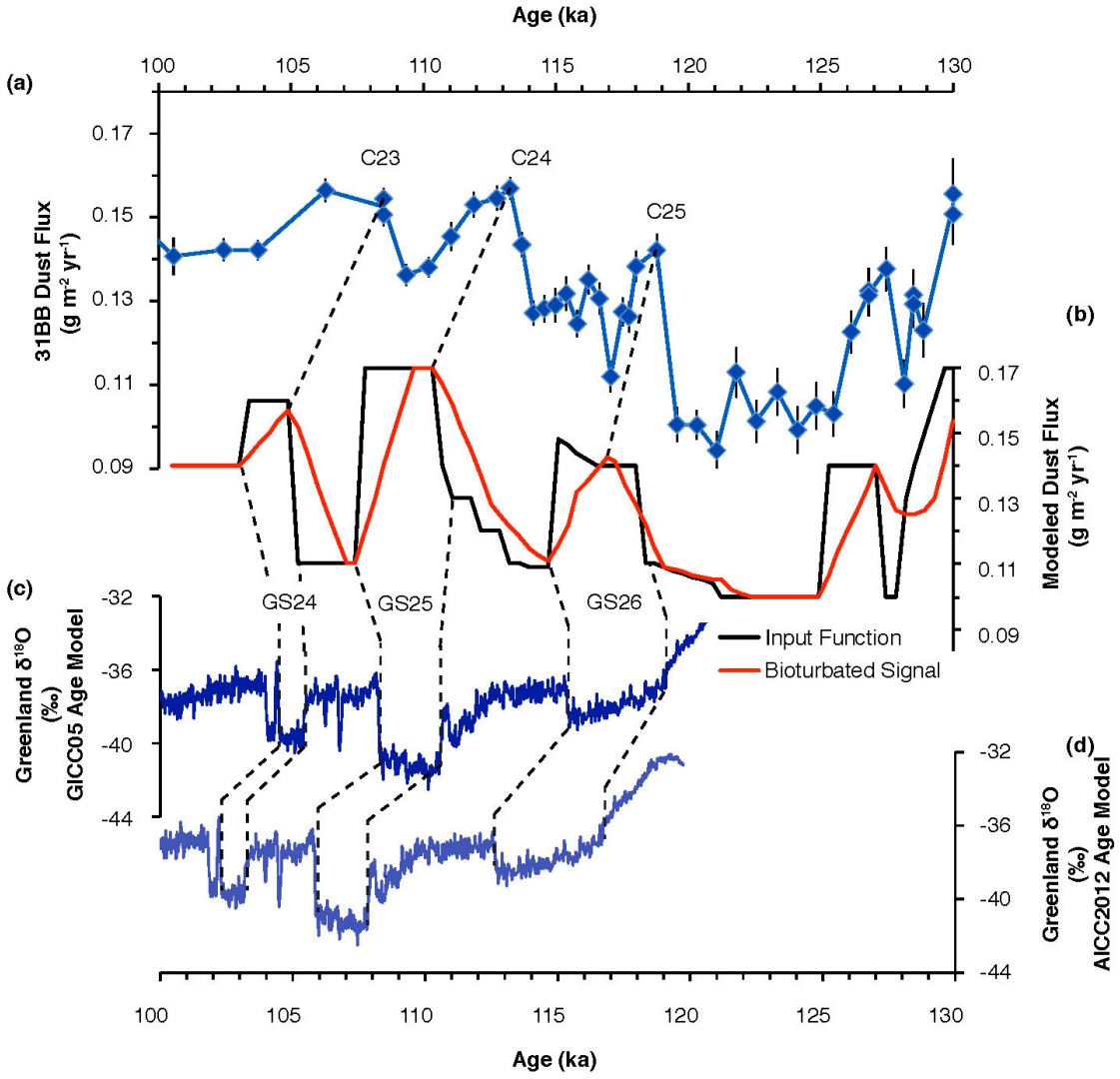

Figure 3.13: Dust fluxes from ML1208 31BB in blue (a). Simulation of the result of bioturbation (red) on a dust flux impulse record (black) (b). Oxygen isotope data from Greenland (NGRIP) on the GICC05 (Seierstad et al., 2014) (navy blue) (c) and AICC2012 (Veres et al., 2013) (light blue) (d) timescales.

Cruise	Core	Depth in Core (cm)	14C Age (years)	14C Age Error (years)	Mean Calendar Age BP (years)	2 σ Minimum Calendar Age BP (years)	2 σ Maximum Calendar Age BP (years)
ML1208	37BB	0	6,180	35	6,619	6,508	6,719
*ML1208	37BB	12	9,940	30	10,911	10,750	11,057
*ML1208	37BB	20	13,200	45	15,242	15,090	15,435
*ML1208	37BB	24	15,100	55	17,887	17,690	18,052
*ML1208	37BB	36	24,800	200	28,423	27,952	28,822
*ML1208	37BB	52	35,000	700	39,106	37,196	40,732
ML1208	31BB	0	11,200	60	12,689	12,580	12,819
ML1208	31BB	4	6,700	45	7,213	7,138	7,335
ML1208	31BB	12	6,280	50	6,735	6,616	6,874
*ML1208	31BB	36	10,450	30	11,573	11,339	11,798
ML1208	31BB	40	11,550	45	13,030	12,869	13,169
*ML1208	31BB	48	14,100	35	16,520	16,317	16,755
*ML1208	31BB	56	16,100	45	18,931	18,806	19,064
ML1208	31BB	72	17,450	75	20,560	20,316	20,794
*ML1208	31BB	100	24,800	75	28,457	28,198	28,695
*ML1208	17PC	22	9,290	25	10,147	10,062	10,208
*ML1208	17PC	32	11,300	35	12,762	12,656	12,883

Table 3.1: Radiocarbon and calibrated calendar ages (years BP) for the ML1208 cores used in this study (Lynch-Stieglitz et al., 2015). Asterisks indicate previously unpublished age control points. Note that none of the radiocarbon dates for core 31BB were explicitly used in generating the age model for that core.

magnitude of Antarctic warming associated with these NH stadial events was determined using the warming residual calculated by (Masson-Delmotte et al., 2010) which excludes warming attributable to changes in greenhouse gas concentrations and insolation. The total magnitude of Antarctic warming is reported for all events, not just the amount of warming occurring coincident with NH cooling (because of phase differences). For GS 26 (whose vertical position on the y-axis is marked with a question mark), the magnitude of Antarctic warming could not be determined due to the SH glacial inception.

3.9 Acknowledgements

We thank the core repository at LDEO for providing samples and Marty Fleisher for assistance in the lab. Special thanks to Jeremy Hoffman for generously sharing his MonteXCM code to improve the age models presented in this paper and to Jean Lynch-Stieglitz for

assistance with and discussion of 14C dates. This research was funded in part by awards from the Geological Society of America (A.W.J.) and US National Science Foundation AGS-1502889 (J.F.M. and G.W.), and benefited from previous support from NSF OCE-1003374, OCE-1159053 and OCE-1158886, and the Comer Science and Education Foundation.

Part II

Equatorial Pacific Deep-Water Chemistry

Chapter 4

Repeated storage of respired carbon in the equatorial Pacific Ocean over the last three glacial cycles

Note: A modified version of this chapter has been submitted to *Nature Communications* [1]

Abstract

As the largest reservoir of carbon exchanging with the atmosphere on glacial-interglacial timescales, the deep ocean has been implicated as the likely location of carbon sequestration during Pleistocene glaciations. Despite strong theoretical underpinning for this expectation, radiocarbon data on watermass ventilation ages are conflicting, and proxy interpretations disagree about the depth, origin and even existence of the respired carbon pool. Because any change in the storage of respiratory carbon is accompanied by corresponding changes in dissolved oxygen concentrations, proxy data reflecting oxygenation are of value in addressing these apparent inconsistencies. We present a record of redox-sensitive uranium from the central equatorial Pacific to identify intervals associated with respiratory carbon storage

[1]Authors: A.W. Jacobel[a*], J.F. McManus[a], R.F. Anderson[a] G.Winckler[a] [a] Department of Earth and Environmental Sciences, and Lamont-Doherty Earth Observatory of Columbia University, 61 Route 9W, Palisades, NY 10964, USA

* corresponding author: jacobel@ldeo.columbia.edu

over the past 350 kyr and find evidence for repeated carbon storage over the last three glacial cycles. We also synthesize our data with previous work and propose an internally consistent picture of glacial carbon storage and equatorial Pacific watermass structure.

4.1 Introduction

Glacial-interglacial climate cycles are well characterized in the late Pleistocene where records of pCO_2 and other greenhouse gases are available from gases trapped within ice cores (Members, 2004). These ice archives reveal pCO_2 variations of 80- to 100-ppm on timescales of approximately 100 kyr with smaller but significant variance in the 41 and 23 kyr frequency bands. While several hypotheses have been proposed to explain the repeated drawdown and release of atmospheric CO_2, it is generally agreed that viable explanations must include carbon storage in the deep ocean (Broecker, 1982; Sigman and Boyle, 2000; Sigman et al., 2010). Key to answering questions about how and where marine carbon storage occurred during glacial periods is an understanding of deep ocean circulation, which, in combination with biological processes (productivity and respiration), is responsible for the distribution of CO_2, O_2, nutrients, and alkalinity in the ocean basins (Boyle, 1988b). Studies aiming to quantify variability in these parameters on paleo-timescales have emphasized the roles of the Southern Ocean(e.g., Jaccard et al., 2016; Martínez-Garcia et al., 2009, 2014; Sprenk et al., 2013; Yu et al., 2014) and the deep Pacific Ocean (e.g., Anderson et al., 2008; Bradtmiller et al., 2010; Broecker and Clark, 2010; Broecker et al., 2004; Jaccard and Galbraith, 2012; Jaccard et al., 2009; Korff et al., 2016; Mekik et al., 2012; Mills et al., 2010). The Antarctic Zone of the Southern Ocean is of particular interest because it is the place where the 'biological pump', which removes surface nutrients and carbon to depth, shows the greatest potential for increased efficiency relative to modern observations (Martínez-Garcia et al., 2014; Studer et al., 2015). The Pacific Ocean is of major significance because volumetrically it has the capacity to hold almost as much water and CO_2 as all the other ocean basins combined and, due to the routing pathway of deep water, its northernmost reaches represent the oldest, most CO_2 enriched waters in the ocean (Key et al., 2004). Although there has been considerable dispute about the role of the Pacific in glacial carbon

storage (Broecker and Clark, 2010; Broecker et al., 2008), previous work in the Subarctic and equatorial Pacific has been interpreted as showing evidence of reduced oxygen concentrations (Bradtmiller et al., 2010; Galbraith et al., 2007; Jaccard and Galbraith, 2012; Jaccard et al., 2009, 2014; Korff et al., 2016; Mills et al., 2010), higher dissolved inorganic carbon (DIC) concentrations (lower $\delta^{13}C$) (Galbraith et al., 2007; Herguera et al., 1992; Keigwin, 1998; Matsumoto et al., 2002), and calcium carbonate dissolution (increased alkalinity) (Anderson et al., 2008; Galbraith et al., 2007; Jaccard et al., 2009) in concert with lower or similar local export productivity (Bradtmiller et al., 2010; Costa et al., 2016; Jaccard et al., 2009; S. S. Kienast et al., 2006; Loubere, 2000; Pichat et al., 2004; Winckler et al., 2016) during the Last Glacial Maximum (LGM) relative to Holocene levels. In concert, the data suggest that Pacific waters below ~2 km had higher concentrations of remineralized carbon during the last ice age (Herguera et al., 1992; Jaccard et al., 2009, 2014; Matsumoto et al., 2002; Sarnthein et al., 2013), representing deep ocean sequestration of CO_2 primarily due to changes in the efficiency of the upstream biological pump, and increased Antarctic water mass stratification, rather than local changes in productivity. These findings are consistent with the original 'nutrient deepening hypothesis' (Boyle, 1988a,b) for enhanced oceanic carbon storage during the last ice age. They are also explained comprehensively by the 'respired carbon deepening hypothesis' (Jaccard and Galbraith, 2012; Jaccard et al., 2009, 2014), a modification that accounts for Cd/Ca proxy data showing relatively invariant deep water phosphate concentrations between the LGM and the Holocene in the deep Pacific (Boyle, 1992). The latter hypothesis, by Jaccard and co-authors (Jaccard et al., 2009), proposes that during the last glacial period the ocean's 'biological pump' was more efficient, particularly in deep water source regions, with more complete utilization of macronutrients in the surface ocean contributing to lower concentrations of pre-formed nutrients in the deep sea. Reducing the inventory of preformed nutrients with a constant inventory of total nutrients indicates a corresponding rise in the inventory of regenerated nutrients, raising the respired CO_2 concentration at depth, effectively sequestering carbon (Sigman et al., 2010). In contrast, during the Holocene, nutrient utilization was less efficient, resulting in a reduction of respired carbon storage at depth, with the consequent transfer of carbon from the deep sea to the atmosphere. The respired carbon deepening hypothesis

combines Cd/Ca, δ^{13}C, authigenic uranium (aU), δ^{15}N, bioBa and opal data from the last glacial period into an internally consistent framework, and in doing so poses important questions about deep ocean carbon sequestration on longer timescales. For instance, **1)** is deep ocean carbon storage a repeated feature of glacial periods? **2)** Does deep ocean oxygen limitation occur solely in concert with glacial maxima? **3)** How do relatively more brief intervals of decreased atmospheric pCO_2 such as Marine Isotope Stage 7d (MIS 7.4) manifest in records of deep ocean oxygenation? To address these questions we reconstructed a record of U- and Th-series isotopes (^{238}U, ^{234}U, ^{232}Th and ^{230}Th) from site ML1208-17PC (hereafter 17PC) in the Line Islands archipelago of the central equatorial Pacific (Figure 4.1). The core site (0.48°N, 156.45°W) sits at a water depth of 2,926 m and at present is bathed by North Pacific Deep Water (NPDW) with a local oxygen content of ~136 μmol kg^{-1}, phosphate concentration of ~2.6 μmol kg^{-1} and apparent oxygen utilization (AOU) of ~200 μmol kg^{-1} (Key et al., 2004). Surface waters at 17PC are derived from upwelling of the Equatorial Undercurrent (EUC) which originates from the mixing of South and North Pacific Subtropical Mode Water, Subtropical Cell Waters and Subantarctic Mode Water (Rafter et al., 2012; Toggweiler et al., 1991).

Here we present aU results from site 17PC spanning the last three glacial cycles at millennial resolution. Our reconstruction expands the published aU data coverage to include the central equatorial Pacific and shows North Pacific Deep Water had significantly lower oxygen concentrations than at present during MIS 2, 4, 6 and 8. We also provide a perspective on watermass structure to reconcile our results with 1) data interpreted as suggestive of no increase in Pacific storage of respired carbon during the LGM (Broecker and Clark, 2010), 2) previously inconclusive data on bottom water oxygen state from 140°W (Anderson et al., 2006; Winckler et al., 2008) and 3) results taken to indicate that Lower Circumpolar Deep Water was the sink for respired carbon (Keigwin and Lehman, 2015). Finally, we discuss our reconstruction of deep water oxygen history in the context of changes in global climate and pCO_2. Our results provide evidence that the deep Pacific was an active reservoir for respired carbon during glacial periods of at least the last 350 kyr.

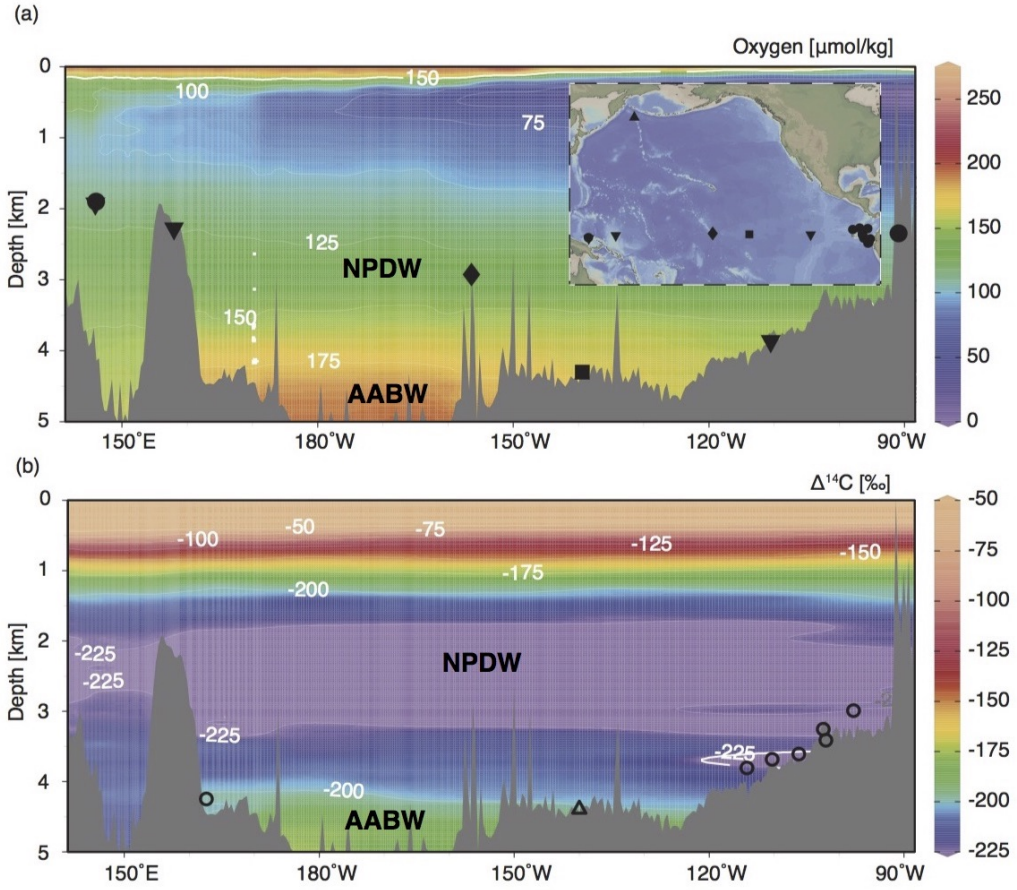

Figure 4.1: Modern oxygen concentrations in μmol kg^{-1} (Key et al., 2004) with the locations of Pacific records of bottom water oxygen as recorded by aU from ML1208-17PC (this study) (diamond), RC11-238 and RC13-140 (Bradtmiller et al., 2010) (dots), TT013-PC72 (Anderson et al., 2006; Winckler et al., 2008) (square), ODP 849 and MD97-2138 (Pichat et al., 2004) (inverted triangles) and ODP 882 (Jaccard et al., 2009) (triangle) (a). The lower panel shows modern Δ^{14}C-concentrations (Key et al., 2004) with radiocarbon from TTN013-18 (Broecker and Clark, 2010) (open triangle), and GS7202-15, PLDS 7G, VNTR01 10 GC, KNR73 3PC, KNR73 4PC, KNR73 6PG and S67 15FFC (Keigwin and Lehman, 2015) (open circles). Note that the other ML1208 core sites discussed in this manuscript are at approximately the same longitude and depth as site 17PC. The labels NADW and AABW indicate North Atlantic Deep Water and Antarctic Bottom Water respectively. Basemaps made using Ocean Data View.

4.2 Results

A record of aU was derived for 17PC (Figure 4.2 and Figure 4.3) on the basis of measured ^{238}U and ^{232}Th activities and is presented alongside previously analyzed (Jacobel et al., 2017) records of aU from ML1208 sediment cores 37BB and 31BB in Figure 4.2a. Uranium is a redox-sensitive metal and is present in oxygenated seawater as soluble uranyl carbonate (Langmuir, 1978). At the seafloor, inorganic precipitation of U may occur within the porewater of sediments under conditions where the combination of low bottom water oxygen concentrations together with in situ respiration drive the sediments to anoxia and to a redox state of iron reduction (Anderson et al., 1989; Cochran et al., 1986; Klinkhammer and Palmer, 1991; J. McManus et al., 2005; Morford et al., 2005; Zheng et al., 2002a). The record of aU from site 17PC shows low frequency variability in the range of 0-0.5 ppm with periodic, abrupt increases in aU reaching values of 2-3 ppm. Large (>1ppm) peaks of aU are observed at 34.4 and 56.3, 138.8, 161.4, 254.2 and 268.6 ka, appearing during glacial maxima, just prior to deglacial boundaries during intervals of increased northern hemisphere glaciation (Figure 4.3). The maximum aU concentrations reported here are within the range of those observed during the LGM at sites from the eastern equatorial Pacific (west of 83.6°W) (Bradtmiller et al., 2010; S. S. Kienast et al., 2007; Yang et al., 1995) and subarctic North Pacific (Jaccard et al., 2009), but are approximately an order of magnitude higher than maximum concentrations measured at TT013-PC72 (0.1°N, 139.4°W; 4,300 m depth) (hereafter PC72) (Anderson et al., 2006; Winckler et al., 2008) (Figure 4.2b), less than 20° (2,220 km east) of our site. We reconcile these differences with respect to watermass in the following subsection on paleocirculation.

4.3 Discussion

4.3.1 Authigenic uranium

Concentrations of aU in core 17PC are substantially greater than would be expected if the uranium present was derived solely from uranium incorporation into foraminiferal calcite or organic material (Methods) (Figure 4.2). Instead, we propose that the primary determinant of aU abundance at site 17PC is the redox state of the sedimentary environment. Thus, the

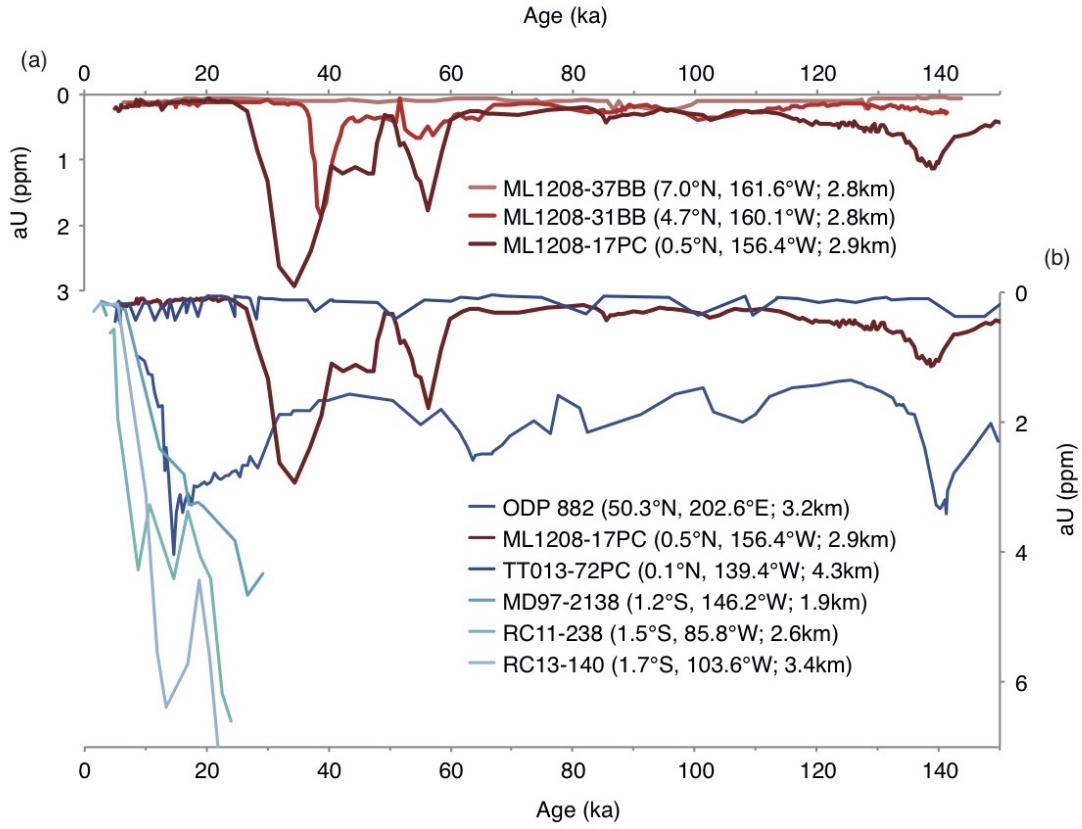

Figure 4.2: Sedimentary aU records from ML1208 sediment cores 17PC (dark red), 31BB (red) and 37BB (lightest red) (a). Comparison of aU records from the Pacific Ocean including 17PC (this study-dark red), ODP 882 (Jaccard et al., 2009), TT013-72PC (Anderson et al., 2006; Winckler et al., 2008), MD97-2138, RC11-238 and RC13-140 (Bradtmiller et al., 2010) with colors and locations as depicted in the figure legend (b).

precipitation of aU at site 17PC is (and was) likely controlled by the combined influence of bottom water oxygen supply and the rate of oxygen consumption, as determined by the respiration of organic matter. Accordingly, the precipitation of aU may either have been driven by a decrease in the supply of oxygen from bottom waters, or by an increase in respiration due to a larger flux of organic material from the overlying surface waters. The abyssal waters bathing site 17PC (NPDW) were most recently at the surface in the Southern Ocean, and therefore any decrease in ventilation rate or increases in respiration along the flow pathway could reduce oxygen delivery to the central equatorial Pacific. Alternatively, aU precipitation at 17PC might be favored if the rain of organic material and associated respiration at depth increased locally during glacial periods, with no change in ventilation required. Here we investigate these two possibilities.

Abundant proxy data including opal fluxes, excess barium fluxes, $^{231}Pa/^{230}Th$ ratios and the $\delta^{15}N$ of planktonic foraminifera characterize the last glacial period as having similar or lower export productivity than during the Holocene interglacial at 160°W in the central equatorial Pacific (Costa et al., 2016), as well as further to the west (Pichat et al., 2004) and much of the east (Costa et al., 2017; Winckler et al., 2016). In the absence of increased biogenic fluxes, higher aU abundance during the last glacial period must therefore be controlled primarily by decreased bottom water oxygen concentrations. This decreased $[O_2]$, in combination with respiration at a relatively invariant background level, lowered the redox state of porewaters to the point of iron reduction, allowing for the precipitation of aU.

Further evidence for deep ocean oxygen changes as the crucial control on aU precipitation during the last glacial period comes from a comparison of the record of 17PC to the other ML1208 sediment cores. Figure 4.2a illustrates that the amount of aU in the sediments decreases northwards away from the equator (from 17PC to 31BB to 37BB). This observation is consistent with the decreasing export of organic carbon away from the equator, as expected due to depletion of nutrients as waters mix poleward from their upwelling source at the equator. Indeed, site 37BB appears to have such a low organic export flux that conditions for aU precipitation are not reached over at least the last 150 kyr. Bottom water oxygen levels are likely to have changed synchronously at these ML1208 sites because

of their close proximity in space and depth, so we attribute the northward decrease in aU to the corresponding decrease in organic carbon rain, decreasing the respiration in the sediments. Indeed, Figure 4.2a shows the timing of aU maxima in 17PC and 31BB to be similar. This comparison confirms a threshold level of organic carbon respiration to be a necessary but not sufficient condition for aU precipitation, and shows that for aU precipitation to occur an additional lowering of bottom water oxygen concentrations via ventilation change is required.

At present no flux-normalized data on export productivity extending beyond the last glacial maximum are available from 160°W. Fortunately, flux-normalized records of barium excess, representing organic carbon export exist from site PC72 at 140°W (Winckler et al., 2016). Because surface productivity at site PC72 is also fed by the EUC, surface waters at 17PC and PC72 have zonally homogenous nutrient concentrations (Rafter et al., 2012; Winckler et al., 2016). We observe little difference between the present day nutrient profiles of water upwelled at the two sites (Rafter et al., 2012) and expect any past changes in the properties of EUC source waters to have affected both sites similarly.

Productivity data from site PC72 (Figure 4.3c) confirm the observation from the Line Islands area that productivity during the last glacial and LGM was lower in the central equatorial Pacific relative to Holocene levels. Generally, the record shows relatively little variability between glacial and interglacial periods. Indeed, late MIS6 and early MIS5 export fluxes appear similar, as do those during late MIS8 and MIS7. Most importantly, there are no detectable increases in productivity coincident with increases in aU. The lack of concordance between observed records of EUC-driven export production in comparison with aU indicates local changes in organic carbon export were not the primary factor regulating aU precipitation during glacial periods. Instead, we infer that peaks of aU precipitation during the last three glacial cycles resulted from a decrease in advected bottom water oxygen concentrations which brought post-respiration porewater redox levels below the threshold for aU precipitation.

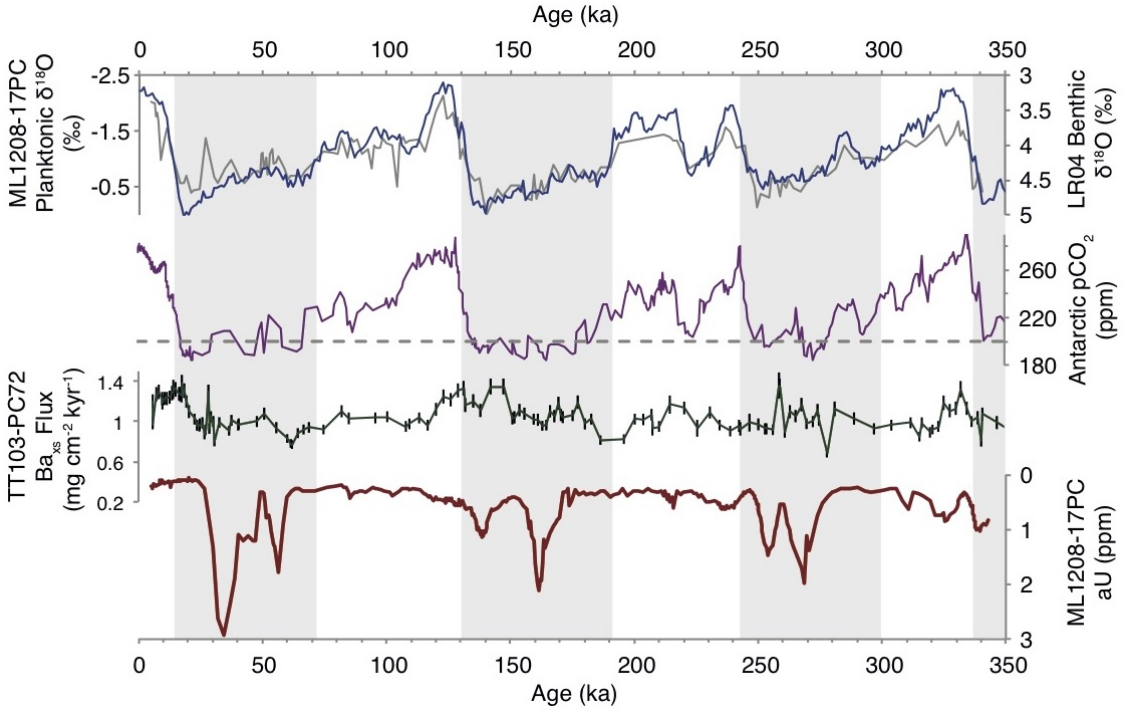

Figure 4.3: Benthic oxygen isotope stack (blue) (Lisiecki and Raymo, 2005) and local planktonic oxygen isotope stack from ML1208-17PC (grey) (this study) (a). Composite of Antarctic pCO_2 records (Lüthi et al., 2008) (b). Central equatorial Pacific (TT013-PC72) excess barium fluxes (dark green) with 1 sigma error bars (Winckler et al., 2016) (c). Authigenic uranium concentrations from site 17PC in the central equatorial Pacific (note the inverted y-axis) with average 1 sigma error bar indicated (d). All Antarctic records are on the AICC2012 age model (Veres et al., 2013) and all other records are as originally published.

4.3.2 Burndown

In contrast with other records from the Pacific basin which show maximum aU fluxes between 27-15 ka (Bradtmiller et al., 2010; Jaccard et al., 2009) (Figure 4.2b), our record from 17PC in the central equatorial Pacific shows a peak of uranium precipitation nominally occurring at ~34 ka. While the late aU peak at ODP 882 in the Subarctic North Pacific can likely be attributed to a late deglacial productivity pulse (Jaccard et al., 2009; Ren et al., 2015), other records from the equatorial Pacific (MD97-2138, RC110238 and RC13-140) (Bradtmiller et al., 2010) suggest aU precipitation was ongoing at these sites until late in the deglaciation (Figure 4.2b). Although it is possible that redox conditions were spatially and temporarily variable across the glacial equatorial Pacific, we propose the difference is more likely due to post-depositional alteration of the Line Islands records at 17PC and 31BB following the LGM.

Diagenetic alteration of aU down core may occur in sediments after an increase in oxygen at the sediment-water interface, as would occur following a reinvigoration of deep water ventilation. As oxygen diffuses into porewaters it creates a front where organic carbon stock is oxidized and aU is dissolved into solution (Colley et al., 1989). Once dissolved, aU may either be lost to seawater or diffuse deeper into the sediment where anoxic conditions persist and the U can be re-precipitated. We suggest that during the Holocene, oxygenation of bottom waters caused the removal of aU as much as 50 cm down core at site 17PC. This magnitude of oxygen penetration is well within the observed range of sedimentary oxygen diffusion (e.g., Mills et al., 2010) and would account for the temporal difference between the aU peak in the record from 17PC and those records from the eastern and western equatorial Pacific (Bradtmiller et al., 2010), where the much larger sediment accumulation rates limit the time interval over which burndown may have affected the aU record.

Further evidence that the latest MIS2 peak in 17PC represents loss of aU comes from comparing the timing of corresponding peaks in cores 17PC and 31BB (Figure 4.2a). The LGM aU peak at 31BB appears to occur before that at 17PC (~40 ka versus ~34 ka), as might be expected if Holocene oxidation of LGM-deposited organic carbon occurred at approximately the same magnitude at both sites. Since 31BB has a lower organic carbon rain (due to its off equator position), post transition re-oxidation would occur at a greater

rate and to a deeper depth (and correspondingly older age) at site 31BB relative to site 17PC. This expectation matches our observations, suggesting that the latest MIS2 peaks in both 31BB and 17PC are a consequence of post depositional alteration of the aU signal.

Indications of down core aU mobilization during the LGM portion of our record raise the question of whether the double peaks observed within MIS 2, 6 and 8 (specifically the early glacial peaks) might be related to post-depositional sedimentary processes. Based on the abundance of uranium-238's daughter isotope, thorium-230, we provide evidence that this is not the case. Instead we suggest both early and late glacial aU peaks are original to the depth intervals in which they are measured and if anything, represent peaks of a smaller magnitude than those originally precipitated in situ.

Examination of U and Th isotope abundances in 17PC reveals that the apparent $^{230}Th_{xs,0}$ concentrations show an unexpected, positive correlation with authigenic ^{238}U (see Methods-Use of $^{230}Th_{xs,0}$). We illustrate this relationship in detail using the example of MIS 8 (Figure 4.4) but note that the same relationship holds for all aU peaks except the most recent LGM interval (in which it may still be developing). The association of high $^{230}Th_{xs,0}$ and authigenic ^{238}U could be due to very low particle accumulation rates coinciding with aU deposition. An alternative explanation, one which we consider more likely, is that ^{238}U was oxidized and subsequently lost to the water column some time after authigenic precipitation. Post depositional loss of ^{238}U would lead to the 'abandonment' of its daughter isotope, causing the appearance of anomalously high $^{230}Th_{xs,0}$ concentrations. Given that aU is readily mobilized to porewaters upon oxidation (Shaw et al., 1994) and can be lost to the water column (Colley et al., 1989), we propose that high $^{230}Th_{xs,0}$ concentrations reflect post-depositional oxidation and removal of aU 10-20 kyr after initial precipitation (Supplementary Note 1 and Supplementary Figure 4.6). This duration of ^{238}U decay prior to dissolution would be consistent with either a temporary re-oxygenation of bottom waters between periods of low oxygen (as suggested by the aU record), or a deglacial re-oxygenation of deep waters. In sum, evidence from unusually high $^{230}Th_{xs,0}$ concentrations indicates that not only does the aU in core 17PC reflect original deposition in situ, but it is likely that the initial aU concentration was actually higher than observed at present due to some intervening loss to seawater.

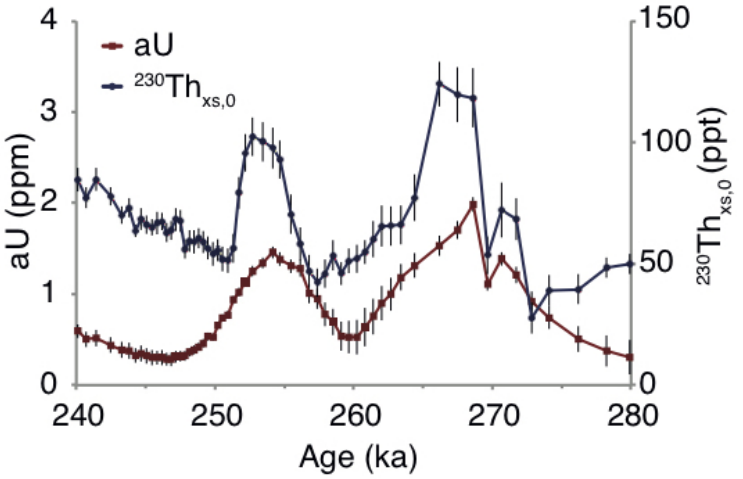

Figure 4.4: Records of aU (red) and $^{230}\mathrm{Th}_{xs,0}$ (blue) from site 17PC over MIS 8. Error bars represent 1 sigma uncertainties.

4.3.3 Insights into watermass geometry

A substantial body of research has focused on evaluating the evidence for a glacial reservoir of carbon in the deep Pacific and on defining its extent. Here, we propose a picture of glacial watermass stratification reconciling apparently inconsistent data from the deep central (Anderson et al., 2008; Broecker and Clark, 2010; Winckler et al., 2008) and eastern Pacific (Keigwin and Lehman, 2015; Mills et al., 2010). At present, the deep equatorial Pacific is occupied by two main watermasses, NPDW and Antarctic Bottom Water (AABW). Southward flowing NPDW occupies depths between ~2 and 4 km while the deepest Pacific is bathed by northward flowing Antarctic Bottom Water (AABW). As might be predicted given the flow pathways of these two watermasses, NPDW is relatively older and less oxygenated than the underlying AABW (Figure 4.1). Last Glacial Maximum grain size data from the North Chatham drift in the southern Pacific indicate increased formation of AABW and inflow to the Pacific (Hall et al., 2001). Although the fraction of North Atlantic Deep Water in AABW was likely different during the LGM, stronger AABW flow would have provided a source of relatively more recently ventilated waters to the deepest Pacific, similar to

the present configuration. This interpretation is supported by records of aU from sites PC72 (Anderson et al., 2006; Winckler et al., 2008) (Fig 3d) and ODP 849 (Pichat et al., 2004) (not pictured). These deep Pacific sites (at 4.3 km and 3.8 km respectively) demonstrate neither the concentration nor structure of aU observed in other records from the Pacific. Whatever the oxygen concentration in northward flowing bottom waters during glacial periods, if glacial circulation followed a pattern similar to that which exists today then the apparent inconsistency between the deepest Pacific records of aU accumulation (PC72 and ODP 849) and our work (and the work of Bradtmiller et al., 2010 and Mills et al., 2010) could be easily understood as the result of sampling sites bathed by different watermasses. This hypothesis is supported by LGM radiocarbon data from the eastern equatorial Pacific (Keigwin and Lehman, 2015), central equatorial Pacific (Broecker and Clark, 2010) and south Pacific (Ronge et al., 2016) which together indicate that the watermass below ~3.5 km (3.8 km in the eastern equatorial Pacific) was more recently ventilated (younger) than the overlying watermass. Specifically, a stratification structure similar to present day would readily explain the absence of a significant surface to deep (~4.4 km) radiocarbon gradient at the LGM (Broecker and Clark, 2010). The majority of existing estimates for the upper bound of glacial NPDW come from North Pacific δ^{13}C data and indicate a watermass high in respired carbon (low δ^{13}C) as shallow as 2 km (Herguera et al., 1992; Matsumoto et al., 2002). In the equatorial Pacific the estimates for LGM NPDW are from 1.9 (Bradtmiller et al., 2010)-2 km (Herguera et al., 1992) in the western portion of the basin and 2 (Herguera et al., 2010)-2.2 km (Bradtmiller et al., 2010) in the east. Combining these estimates of the bounds of NPDW suggests the LGM watermass may not have occupied a significantly different depth range than at present. Instead, the more significant glacial change appears to have been to the watermass properties.

4.3.4 Implications for respired carbon storage

The observation of aU peaks during the last three glacial periods in the absence of concurrent increases in organic carbon fluxes supports the conclusion that respired carbon storage in the deep Pacific has been a recurrent feature of at least the last three ice ages. The timing of repeated aU maxima indicates that the deep ocean may have been periodically

oxygen-limited during glacial periods as a consequence of increased respired carbon storage and decreased rates of ocean ventilation. Our conclusions about bottom water oxygen concentrations are in agreement the findings and interpretation of previous studies of aU over the last ~20 (Bradtmiller et al., 2010) and ~150 kyr (Jaccard and Galbraith, 2012; Jaccard et al., 2009) which concluded that the Pacific stored a large volume of respired carbon during the last glacial period. Our data are also consistent with conclusions about bottom water oxygen concentrations derived from a site on the East Pacific Rise (Mills et al., 2010), but our proxy appears to be a more sensitive measure of deep water conditions as aU records not just one, but multiple intervals of low oxygen during each of the last three glacial periods. Our data indicate the conditions in equatorial Pacific sediments at ~3 km water depth that allowed authigenic uranium deposition were closely associated with an atmospheric pCO_2 concentration of ~200 ppm (Figure 4.3b) with some range in sensitivity attributable to the variable influence of marine organic productivity and the biogeochemical activity of the terrestrial biosphere (Claussen, 2009). It is possible that brief intervals of low oxygen abundance (for example a possible event during MIS 7d) are not well preserved in the core due to post-precipitation oxidation. Additional work on higher sedimentation rate sites (eg ML1208-31BB) may help to resolve this question. Our new record highlights the significance of the deep Pacific as a reservoir for lowering atmospheric pCO_2 during glacial periods and suggests mechanisms responsible for increasing the DIC burden of the basin are active components of the climate system over at least the last 350 kyr.

4.4 Conclusions

Our new record of sedimentary authigenic U from the central equatorial Pacific strengthens the body of evidence that vast areas of the deep Pacific, including the central (this study), eastern (Bradtmiller et al., 2010; Mills et al., 2010), western (Bradtmiller et al., 2010), north (Galbraith et al., 2007; Jaccard and Galbraith, 2012; Jaccard et al., 2009, 2014; Korff et al., 2016), and south (Ronge et al., 2016) Pacific, were reservoirs for respired carbon during the last three glacial cycles. In contrast with previous work (Broecker and Clark, 2010; Keigwin and Lehman, 2015), we infer a 'floating' pool of respired carbon between 2 and 3.5 km depth

in the central equatorial Pacific and conclude that existing proxy data reflecting LGM deep water circulation and carbon storage can be reconciled without invoking a significantly different glacial watermass structure in the central equatorial Pacific. Although data are still too sparse to extend our conclusions to the last three glacial cycles, we hypothesize that further research will demonstrate this finding to be robust on longer timescales (Korff et al., 2016; Mills et al., 2010). Our observation that the precipitation of aU at site 17PC is associated with an atmospheric concentration of ~200 ppm pCO_2, raises the question of what bottom water oxygen concentration(s) are related to this apparent threshold. While our data conclusively identify the existence of an oxygen-poor, carbon-rich watermass in the Pacific, future work to quantitatively determine the oxygen content (as previously done for the Atlantic (Gottschalk et al., 2016; Hoogakker et al., 2015a; Hoogakker et al., 2015b) is essential for determining the precise timing and spatio-temporal extent of respiratory carbon storage.

4.5 Methods

4.5.1 Study site

This study presents records of U- and Th-series isotopes (^{238}U, ^{234}U, ^{232}Th and ^{230}Th) reconstructed from sediment core ML1208-17PC collected from the Line Islands archipelago of the central equatorial Pacific (Figure 4.1). Sediments at site 17PC are foraminifera oozes with low organic and terrigenous components. Age-depth relationships for 17PC were constrained using δ^{18}O isotope ratio constraints from the planktonic foraminifera G. ruber (Lynch-Stieglitz et al., 2015) and previously published radiocarbon dates (Jacobel et al., 2017). The isotope stratigraphy was tuned to the LR04 benthic stack (Lisiecki and Raymo, 2005) using a Monte-Carlo-enabled cross-correlation maximization scheme coupled with a random walk algorithm known as MonteXCM (Hoffman et al., 2015). Age-depth control points specified by MonteXCM were refined in Bchronology (Haslett and Parnell, 2008) to better constrain age uncertainties. Sedimentation rates average 2.1 cm ka^{-1} with age uncertainties of ± 2.3 ka (1σ) (Supplementary Figure 4.5). The age model presented here is consistent with the most recently published version for 17PC (Jacobel et al., 2017) but

varies slightly from that originally published (Lynch-Stieglitz et al., 2015) due to improved age control.

4.5.2 Radiogenic isotope measurements

New data presented in this study are 216 U and Th isotope measurements from core 17PC analyzed by isotope dilution on an Element 2 ICP-MS at the Lamont-Doherty Earth Observatory of Columbia University. For each depth interval ~200 mg of sediment was spiked with ^{236}U and ^{229}Th prior to dissolution and digestion using HNO_3, HF and $HClO_4$, following methods outlined in (Fleisher and Anderson, 2003). The U and Th fractions were concentrated using anion exchange column chemistry following the adsorption behaviors observed by (Kraus et al., 1956). An internal standard with similar chemical and physical properties to sediments at site 17PC was evaluated with each batch of samples to determine data reproducibility with resulting relative standard deviations of 1.8%, 1.4%, 1.0% and 3.5% for ^{238}U, ^{234}U, ^{230}Th and ^{232}Th respectively. Background levels of U and Th were evaluated for each batch using blanks processed alongside samples but containing no sediment. Results show blanks for all isotopes at less than 0.5% of even the lowest sample values. We report uncertainties calculated for each data point at the 1-sigma level, including the propagated uncertainty due to counting statistics, the mass bias correction, counting gain, spike measurements and the fraction of the sediment derived from lithogenic source material (e.g., Bradtmiller et al., 2010; Francois et al., 2004; J. F. McManus et al., 1998). Additional U and Th data from sediment cores ML1208-37BB (7.04°N, 161.63°W; 2,798 m water depth) and ML1208-31BB (4.68°N, 160.05°W; 2,857 m water depth) are presented alongside the new data from 17PC, but were originally part of (Jacobel et al., 2017).

4.5.3 Authigenic uranium proxy systematics

Uranium is a redox-sensitive metal and is present in oxygenated seawater as soluble uranyl carbonate (Langmuir, 1978). In the upper water column, particulate U is generally associated with either detrital silicates or with organic carbon (Anderson, 1982), although a small amount of U (~0.012–0.036 ppm) can be incorporated into the calcite tests of foraminifera (Russell et al., 2004). As particles descend through the open ocean water column most

U precipitated in conjunction with Corg is remineralized, although this recycling process appears to be less efficient at the ocean margin where dissolved oxygen concentrations can be much lower than in typical open ocean settings (Anderson, 1982; Zheng et al., 2002b). At the seafloor, two more processes may contribute U to the sediments. First, inorganic precipitation of U may occur within the porewater of sediments under conditions of complete anoxia accompanied by iron reduction. This process occurs due to the reduction of U(VI) to U(IV) by iron reducing bacteria (Finneran et al., 2002). As the precipitation of reduced uranium proceeds, a concentration gradient may form between the high [U] seawater and low [U] porewater, creating a diffusive flux into the sediment that can generate intervals of high U (Bradtmiller et al., 2010; Jaccard et al., 2009; Klinkhammer and Palmer, 1991). Authigenic precipitation in porewaters is thought to be the most important (~75%) mechanism of U removal in the ocean (Klinkhammer and Palmer, 1991; J. McManus et al., 2005). A second mechanism of sedimentary U addition at the seafloor is precipitation in association with hydrothermal vent systems (Mills et al., 2010). These processes remove U from seawater and constitute a significant global sink of U, although the impact of hydrothermal removal is restricted to near-ridge environs and does not influence the study site addressed here. Despite the geochemical complexity of U deposition in sediments, U is typically characterized as either detrital/lithogenic (of terrestrial origin) or authigenic (of marine origin). In the central equatorial Pacific lithogenic U is transported via the same aeolian processes delivering ^{232}Th and thus can be constrained using the empirically determined activity ratio between lithogenic or detrital ^{238}U and ^{232}Th (0.7 ± 0.1) for the Pacific (Henderson and Anderson, 2003) such that $^{238}U_{detrital}$=0.7*$^{232}Th_{meas}$, and all additional U not lithogenic in origin is considered to be authigenic (aU).

4.5.4 Use of $^{230}Th_{xs,0}$

Thorium-230 may be introduced to the sediment in two ways: via the decay of particulate uranium (of either detrital or authigenic origin), or via scavenging of ^{230}Th onto particles as they descend through the water column. The former ^{230}Th (ingrowth from radioactive decay) is referred to as supported ^{230}Th, whereas the latter is considered unsupported or excess (xs). Excess ^{230}Th is decay corrected to quantify the initial $^{230}Th_{xs}$ ($^{230}Th_{xs,0}$).

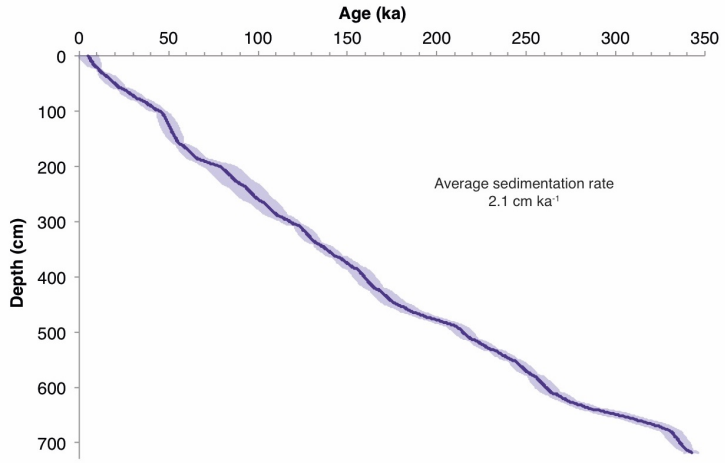

Figure 4.5: Data for core ML1208-17PC (purple line) with shading indicating two sigma uncertainty (95% confidence intervals) for the age model. The accumulation rate depicted on the figure is the average for the 350 kyr interval discussed here.

Changes in the concentration of $^{230}Th_{xs,0}$ are primarily a function of dilution by other sedimentary constituents (e.g.: organic matter, lithogenic particles, and calcium carbonate).

4.6 Supplementary Notes

4.6.1 Daughter isotope 'abandonment'

We propose that high $^{230}Th_{xs,0}$ concentrations coincident with aU peaks reflect post-depositional oxidation and removal of aU 10-20 kyr after its initial authigenic precipitation. This hypothesis is supported by the observation of ongoing oxidation of the LGM aU peak (a process similar to that which likely affected the relict aU peaks), and the observation that bottom waters became re-oxygenated during periods of increased ventilation following the deposition of the glacial aU peaks. Our hypothesis of post emplacement ^{238}U dissolution and ^{230}Th daughter isotope 'abandonment' finds additional support in a modeling experiment designed to verify a range of these dissolution scenarios. We evaluate these scenarios by assessing the changing correlation between aU and $^{230}Th_{xs}$. The data as measured show a positive correlation between aU and $^{230}Th_{xs}$. This is an unexpected relationship with no

physical basis and the observation of such a relationship in the data is strongly indicative of post depositional dissolution of aU and subsequent under correction for ^{230}Th ingrowth. We expect the correlation between aU and $^{230}Th_{xs}$ in the model to be near zero when we identify a realistic scenario of aU dissolution and daughter isotope 'abandonment'.

In our experiments we varied three parameters: **1)** the hypothesized original aU concentration, **2)** the time elapsed between aU emplacement and dissolution, and **3)** the concentration threshold above which aU is dissolved. To simplify the calculation we assume that all of the ^{238}U present is authigenic. This is reasonable simplifying assumption because on average the contribution of detrital ^{238}U to the total ^{238}U is ~0.7/

Supplementary Figure 4.6 illustrates two different iterations of the modeling experiment for the same interval depicted in Figure 4.4. Panels a (solid lines) and b illustrate the positive correlation between aU and $^{230}Th_{xs}$ prior to correction for aU dissolution. Panels a (dotted lines) and c show the results of an experiment in which intervals with an aU concentration above 0.5 dpm g^{-1} undergo dissolution to two-thirds of their initial concentrations 15 ka after the time of aU precipitation. Accounting for this history of aU precipitation and subsequent dissolution would result in the $^{230}Th_{xs}$ time series represented by the dotted blue line. The relationship between the hypothesized $^{230}Th_{xs}$ time series and the observed time series of aU in Panel c shows no correlation (as expected). Panel d depicts the results of an experiment in which intervals with an aU concentration above 0.8 dpm g^{-1} undergo dissolution to two-thirds of their initial concentrations 20 ka after the time of aU precipitation. Accounting for this history of aU precipitation and subsequent dissolution would result in the $^{230}Th_{xs}$ time series represented by the dotted blue line. The relationship between this hypothetical $^{230}Th_{xs}$ time series and the observed time series of aU (Panel e) shows no correlation (again, as expected).

Our modeling results demonstrate that time series of $^{230}Th_{xs}$ uncorrelated with ^{238}U (aU) can be obtained by substituting realistic parameter values into our model. We consider these results an additional line of evidence that aU has been removed from the relict aU peaks at some time after deposition. Based on our experimentation we find it likely that approximately two-thirds of the initially precipitated aU was dissolved 15-20 kyr after emplacement, 'abandoning' ^{230}Th. This process leads to an overestimate of $^{230}Th_{xs}$.

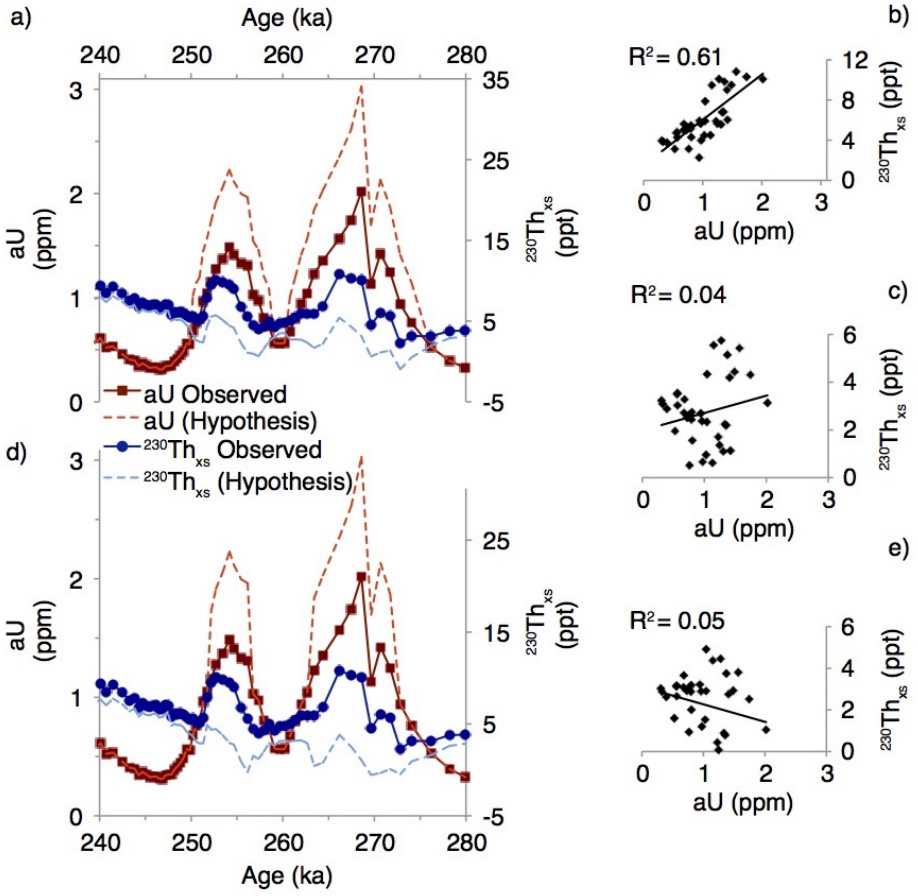

Figure 4.6: Here we show two different scenarios of post-depositional aU dissolution. Panel (a) shows the results of an experiment in which intervals with an aU concentration above 0.5 dpm g^{-1} undergo dissolution to two-thirds of their initial concentrations, 15 ka after the time of aU precipitation. Panel (b) shows the observed correlation between $^{230}Th_{xs}$ and aU in the data as measured. Panel (c) shows the same correlation but for the hypothetical $^{230}Th_{xs}$ and aU data. Panel (d) depicts the results of an experiment in which intervals with an aU concentration above 0.8 dpm g^{-1} undergo dissolution to two-thirds of their initial concentrations 20 ka after the time of aU precipitation. Panel (e) shows the correlation between hypothetical $^{230}Th_{xs}$ and aU data. In Panels a and b the observed aU (maroon) and $^{230}Th_{xs}$ (navy) data are displayed with solid lines and symbols and the hypothesized original values of aU (red) and $^{230}Th_{xs}$ (blue) are shown with dotted lines.

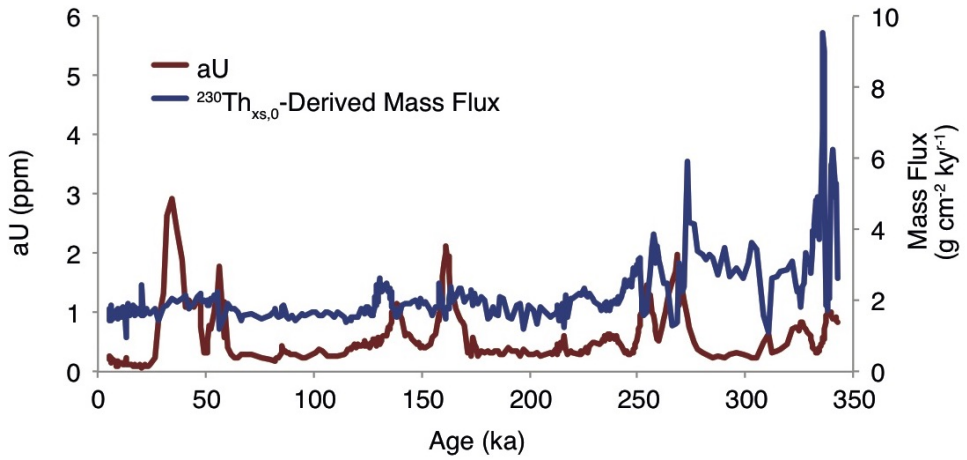

Figure 4.7: Mass fluxes, derived from $^{230}\mathrm{Th}_{xs,0}$, for the last 350 kyr from 17PC (blue line). The anticorrelation between mass flux and aU concentration (red line) is evident especially for the oldest aU peaks.

Evidence from $^{230}\mathrm{Th}_{xs}$ that the observed aU peaks represent post depositional dissolution supports our conclusion that aU peaks in 17PC as displayed in Figures 4.2 and 4.3 are in situ and not the result of post depositional reprecipitation of aU down core. Not only are these peaks most likely original to the sediment intervals in which they are found, the available evidence supports the conclusion that they were initially larger than presently observed.

4.6.2 Utility of derived mass fluxes

As described above, the consequence of ^{230}Th abandonment by ^{238}U is that $^{230}\mathrm{Th}_{xs}$ values are elevated relative to the actual delivery of ^{230}Th from the water column. Accordingly, $^{230}\mathrm{Th}_{xs,0}$ values are also elevated. When mass fluxes are calculated from these $^{230}\mathrm{Th}_{xs,0}$ values:

$$\text{Mass Flux} = (\beta * \text{z})/(^{230}\mathrm{Th}_{xs,0})$$

the result is that the calculated mass flux is too low. This is illustrated in Figure 4.7. Unfortunately, this means that while the record from 17PC is very useful in the context of

reconstructing intervals of reduced bottom water oxygen in the Pacific, ^{230}Th-derived ^{232}Th fluxes are less reliable for reconstructing dust fluxes over this interval.

4.7 Acknowledgements

We thank the sediment core repository at LDEO for providing samples, Marty Fleisher for technical assistance in the lab, and Gemma Sahwell for her help preparing sediments for analysis. This research was funded in part by awards from the Geological Society of America (A.W.J.) and US National Science Foundation AGS-1502889 (J.F.M. and G.W.), and benefited from previous support from NSF OCE-1003374, OCE-1159053 and OCE-1158886, and the Comer Science and Education Foundation.

Part III

Bibliography

Bibliography

Adler, R. F. et al. (2015). "The Version-2 Global Precipitation Climatology Project (GPCP) Monthly Precipitation Analysis (1979–Present)". In: *Journal of Hydrometeorology* 4.6, pp. 1147–1167.

Alley, R. B. (2000). "The Younger Dryas cold interval as viewed from central Greenland". In: *Quaternary Science Reviews* 19.1-5, pp. 213–226.

Andersen, M. B. et al. (2010). "Precise determination of the open ocean $^{234}U/^{238}U$ composition". In: *Geochemistry Geophysics Geosystems* 11.12, 10.1029/2010GC003318.

Anderson, R. F. (1982). "Concentration, vertical flux, and remineralization of particulate uranium in seawater". In: *Geochimica et Cosmochimica Acta* 46.7, pp. 1293–1299.

Anderson, R. F. et al. (1989). "Uranium deposition in saanich inlet sediments, vancouver island". In: *Geochimica et Cosmochimica Acta* 53.9, pp. 2205–2213.

Anderson, R. F. et al. (2006). "Glacial–interglacial variability in the delivery of dust to the central equatorial Pacific Ocean". In: *Earth and Planetary Science Letters* 242.3–4, pp. 406–414.

Anderson, R. F. et al. (2008). "Modern $CaCO_3$ preservation in equatorial Pacific sediments in the context of late-Pleistocene glacial cycles". In: *Marine Chemistry* 111.1, pp. 30–46.

Anderson, R. F. et al. (2009). "Wind-Driven Upwelling in the Southern Ocean and the Deglacial Rise in Atmospheric CO_2". In: *Science* 323.5920, pp. 1443–1448.

Anderson, R. F. et al. (2014). "Biological response to millennial variability of dust and nutrient supply in the Subantarctic South Atlantic Ocean". In: *Philos Transact A Math Phys Eng Sci* 372.2019, DOI: 10.1098/rsta.2013.0054.

Arbuszewski, J. A. et al. (2013). "Meridional shifts of the Atlantic intertropical convergence zone since the Last Glacial Maximum". In: *Nature Geoscience* 6.11, pp. 959–962.

Bacon, M. P. (1984). "Glacial to interglacial changes in carbonate and clay sedimentation in the Atlantic Ocean estimated from ^{230}Th measurements". In: *Chemical Geology* 46.2, pp. 97–111.

Bacon, M. P. and R. F. Anderson (1982). "Distribution of thorium isotopes between dissolved and particulate forms in the deep sea". In: *Journal of Geophysical Research* 87.C3, pp. 2045–2056.

Barker, S. et al. (2015). "Icebergs not the trigger for North Atlantic cold events". In: *Nature* 520.7547, pp. 333–336.

Boehnke, P. and T. M. Harrison (2014). "A meta-analysis of geochronologically relevant half-lives: what's the best decay constant?" In: *International Geology Review* 56.7, pp. 905–914.

Böhm, E. et al. (2014). "Strong and deep Atlantic meridional overturning circulation during the last glacial cycle". In: *Nature* 517.7532, pp. 73–76.

Boudreau, B. P. (1994). "Is burial velocity a master parameter for bioturbation?" In: *Geochimica et Cosmochimica Acta* 58.4, pp. 1243–1249.

Boyle, E. A. (1988a). "The role of vertical chemical fractionation in controlling late Quaternary atmospheric carbon dioxide". In: *Journal of Geophysical Research: Oceans* 93.C12, pp. 15701–15714.

— (1988b). "Vertical oceanic nutrient fractionation and glacial/interglacial CO_2 cycles". In: *Nature* 331.6151, pp. 55–56.

— (1992). "Cadmium and δ^{13}C Paleochemical Ocean Distributions During the Stage 2 Glacial Maximum". In: *Annual Review of Earth and Planetary Sciences* 20.1, pp. 245–287.

Bradtmiller, L. I. et al. (2010). "A deeper respired carbon pool in the glacial equatorial Pacific Ocean". In: *Earth and Planetary Science Letters* 299.3–4, pp. 417–425.

Broecker, W. S. (1982). "Glacial to interglacial changes in ocean chemistry". In: *Progress in Oceanography* 11.2, pp. 151–197.

Broecker, W. S. and E. Clark (2010). "Search for a glacial-age ^{14}C-depleted ocean reservoir". In: *Geophysical Research Letters* 37.13, DOI: 10.1029/2010GL043969.

Broecker, W. S. et al. (2004). "Ventilation of the Glacial Deep Pacific Ocean". In: *Science* 306.5699, pp. 1169–1172.

Broecker, W. S. et al. (2008). "Near constancy of the Pacific Ocean surface to mid-depth radiocarbon-age difference over the last 20 kyr". In: *Earth and Planetary Science Letters* 274.3–4, pp. 322–326.

Capron, E. et al. (2012). "A global picture of the first abrupt climatic event occurring during the last glacial inception". In: *Geophysical Research Letters* 39.15.

Ceppi, P. et al. (2013). "The relationship between the ITCZ and the Southern Hemispheric eddy-driven jet". In: *Journal of Geophysical Research: Atmospheres* 118.11, pp. 5136–5146.

Cheng, H. et al. (2009). "Ice Age Terminations". In: *Science* 326.5950, pp. 248–252.

Cheng, H. et al. (2013). "Improvements in ^{230}Th dating, ^{230}Th and ^{234}U half-life values, and U–Th isotopic measurements by multi-collector inductively coupled plasma mass spectrometry". In: *Earth and Planetary Science Letters* 371–372, pp. 82–91.

Chiang, J. C. H. and C. M. Bitz (2005). "Influence of high latitude ice cover on the marine Intertropical Convergence Zone". In: *Climate Dynamics* 25.5, pp. 477–496.

Chiang, J. C. H. and A. R. Friedman (2012). "Extratropical Cooling, Interhemispheric Thermal Gradients, and Tropical Climate Change". In: *Annual Review of Earth and Planetary Sciences* 40.1, pp. 383–412.

Chiang, J. C. H. et al. (2003). "Sensitivity of the Atlantic Intertropical Convergence Zone to Last Glacial Maximum boundary conditions". In: *Paleoceanography* 18.4.

Claussen, M. (2009). "Late Quaternary vegetation-climate feedbacks". In: *Climate of the Past* 5.2, pp. 203–216.

Cochran, J. K. et al. (1986). "The geochemistry of uranium and thorium in coastal marine sediments and sediment pore waters". In: *Geochimica et Cosmochimica Acta* 50.5, pp. 663–680.

Colley, S. et al. (1989). "Uranium relocations and derivation of quasi-isochrons for a turbidite/pelagic sequence in the Northeast Atlantic". In: *Quaternary Science Reviews* 53.6, pp. 1223–1234.

Costa, K. M. et al. (2016). "No iron fertilization in the equatorial Pacific Ocean during the last ice age". In: *Nature* 529.7587, pp. 519–522.

Costa, K. M. et al. (2017). "Productivity patterns in the equatorial Pacific over the last 30,000 years". In: *Global Biogeochemical Cycles* 122.2.

Donohoe, A. et al. (2013). "The Relationship between ITCZ Location and Cross-Equatorial Atmospheric Heat Transport: From the Seasonal Cycle to the Last Glacial Maximum". In: *Journal of Climate* 26.11, pp. 3597–3618.

Dubois, N. and M. Kienast (2011). "Spatial reorganization in the equatorial divergence in the Eastern Tropical Pacific during the last 150 kyr". In: *Geophysical Research Letters* 38.16, DOI: 10.1029/2011GL048325.

Dykoski, C. et al. (2005). "A high-resolution, absolute-dated Holocene and deglacial Asian monsoon record from Dongge Cave, China". In: *Earth and Planetary Science Letters* 233.1-2, pp. 71–86.

Finneran, K. T. et al. (2002). "Potential for Bioremediation of Uranium-Contaminated Aquifers with Microbial U(VI) Reduction". In: *Soil and Sediment Contamination: An International Journal* 11.3, pp. 339–357.

Fleisher, M. Q. and R. F. Anderson (2003). "Assessing the collection efficiency of Ross Sea sediment traps using ^{230}Th and ^{231}Pa". In: *Deep Sea Research Part II: Topical Studies in Oceanography* 50.3-4, pp. 693–712.

Francois, R. et al. (2004). "^{230}Th normalization: An essential tool for interpreting sedimentary fluxes during the late Quaternary". In: *Paleoceanography* 19.1.

Galbraith, E. D. et al. (2007). "Carbon dioxide release from the North Pacific abyss during the last deglaciation". In: *Nature* 449.7164, pp. 890–893.

Goreau, T. J. (1980). "Frequency sensitivity of the deep-sea climatic record". In: *Nature* 287.5783, pp. 620–622.

Gottschalk, J. et al. (2016). "Biological and physical controls in the Southern Ocean on past millennial-scale atmospheric CO_2 changes". In: *Nature Communications* 7, p. 11539.

Hall, I. R. et al. (2001). "Intensified deep Pacific inflow and ventilation in Pleistocene glacial times". In: *Nature* 412.6849, pp. 809–812.

Haslett, J. and A. Parnell (2008). "A simple monotone process with application to radiocarbon-dated depth chronologies". In: *Journal of the Royal Statistical Society: Series C (Applied Statistics)* 57.4, pp. 399–418.

Haug, G. H. et al. (2001). "Southward migration of the Intertropical Convergence Zone through the Holocene". In: *Science* 293.1304, pp. 1304–1308.

Henderson, G. M. and R. F. Anderson (2003). "The U-series Toolbox for Paleoceanography". In: *Reviews in mineralogy and geochemistry* 52.1, pp. 493–531.

Herguera, J. C. et al. (1992). "Evidence for a bathyal front at 2000-M depth in the glacial Pacific, based on a depth transect on Ontong Java Plateau". In: *Paleoceanography* 7.3, pp. 273–288.

Herguera, J. C. et al. (2010). "Intermediate and deep water mass distribution in the Pacific during the Last Glacial Maximum inferred from oxygen and carbon stable isotopes". In: *Quaternary Science Reviews* 29.9–10, pp. 1228–1245.

Hodell, D. A. et al. (2005). "Terminal Classic drought in the northern Maya lowlands inferred from multiple sediment cores in Lake Chichancanab (Mexico)". In: *Quaternary Science Reviews* 24.12–13, pp. 1413–1427.

Hoffman, J. S. et al. (2015). "Estimating age model uncertainties for the last interglaciation". In: *Fall Meeting, American Geophysical Union*. San Francisco.

Hoogakker, B. A. A. et al. (2015a). "Millennial changes in North Atlantic oxygen concentrations". In: *Biogeosciences Discussions* 12.15, pp. 12947–12973.

Hoogakker, B. A. A. et al. (2015b). "Glacial-interglacial changes in bottom-water oxygen content on the Portuguese margin". In: *Nature Geoscience* 8.1, pp. 40–43.

Husar, R. B. et al. (1997). "Characterization of tropospheric aerosols over the oceans with the NOAA advanced very high resolution radiometer optical thickness operational product". In: *Journal of Geophysical Research: Atmospheres* 102.D14, pp. 16889–16909.

Jaccard, S. L. and E. D. Galbraith (2012). "Large climate-driven changes of oceanic oxygen concentrations during the last deglaciation". In: *Nature Geoscience* 5.2, pp. 151–156.

Jaccard, S. L. et al. (2009). "Subarctic Pacific evidence for a glacial deepening of the oceanic respired carbon pool". In: *Earth and Planetary Science Letters* 277.1-2, pp. 156–165.

Jaccard, S. L. et al. (2010). "A pervasive link between Antarctic ice core and subarctic Pacific sediment records over the past 800 kyrs". In: *Climate of the Last Million Years: New Insights from EPICA and Other Records* 29.1–2, pp. 206–212.

Jaccard, S. L. et al. (2014). "Ocean (De)oxygenation Across the Last Deglaciation: Insights for the Future". In: *Oceanography* 27.1, pp. 26–35.

Jaccard, S. L. et al. (2016). "Covariation of deep Southern Ocean oxygenation and atmospheric CO_2 through the last ice age". In: *Nature* 530.7589, pp. 207–210.

Jacobel, A. W. et al. (2016). "Large deglacial shifts of the Pacific Intertropical Convergence Zone". In: *Nature Communications* 7, DOI: 10.1038/ncomms10449.

— (2017). "Climate-related response of dust flux to the central equatorial Pacific over the past 150 kyr". In: *Earth and Planetary Science Letters* 457, pp. 160–172.

Jaffey, A. H. et al. (1971). "Precision Measurement of Half-Lives and Specific Activities of ^{235}U and ^{238}U ". In: *Physical Review C* 4.5, pp. 1889–1906.

Jouzel, J. et al. (2007). "Orbital and Millennial Antarctic Climate Variability over the Past 800,000 Years". In: *Science* 317.5839, pp. 793–796.

Keigwin, L. (1998). "Glacial-age hydrography of the far northwest Pacific Ocean". In: *Paleoceanography* 13.4, pp. 323–339.

Keigwin, L. and S. J. Lehman (2015). "Radiocarbon evidence for a possible abyssal front near 3.1 km in the glacial equatorial Pacific Ocean". In: *Earth and Planetary Science Letters* 425, pp. 93–104.

Key, R. M. et al. (2004). "A global ocean carbon climatology: Results from Global Data Analysis Project (GLODAP)". In: *Global Biogeochemical Cycles* 18.4.

Kienast, S. S. et al. (2006). "Testing the silica leakage hypothesis with sedimentary opal records from the eastern equatorial Pacific over the last 150 kyrs". In: *Geophysical Research Letters* 33.15, DOI: 10.1029/2006GL026651.

Kienast, S. S. et al. (2007). "Thorium-230 normalized particle flux and sediment focusing in the Panama Basin region during the last 30,000 years". In: *Paleoceanography* 22.2.

Kienast, S. S. et al. (2013). "Near collapse of the meridional SST gradient in the eastern equatorial Pacific during Heinrich Stadial 1". In: *Paleoceanography* 28.4.

Klinkhammer, G. P. and M. R. Palmer (1991). "Uranium in the oceans: Where it goes and why". In: *Earth and Planetary Science Letters* 55.7, pp. 1799–1806.

Korff, L. et al. (2016). "Cyclic magnetite dissolution in Pleistocene sediments of the abyssal northwest Pacific Ocean: Evidence for glacial oxygen depletion and carbon trapping". In: *Paleoceanography* 31, pp. 600–624.

Koutavas, A. and J. Lynch-Stieglitz (2004). "Variability of the Marine ITCZ over the Eastern Pacific during the Past 30,000 Years". In: *The Hadley Circulation: Present, Past and Future*. Ed. by H. F. Diaz and R. S. Bradley. Dordrecht: Springer Netherlands, pp. 347–369.

Kraus, K. A. et al. (1956). "Anion-exchange Studies. XXI. Th(IV) and U(IV) in Hydrochloric Acid. Separation of Thorium, Protactinium and Uranium1,2". In: *J. Am. Chem. Soc.* 78.12, pp. 2692–2695.

Lambert, F. et al. (2008). "Dust-climate couplings over the past 800,000 years from the EPICA Dome C ice core". In: *Nature* 452.7187, pp. 616–619.

Lambert, F. et al. (2012). "Centennial mineral dust variability in high-resolution ice core data from Dome C, Antarctica". In: *Climate of the Past* 8.2, pp. 609–623.

Landais, A. et al. (2015). "A review of the bipolar see–saw from synchronized and high resolution ice core water stable isotope records from Greenland and East Antarctica". In: *Quaternary Science Reviews* 114, pp. 18–32.

Langmuir, D. (1978). "Uranium solution-mineral equilibria at low temperatures with applications to sedimentary ore deposits". In: *Geochimica et Cosmochimica Acta* 42.6, pp. 547–569.

Larrasoana, J. C. et al. (2003). "Three million years of monsoon variability over the northern Sahara". In: *Climate Dynamics* 21.7-8, pp. 689–698.

Lea, D. W. et al. (2006). "Paleoclimate history of Galápagos surface waters over the last 135,000 yr". In: *Climate of the Last Million Years: New Insights from EPICA and Other Records* 25.11–12, pp. 1152–1167.

Leduc, G. et al. (2007). "Moisture transport across Central America as a positive feedback on abrupt climatic changes". In: *Nature* 445.7130, pp. 908–911.

Lee, S.-Y. et al. (2011). "Southern Ocean wind response to North Atlantic cooling and the rise in atmospheric CO_2: Modeling perspective and paleoceanographic implications". In: *Paleoceanography* 26.1, DOI: 10.1029/2010PA002004.

Lehman, S. J. et al. (2002). "Relation of subtropical Atlantic temperature, high-latitude ice rafting, deep water formation, and European climate 130,000–60,000 years ago". In: *Quaternary Science Reviews* 21.18–19, pp. 1917–1924.

Lisiecki, L. E. and M. E. Raymo (2005). "A Pliocene-Pleistocene stack of 57 globally distributed benthic δ^{18}O records". In: *Paleoceanography* 20.1, DOI: 10.1029/2004PA001071.

Liu, Y. et al. (2015). "Obliquity pacing of the western Pacific Intertropical Convergence Zone over the past 282,000 years". In: *Nature Communications* 6, p. 10018.

Loubere, P. (2000). "Marine control of biological production in the eastern equatorial Pacific Ocean". In: *Nature* 406.6795, pp. 497–500.

Lüthi, D. et al. (2008). "High-resolution carbon dioxide concentration record 650,000-800,000 years before present". In: *Nature* 453.7193, pp. 379–382.

Lyle, M. W. et al. (2014). "Sediment size fractionation and focusing in the equatorial Pacific: Effect on ^{230}Th normalization and paleoflux measurements". In: *Paleoceanography* 29.7, pp. 747–763.

Lyle, M. W. et al. (2016). "Dynamic carbonate sedimentation on the Northern Line Islands Ridge, Palmyra Basin". In: *Marine Geology* 379, pp. 194–207.

Lynch-Stieglitz, J. et al. (2015). "Glacial-interglacial changes in central tropical Pacific surface seawater property gradients". In: *Paleoceanography* 30.5, pp. 423–438.

Mahowald, N. M. et al. (2006). "Climate response and radiative forcing from mineral aerosols during the last glacial maximum, pre-industrial, current and doubled-carbon dioxide climates". In: *Geophysical Research Letters* 33.20, DOI: 10.1029/2006GL026126.

Mahowald, N. M. et al. (2014). "The size distribution of desert dust aerosols and its impact on the Earth system". In: *Aeolian Research* 15.C, pp. 53–71.

Marino, G. et al. (2015). "Bipolar seesaw control on last interglacial sea level". In: *Nature* 522.7555, pp. 197–201.

Markle, B. R. et al. (2016). "A coherent understanding of water-isotope and ice-impurity variability in Antarctica at millennial to orbital time scales". In: *Fall Meeting, American Geophysical Union*. San Francisco.

Martínez-Garcia, A. et al. (2009). "Links between iron supply, marine productivity, sea surface temperature, and CO_2 over the last 1.1 Ma". In: *Paleoceanography* 24.1, DOI: 10.1029/2008PA001657.

Martínez-Garcia, A. et al. (2014). "Iron Fertilization of the Subantarctic Ocean During the Last Ice Age". In: *Science* 343.6177, pp. 1347–1350.

Masson-Delmotte, V. et al. (2010). "EPICA Dome C record of glacial and interglacial intensities". In: *Climate of the Last Million Years: New Insights from EPICA and Other Records* 29.1–2, pp. 113–128.

Matsumoto, K. et al. (2002). "Interior hydrography and circulation of the glacial Pacific Ocean". In: *Quaternary Science Reviews* 21.14–15, pp. 1693–1704.

McGee, D. et al. (2007). "Deglacial changes in dust flux in the eastern equatorial Pacific". In: *Earth and Planetary Science Letters* 257.1–2, pp. 215–230.

McGee, D. et al. (2010). "Gustiness: The driver of glacial dustiness?" In: *Quaternary Science Reviews* 29.17–18, pp. 2340–2350.

McGee, D. et al. (2014). "Changes in ITCZ location and cross-equatorial heat transport at the Last Glacial Maximum, Heinrich Stadial 1, and the mid-Holocene". In: *Earth and Planetary Science Letters* 390.C, pp. 69–79.

McGee, D. et al. (2016). "Tracking eolian dust with helium and thorium: Impacts of grain size and provenance". In: *Geochimica et Cosmochimica Acta* 175, pp. 47–67.

McManus, J. et al. (2005). "Authigenic uranium: Relationship to oxygen penetration depth and organic carbon rain". In: *Geochimica et Cosmochimica Acta* 69.1, pp. 95–108.

McManus, J. F. et al. (1998). "Radiometrically determined sedimentary fluxes in the subpolar Atlantic during the last 140,000 years". In: *Earth and Planetary Science Letters* 155, pp. 29–43.

McManus, J. F. et al. (1999). "A 0.5-million-year record of millennial-scale climate variability in the North Atlantic". In: *Science* 283.5404, pp. 971–975.

McManus, J. et al. (1994). "High-resolution climate records from the North Atlantic during the last interglacial". In: *Nature* 371.6495, pp. 326–329.

Medina-Elizalde, M. and E. J. Rohling (2012). "Collapse of Classic Maya Civilization Related to Modest Reduction in Precipitation". In: *Science* 335.6071, pp. 956–959.

Mekik, F. A. et al. (2012). "The mystery of the missing deglacial carbonate preservation maximum". In: *Quaternary Science Reviews* 39, pp. 60–72.

Members, E. C. (2004). "Eight glacial cycles from an Antarctic ice core". In: *Nature* 429.6992, pp. 623–628.

Mills, R. A. et al. (2010). "Hydrothermal sediments record changes in deep water oxygen content in the SE Pacific". In: *Paleoceanography* 25.4, DOI: 10.1029/2010PA001959.

Mokeddem, Z. et al. (2014). "Oceanographic dynamics and the end of the last interglacial in the subpolar North Atlantic". In: *Proceedings of the National Academy of Sciences* 111.31, pp. 11263–11268.

Morford, J. L. et al. (2005). "Diagenesis of oxyanions (V, U, Re, and Mo) in pore waters and sediments from a continental margin". In: *Geochimica et Cosmochimica Acta* 69.21, pp. 5021–5032.

North Greenland Ice Core Project members (2004). "High-resolution record of Northern Hemisphere climate extending into the last interglacial period". In: *Nature* 431.7005, pp. 147–151.

Oppo, D. W. et al. (2006). "Evolution and demise of the Last Interglacial warmth in the subpolar North Atlantic". In: *Quaternary Science Reviews* 25.23-24, pp. 3268–3277.

Owens, S. A. et al. (2011). "Re-evaluating the 238U-salinity relationship in seawater: Implications for the 238U–234Th disequilibrium method". In: *Marine Chemistry* 127.1–4, pp. 31–39.

Pailler, D. and E. Bard (2002). "High frequency palaeoceanographic changes during the past 140,000 yr recorded by the organic matter in sediments of the Iberian Margin". In: *Palaeogeography, Palaeoclimatology, Palaeoecology* 181, pp. 431–452.

Parrenin, F. et al. (2007). "The EDC3 chronology for the EPICA Dome C ice core". In: *Climate of the Past* 3.3, pp. 485–497.

Pausata, F. S. R. et al. (2011). "Chinese stalagmite [delta]18O controlled by changes in the Indian monsoon during a simulated Heinrich event". In: 4.7, pp. 474–480.

Petit, J. R. et al. (1999). "Climate and atmospheric history of the past 420,000 years from the Vostok ice core, Antarctica". In: *Nature* 399, pp. 429–436.

Pichat, S. et al. (2004). "Lower export production during glacial periods in the equatorial Pacific derived from $(^{231}\mathrm{Pa}/^{230}\mathrm{Th})_{xs,0}$ measurements in deep-sea sediments". In: *Paleoceanography* 19.4, DOI: 10.1029/2003pa000994.

Pichat, S. et al. (2014). "Lead isotopes in the Eastern Equatorial Pacific record Quaternary migration of the South Westerlies". In: *Earth and Planetary Science Letters* 388, pp. 293–305.

Porter, S. C. and A. Zhisheng (1995). "Correlation between climate events in the North Atlantic and China during the last glaciation". In: *Nature* 375.6529, pp. 305–308.

Rafter, P. A. et al. (2012). "Subsurface tropical Pacific nitrogen isotopic composition of nitrate: Biogeochemical signals and their transport". In: *Global Biogeochemical Cycles* 26.1, DOI: 10.1029/2010GB003979.

Rasmussen, S. O. et al. (2014). "A stratigraphic framework for abrupt climatic changes during the Last Glacial period based on three synchronized Greenland ice-core records: refining and extending the INTIMATE event stratigraphy". In: *Quaternary Science Reviews* 106, pp. 14–28.

Rasmussen, T. L. et al. (2003). "Deep sea records from the southeast Labrador Sea: Ocean circulation changes and ice-rafting events during the last 160,000 years". In: *Paleoceanography* 18.1, DOI: 10.1029/2001PA000736.

Rea, D. K. (1994). "The paleoclimatic record provided by eolian deposition in the deep sea: the geologic history of wind". In: *Reviews of Geophysics* 32, pp. 159–195.

Rea, D. K. and S. A. Hovan (1995). "Grain size distribution and depositional processes of the mineral component of abyssal sediments: Lessons from the North Pacific". In: *Paleoceanography* 10.2, pp. 251–258.

Reimer, P. J. et al. (2013). "IntCal13 and Marine13 Radiocarbon Age Calibration Curves 0-50,000 Years cal BP". In: *Radiocarbon* 55.4, pp. 1869–1887.

Reimi, M. A. and F. Marcantonio (2016). "Constraints on the magnitude of the deglacial migration of the ITCZ in the Central Equatorial Pacific Ocean". In: *Earth and Planetary Science Letters* 453.C, pp. 1–8.

Ren, H. et al. (2015). "Glacial-to-interglacial changes in nitrate supply and consumption in the subarctic North Pacific from microfossil-bound N isotopes at two trophic levels". In: *Paleoceanography* 30.9, pp. 1217–1232.

Ridley, H. E. et al. (2015). "Aerosol forcing of the position of the intertropical convergence zone since ad 1550". In: 8.3, pp. 195–200.

Roe, G. (2009). "On the interpretation of Chinese loess as a paleoclimate indicator". In: *Quaternary Research* 71.2, pp. 150–161.

Ronge, T. A. et al. (2016). "Radiocarbon constraints on the extent and evolution of the South Pacific glacial carbon pool". In: *Nature Communications* 7.

Ruddiman, W. F. and L. K. Glover (1972). "Vertical Mixing of Ice-Rafted Volcanic Ash in North Atlantic Sediments". In: *Geological Society of America Bulletin* 83.9, pp. 2817–2836.

Russell, A. D. et al. (2004). "Effects of seawater carbonate ion concentration and temperature on shell U, Mg, and Sr in cultured planktonic foraminifera". In: *Geochimica et Cosmochimica Acta* 68.21, pp. 4347–4361.

Ruth, U. et al. (2007). "Ice core evidence for a very tight link between North Atlantic and east Asian glacial climate". In: *Geophysical Research Letters* 34.3, p. L03706.

Sarnthein, M. et al. (2013). "Peak glacial ^{14}C ventilation ages suggest major draw-down of carbon into the abyssal ocean". In: *Climate of the Past* 9.6, pp. 2595–2614.

Schlanger, S. O. et al. (1984). "Geology and Geochronology of the Line Islands". In: *Journal of Geophysical Research: Oceans* 89.B13, pp. 11261–11272.

Schlosser, C. et al. (2014). "Seasonal ITCZ migration dynamically controls the location of the (sub)tropical Atlantic biogeochemical divide". In: *Proceedings of the National Academy of Sciences* 111.4, pp. 1438–1442.

Schneider, T. et al. (2014). "Migrations and dynamics of the intertropical convergence zone". In: *Nature* 513.7516, pp. 45–53.

Seager, R. et al. (2005). "Modeling of Tropical Forcing of Persistent Droughts and Pluvials over Western North America: 1856-2000*". In: *Journal of Climate* 18.19, pp. 4065–4088.

Seierstad, I. K. et al. (2014). "Consistently dated records from the Greenland GRIP, GISP2 and NGRIP ice cores for the past 104 ka reveal regional millennial-scale δ^{18}O gradients with possible Heinrich event imprint". In: *Climate of the Last Million Years: New Insights from EPICA and Other Records* 106, pp. 29–46.

Serno, S. et al. (2015). "Comparing dust flux records from the Subarctic North Pacific and Greenland: Implications for atmospheric transport to Greenland and for the application of dust as a chronostratigraphic tool". In: *Paleoceanography* 30.6, pp. 583–600.

Serno, S. et al. (2017). "Change in dust seasonality as the primary driver for orbital-scale dust storm variability in East Asia". In: *Geophysical Research Letters*.

Shaw, T. J. et al. (1994). "Redox dynamics in the Chesapeake Bay: The effect on sediment/water uranium exchange". In: *Geochimica et Cosmochimica Acta* 58.14, pp. 2985–2995.

Sigman, D. M. and E. A. Boyle (2000). "Glacial/interglacial variations in atmospheric carbon dioxide". In: *Nature* 407.6806, pp. 859–869.

Sigman, D. M. et al. (2010). "The polar ocean and glacial cycles in atmospheric CO_2 concentration". In: *Nature* 466.7302, pp. 47–55.

Smith, C. R. et al. (1997). "Latitudinal variations in benthic processes in the abyssal equatorial Pacific: control by biogenic particle flux". In: *Deep-Sea Research Part II* 44.9, pp. 2295–2317.

Sprenk, D. et al. (2013). "Southern Ocean bioproductivity during the last glacial cycle - new detection method and decadal-scale insight from the Scotia Sea". In: *Geological Society, London, Special Publications* 381.1, pp. 245–261.

Stager, J. C. et al. (2011). "Catastrophic Drought in the Afro-Asian Monsoon Region During Heinrich Event 1". In: *Science* 331.6022, pp. 1299–1302.

Studer, A. S. et al. (2015). "Antarctic Zone nutrient conditions during the last two glacial cycles". In: *Paleoceanography* 30.7, pp. 845–862.

Stuut, J.-B. W. et al. (2002). "A 300-kyr record of aridity and wind strength in southwestern Africa: inferences from grain-size distributions of sediments on Walvis Ridge, SE Atlantic". In: *Marine Geology* 180.1–4, pp. 221–233.

Suman, D. O. and M. P. Bacon (1989). "Variations in Holocene sedimentation in the North American Basin determined from ^{230}Th measurements". In: *Deep Sea Research Part A. Oceanographic Research Papers* 36.6, pp. 869–878.

Teal, L. R. et al. (2008). "Global patterns of bioturbation intensity and mixed depth of marine soft sediments". In: *Aquatic Biology* 2.3, pp. 207–218.

Toggweiler, J. et al. (1991). "The Peru upwelling and the ventilation of the south Pacific thermocline". In: *Journal of Geophysical Research* 96.C11, pp. 20467–20497.

Veres, D. et al. (2013). "The Antarctic ice core chronology (AICC2012): an optimized multi-parameter and multi-site dating approach for the last 120 thousand years". In: *Climate of the Past* 9, pp. 1733–1748.

Wang, H. and V. M. Mehta (2008). "Decadal variability of the Indo-Pacific warm pool and its association with atmospheric and oceanic variability in the NCEP-NCAR and SODA reanalyses". In: *Journal of Climate*, pp. 5545–5565.

Wang, X. et al. (2004). "Wet periods in northeastern Brazil over the past 210 kyr linked to distant climate anomalies". In: *Nature* 432.7018, pp. 740–743.

Wang, X. et al. (2007). "Millennial-scale precipitation changes in southern Brazil over the past 90,000 years". In: *Geophysical Research Letters* 34.23, DOI: 10.1029/2007GL031149.

Wang, Y. J. et al. (2001). "A High-Resolution Absolute-Dated Late Pleistocene Monsoon Record from Hulu Cave, China". In: *Science* 294, pp. 2345–2348.

Wang, Y. et al. (2005). "The Holocene Asian Monsoon: Links to Solar Changes and North Atlantic Climate". In: *Science* 308.5723, pp. 854–857.

Winckler, G. et al. (2005). "Equatorial Pacific productivity and dust flux during the mid-Pleistocene climate transition". In: *Paleoceanography* 20.4, DOI: 10.1029/2005PA001177.

Winckler, G. et al. (2008). "Covariant Glacial-Interglacial Dust Fluxes in the Equatorial Pacific and Antarctica". In: *Science* 320.5872, pp. 93–96.

Winckler, G. et al. (2016). "Ocean dynamics, not dust, have controlled equatorial Pacific productivity over the past 500,000 years". In: *Proceedings of the National Academy of Sciences* 113.22, pp. 6119–6124.

Xiao, J. L. et al. (1999). "East Asian monsoon variation during the last 130,000 Years: evidence from the Loess Plateau of central China and Lake Biwa of Japan". In: *Quaternary Science Reviews* 18.1, pp. 147–157.

Xie, R. C. and F. Marcantonio (2012). "Deglacial dust provenance changes in the Eastern Equatorial Pacific and implications for ITCZ movement". In: *Earth and Planetary Science Letters* 317-318.C, pp. 386–395.

Yancheva, G. et al. (2007). "Influence of the intertropical convergence zone on the East Asian monsoon". In: *Nature* 445.7123, pp. 74–77.

Yang, Y.-L. et al. (1995). "Geochemical record of the Panama basin during the last glacial maximum carbon event shows that the glacial ocean was not suboxic". In: *Geology* 23.12, pp. 1115–1118.

Yarincik, K. M. et al. (2000). "Climatically sensitive eolian and hemipelagic deposition in the Cariaco Basin, Venezuela, over the past 578,000 years: Results from Al/Ti and K/Al". In: *Paleoceanography* 15.2, pp. 210–228.

Yu, J. et al. (2014). "Deep South Atlantic carbonate chemistry and increased interocean deep water exchange during last deglaciation". In: *Quaternary Science Reviews* 90, pp. 80–89.

Zheng, Y. et al. (2002a). "Remobilization of authigenic uranium in marine sediments by bioturbation". In: *Geochimica et Cosmochimica Acta* 66.10, pp. 1759–1772.

Zheng, Y. et al. (2002b). "Preservation of particulate non-lithogenic uranium in marine sediments". In: *Geochimica et Cosmochimica Acta* 66.17, pp. 3085–3092.

Part IV

Appendices

Appendix A

ML1208-37BB Sediment Core Data

Table A.1: Data from ML1208-37BB retrieved from 2,798 m of water at (7.04°N, -161.63°W).

Depth	Age	$^{230}Th_{xs,0}$	Mass Flux	^{232}Th	^{232}Th Flux	Dust Flux	aU
(cm)	(ka)	(dpm g^{-1})	(g cm^{-2} kyr^{-1})	(dpm g^{-1})	(μg cm^{-2} kyr^{-1})	(g m^{-2} yr^{-1})	(ppm)
0	6.49	8.468	0.846	0.03	0.106	0.099	0.12
1	7.16	8.72	0.821	0.027	0.092	0.086	0.12
2	7.52	8.561	0.837	0.026	0.09	0.084	0.12
3	7.85	8.638	0.829	0.027	0.093	0.087	0.12
4	8.16	8.276	0.866	0.026	0.093	0.087	0.12
5	8.47	8.695	0.824	0.028	0.094	0.088	0.13
6	8.77	7.937	0.903	0.027	0.099	0.093	0.12
7	9.07	8.22	0.871	0.029	0.105	0.098	0.12
8	9.37	8.872	0.807	0.032	0.108	0.101	0.13
9	9.68	8.583	0.835	0.032	0.111	0.104	0.12
10	10.00	8.278	0.865	0.034	0.12	0.112	0.12
11	10.36	8.487	0.844	0.036	0.126	0.118	0.12
12	10.96	7.989	0.897	0.042	0.155	0.145	0.11
13	11.67	8.24	0.869	0.044	0.159	0.148	0.11
14	12.19	7.938	0.902	0.045	0.169	0.158	0.1
15	12.64	9.306	0.77	0.053	0.167	0.156	0.12
16	13.08	7.901	0.907	0.051	0.191	0.179	0.1
17	13.51	7.013	1.021	0.05	0.21	0.196	0.09
18	13.97	9.204	0.778	0.073	0.235	0.22	0.11
19	14.47	8.249	0.868	0.068	0.244	0.228	0.1
20	15.23	6.96	1.029	0.064	0.271	0.253	0.08
21	16.01	7.064	1.014	0.073	0.307	0.287	0.07
22	16.56	6.662	1.075	0.071	0.313	0.292	0.06
23	17.11	6.789	1.055	0.071	0.31	0.29	0.06
24	18.01	7.14	1.003	0.075	0.309	0.289	0.06
25	19.29	8.33	0.86	0.088	0.313	0.292	0.07
26	20.17	7.643	0.937	0.079	0.305	0.285	0.07
30	23.15	7.257	0.987	0.076	0.308	0.288	0.06
34	26.16	6.744	1.062	0.072	0.316	0.295	0.07
38	30.19	6.499	1.102	0.061	0.279	0.26	0.08
42	32.58	6.579	1.089	0.059	0.265	0.248	0.09
46	34.86	7.671	0.934	0.068	0.26	0.243	0.09
50	37.29	5.641	1.27	0.049	0.255	0.238	0.09
54	40.98	6.549	1.094	0.052	0.237	0.221	0.1
58	43.46	5.565	1.287	0.044	0.235	0.22	0.08
62	45.84	6.285	1.14	0.052	0.242	0.226	0.1
66	48.24	6.331	1.131	0.049	0.227	0.212	0.12
69.5	50.49	5.945	1.205	0.049	0.245	0.229	0.1
70	50.97	5.589	1.282	0.052	0.274	0.256	0.1
71	52.42	6.48	1.105	0.047	0.213	0.199	0.08
73.5	54.48	5.523	1.297	0.055	0.293	0.274	0.09
74	54.84	6.302	1.137	0.067	0.315	0.295	0.09
74	54.84	6.047	1.185	0.061	0.3	0.28	0.1
75	55.55	5.967	1.2	0.072	0.357	0.333	0.08
75	55.55	6.941	1.032	0.078	0.333	0.311	0.09
77.5	57.24	7.057	1.015	0.085	0.355	0.332	0.09
80	58.97	6.389	1.121	0.083	0.383	0.358	0.07
82	60.97	7.393	0.969	0.092	0.369	0.344	0.06
85.5	64.4	7.411	0.967	0.087	0.348	0.326	0.06
86.5	65.13	7.225	0.991	0.083	0.338	0.316	0.06
89.5	67.33	8.338	0.859	0.089	0.317	0.296	0.06
90.5	68.09	7.7	0.93	0.073	0.281	0.263	0.08

Table A.2: Age-depth and U/Th series data for ML1208 Site 37BB continued

Depth	Age	$^{230}Th_{xs,0}$	Mass Flux	^{232}Th	^{232}Th Flux	Dust Flux	aU
(cm)	(ka)	(dpm g^{-1})	(g cm^{-2} kyr^{-1})	(dpm g^{-1})	(μg cm^{-2} kyr^{-1})	(g m^{-2} yr^{-1})	(ppm)
92.5	70.01	7.362	0.973	0.062	0.249	0.233	0.09
93.5	71.55	7.155	1.001	0.056	0.23	0.215	0.09
94.5	72.51	7.404	0.967	0.055	0.22	0.206	0.1
95.5	73.29	7.156	1.001	0.05	0.205	0.191	0.1
96.5	74.02	7.126	1.005	0.044	0.182	0.17	0.08
97.5	74.72	6.886	1.04	0.042	0.179	0.168	0.11
98.5	75.4	6.862	1.044	0.042	0.18	0.168	0.11
100.5	76.78	6.201	1.155	0.04	0.191	0.179	0.1
102.5	78.17	7.639	0.938	0.052	0.2	0.187	0.1
104.5	79.63	8.52	0.841	0.062	0.215	0.201	0.1
106.5	81.76	7.647	0.937	0.056	0.214	0.2	0.07
108.5	84.05	7.926	0.904	0.06	0.222	0.208	0.09
110.5	85.65	7.87	0.91	0.052	0.195	0.182	0.1
112	86.8	6.603	1.085	0.047	0.21	0.196	0.23
113	87.58	7.289	0.983	0.046	0.185	0.173	0.1
114	88.39	5.784	1.238	0.029	0.15	0.14	0.22
116	89.99	6.187	1.158	0.032	0.151	0.141	0.17
118	92.3	6.243	1.147	0.034	0.161	0.15	0.22
120	95.32	5.573	1.285	0.036	0.19	0.177	0.23
122	97.4	5.601	1.279	0.033	0.177	0.165	0.21
124	99.41	9.051	0.791	0.048	0.157	0.146	0.1
124	99.41	6.113	1.172	0.039	0.188	0.175	0.21
125	100.47	8.099	0.884	0.046	0.167	0.156	0.09
126	101.7	7.897	0.907	0.044	0.164	0.153	0.09
128	105.24	10.371	0.691	0.059	0.168	0.157	0.1
130	107.36	9.568	0.749	0.055	0.17	0.159	0.09
132	109.32	8.998	0.796	0.053	0.175	0.164	0.09
134	111.5	9.537	0.751	0.051	0.157	0.146	0.09
136	115.1	9.829	0.729	0.052	0.155	0.145	0.1
138	117.45	9.977	0.718	0.045	0.133	0.124	0.09
140	119.58	9.396	0.762	0.039	0.123	0.115	0.09
142	121.99	9.613	0.745	0.037	0.113	0.105	0.09
144	124.73	9.718	0.737	0.038	0.116	0.108	0.09
146	126.15	9.921	0.722	0.048	0.144	0.134	0.1
148	127.45	8.792	0.815	0.049	0.163	0.153	0.08
149	128.08	5.668	1.264	0.035	0.184	0.172	0.21
150	128.71	8.469	0.846	0.058	0.204	0.191	0.07
151	129.33	8.07	0.888	0.071	0.259	0.242	0.07
152	129.97	8.273	0.866	0.072	0.256	0.239	0.06
154	131.31	8.236	0.87	0.083	0.297	0.277	0.06
155	131.97	7.565	0.947	0.085	0.33	0.309	0.06
156	132.71	6.965	1.028	0.069	0.292	0.273	0.05
158	134.83	7.707	0.929	0.078	0.299	0.279	0.06
159	135.54	8.498	0.843	0.094	0.326	0.305	0.06
160	136.1	8.129	0.881	0.08	0.292	0.273	0.05
161	136.61	7.164	1	0.073	0.302	0.282	0.05
162	137.1	7.769	0.922	0.073	0.277	0.259	0.05
164	138.06	8.825	0.812	0.076	0.256	0.239	0.06
165	138.54	7.322	0.978	0.075	0.304	0.284	0.05
166	139.01	7.1	1.009	0.067	0.279	0.26	0.04
167	139.48	7.379	0.971	0.08	0.32	0.299	0.04
168	139.95	7.468	0.959	0.073	0.287	0.268	0.03
170	140.89	6.637	1.079	0.067	0.296	0.277	0.04

Table A.3: Age-depth and U/Th series data for ML1208 Site 37BB continued

Depth	Age	$^{230}Th_{xs,0}$	Mass Flux	^{232}Th	^{232}Th Flux	Dust Flux	aU
(cm)	(ka)	(dpm g^{-1})	(g cm^{-2} kyr^{-1})	(dpm g^{-1})	(μg cm^{-2} kyr^{-1})	(g m^{-2} yr^{-1})	(ppm)
172	141.82	7.993	0.896	0.073	0.271	0.253	0.05
174	142.77	6.092	1.176	0.061	0.297	0.277	0.05
176	143.72	7.004	1.023	0.074	0.314	0.293	0.06

Appendix B

ML1208-31BB Sediment Core Data

Table B.1: Data from ML1208-31BB retrieved from 2,857 m of water at (4.68°N, -160.05°W).

Depth	Age	$^{230}Th_{xs,0}$	Mass Flux	^{232}Th	^{232}Th Flux	Dust Flux	aU
(cm)	(ka)	(dpm g^{-1})	(g cm^{-2} kyr^{-1})	(dpm g^{-1})	(μg cm^{-2} kyr^{-1})	(g m^{-2} yr^{-1})	(ppm)
13	7.14	6.069	1.205	0.032	0.159	0.149	0.15
14	7.25	5.722	1.278	0.020	0.105	0.098	0.14
15	7.37	5.845	1.251	0.020	0.101	0.095	0.14
16	7.55	6.042	1.210	0.020	0.098	0.091	0.14
17	7.78	5.845	1.251	0.019	0.100	0.094	0.15
18	8.00	5.970	1.225	0.020	0.099	0.093	0.14
19	8.20	5.959	1.227	0.019	0.096	0.090	0.14
20	8.40	5.778	1.266	0.020	0.103	0.096	0.14
21	8.60	6.434	1.137	0.025	0.118	0.110	0.17
22	8.79	5.935	1.232	0.021	0.108	0.101	0.15
23	8.99	6.286	1.164	0.023	0.108	0.101	0.15
24	9.18	5.700	1.283	0.021	0.110	0.103	0.14
25	9.36	6.036	1.212	0.022	0.112	0.105	0.15
26	9.55	6.032	1.213	0.024	0.120	0.112	0.15
27	9.73	5.591	1.308	0.023	0.125	0.117	0.15
28	9.92	5.791	1.263	0.026	0.137	0.128	0.15
29	10.11	6.218	1.176	0.031	0.148	0.138	0.16
30	10.29	5.504	1.329	0.025	0.136	0.127	0.14
31	10.48	5.625	1.300	0.025	0.134	0.125	0.15
32	10.67	5.794	1.262	0.026	0.138	0.129	0.15
33	10.85	5.662	1.292	0.026	0.137	0.128	0.14
34	11.04	5.789	1.263	0.026	0.137	0.128	0.15
35	11.22	5.847	1.251	0.027	0.137	0.128	0.15
36	11.41	5.186	1.410	0.023	0.133	0.124	0.13
37	11.60	5.423	1.349	0.025	0.142	0.132	0.13
38	11.79	6.340	1.154	0.031	0.147	0.138	0.15
39	11.99	6.176	1.184	0.029	0.141	0.132	0.14
40	12.18	5.357	1.365	0.031	0.175	0.163	0.13
41	12.38	5.286	1.384	0.034	0.193	0.181	0.13
42	12.59	5.125	1.427	0.032	0.189	0.177	0.13
43	12.80	5.238	1.396	0.033	0.190	0.178	0.13
44	13.05	5.410	1.352	0.034	0.188	0.176	0.13
45	13.29	5.174	1.414	0.033	0.190	0.177	0.13
46	13.50	5.058	1.446	0.032	0.191	0.178	0.12
46	13.50	5.119	1.429	0.033	0.192	0.180	0.13
47	13.71	5.149	1.420	0.031	0.180	0.168	0.12
48	13.90	5.681	1.287	0.034	0.183	0.171	0.13
49	14.09	5.509	1.328	0.035	0.193	0.180	0.13
50	14.28	5.426	1.348	0.035	0.195	0.183	0.12
51	14.46	5.607	1.304	0.039	0.211	0.197	0.13
52	14.64	6.405	1.142	0.043	0.203	0.190	0.14
53	14.82	5.408	1.352	0.041	0.228	0.213	0.13
54	15.00	5.599	1.306	0.047	0.251	0.234	0.13
54	15.00	10.729	0.682	0.087	0.244	0.228	0.26
55	15.18	5.151	1.420	0.044	0.256	0.240	0.12
55	15.18	5.169	1.415	0.043	0.253	0.236	0.12
56	15.36	5.399	1.355	0.045	0.250	0.234	0.12
57	15.54	5.473	1.336	0.047	0.262	0.244	0.13
58	15.71	5.647	1.295	0.050	0.269	0.252	0.12
58	15.71	5.634	1.298	0.050	0.266	0.249	0.13
59	15.89	5.429	1.347	0.049	0.274	0.256	0.12
60	16.07	5.499	1.330	0.049	0.268	0.250	0.12

Table B.2: Age-depth and U/Th series data for ML1208 Site 31BB continued

Depth	Age	$^{230}Th_{xs,0}$	Mass Flux	^{232}Th	^{232}Th Flux	Dust Flux	aU
(cm)	(ka)	(dpm g^{-1})	(g cm^{-2} kyr^{-1})	(dpm g^{-1})	(μg cm^{-2} kyr^{-1})	(g m^{-2} yr^{-1})	(ppm)
61	16.25	6.017	1.216	0.053	0.265	0.248	0.14
62	16.43	5.612	1.303	0.050	0.268	0.251	0.13
63	16.61	5.888	1.242	0.052	0.264	0.247	0.13
64	16.78	5.623	1.301	0.049	0.261	0.243	0.13
65	16.96	5.708	1.281	0.049	0.258	0.241	0.13
66	17.14	5.362	1.364	0.049	0.275	0.257	0.15
67	17.32	5.142	1.422	0.050	0.294	0.275	0.16
68	17.50	5.976	1.224	0.051	0.259	0.242	0.13
69	17.69	6.560	1.115	0.054	0.246	0.230	0.14
70	17.87	5.970	1.225	0.051	0.256	0.239	0.14
71	18.06	6.224	1.175	0.052	0.254	0.237	0.14
72	18.26	6.559	1.115	0.054	0.246	0.230	0.13
73	18.45	6.788	1.077	0.058	0.257	0.240	0.15
74	18.66	4.587	1.595	0.042	0.276	0.258	0.17
75	18.92	6.587	1.110	0.058	0.266	0.249	0.14
76	19.64	5.940	1.231	0.049	0.250	0.234	0.12
77	20.47	6.305	1.160	0.050	0.240	0.225	0.12
78	21.29	5.960	1.227	0.051	0.257	0.241	0.12
80	22.94	5.708	1.281	0.045	0.237	0.222	0.12
82	24.58	5.756	1.271	0.049	0.256	0.240	0.11
84	26.02	6.403	1.142	0.053	0.248	0.232	0.12
86	27.43	6.203	1.179	0.054	0.262	0.245	0.12
88	28.84	6.140	1.191	0.054	0.266	0.249	0.12
90	30.09	4.139	1.767	0.037	0.268	0.250	0.08
92	30.62	5.731	1.276	0.048	0.252	0.235	0.12
94	31.10	6.032	1.212	0.050	0.252	0.236	0.13
97	31.81	5.733	1.276	0.043	0.227	0.212	0.13
98	32.04	5.174	1.414	0.039	0.228	0.213	0.13
100	32.50	5.706	1.282	0.042	0.220	0.206	0.14
102	32.96	5.599	1.306	0.042	0.226	0.211	0.13
104	33.41	6.019	1.215	0.045	0.227	0.212	0.14
106	33.88	5.970	1.225	0.045	0.227	0.212	0.13
108	34.35	5.936	1.232	0.044	0.225	0.210	0.13
110	34.84	5.679	1.288	0.044	0.232	0.217	0.14
110	34.84	5.367	1.363	0.042	0.235	0.220	0.14
112	35.40	5.918	1.236	0.042	0.215	0.201	0.16
114	35.92	5.313	1.377	0.036	0.203	0.190	0.17
116	36.41	5.551	1.318	0.037	0.200	0.187	0.26
118	36.88	5.475	1.336	0.037	0.202	0.188	0.37
120	37.34	5.278	1.386	0.038	0.216	0.202	0.88
122	37.80	4.535	1.613	0.031	0.209	0.196	1.00
124	38.26	4.515	1.620	0.034	0.227	0.212	1.72
126	38.72	4.319	1.694	0.033	0.230	0.215	1.82
126	38.72	4.534	1.613	0.035	0.235	0.219	1.88
128	39.18	4.242	1.724	0.034	0.243	0.227	1.76
130	39.65	4.486	1.630	0.035	0.237	0.221	1.66
134	40.70	4.890	1.496	0.037	0.229	0.214	1.02
136	41.27	4.937	1.482	0.039	0.238	0.222	0.80
138	41.81	5.162	1.417	0.042	0.247	0.231	0.64
140	42.34	5.020	1.457	0.038	0.230	0.215	0.48
142	42.87	4.995	1.464	0.039	0.235	0.220	0.41
144	43.40	5.171	1.414	0.038	0.221	0.206	0.37

Table B.3: Age-depth and U/Th series data for ML1208 Site 31BB continued

Depth	Age	$^{230}Th_{xs,0}$	Mass Flux	^{232}Th	^{232}Th Flux	Dust Flux	aU
(cm)	(ka)	(dpm g^{-1})	(g cm^{-2} kyr^{-1})	(dpm g^{-1})	(μg cm^{-2} kyr^{-1})	(g m^{-2} yr^{-1})	(ppm)
146	43.93	5.466	1.338	0.039	0.214	0.200	0.36
148	44.46	5.931	1.233	0.043	0.219	0.204	0.43
148	44.46	5.395	1.356	0.037	0.208	0.194	0.37
150	45.00	5.599	1.306	0.039	0.211	0.198	0.41
152	45.56	5.310	1.377	0.038	0.214	0.200	0.37
154	46.26	5.394	1.356	0.037	0.206	0.193	0.34
156	46.96	4.957	1.475	0.034	0.206	0.192	0.35
158	47.64	5.326	1.373	0.036	0.203	0.190	0.38
160	48.30	5.051	1.448	0.036	0.212	0.198	0.34
162	48.96	5.283	1.384	0.037	0.212	0.198	0.34
164	49.62	5.050	1.448	0.038	0.225	0.210	0.37
166	50.29	4.950	1.478	0.033	0.200	0.187	0.40
168	50.98	4.968	1.472	0.032	0.194	0.182	0.44
170	51.75	0.667	10.963	0.004	0.185	0.173	0.07
172	52.47	4.814	1.519	0.029	0.184	0.172	0.52
174	53.12	4.731	1.546	0.029	0.186	0.173	0.58
176	53.77	4.740	1.543	0.029	0.186	0.174	0.62
178	54.41	4.719	1.550	0.032	0.207	0.194	0.66
180	55.06	5.075	1.441	0.034	0.204	0.191	0.66
182	55.71	5.104	1.433	0.034	0.202	0.189	0.56
184	56.39	4.284	1.707	0.031	0.220	0.206	0.48
186	57.11	5.229	1.399	0.039	0.226	0.212	0.63
188	57.74	4.870	1.502	0.037	0.229	0.214	0.54
190	58.35	4.637	1.577	0.036	0.232	0.217	0.47
192	58.96	4.686	1.561	0.041	0.262	0.245	0.41
194	59.55	5.083	1.439	0.045	0.268	0.250	0.40
196	60.15	5.167	1.415	0.049	0.287	0.269	0.37
196	60.15	5.297	1.381	0.051	0.288	0.269	0.36
198	60.75	4.880	1.499	0.048	0.294	0.275	0.32
198	60.75	4.631	1.579	0.045	0.292	0.273	0.30
200	61.36	4.199	1.742	0.039	0.283	0.264	0.32
200	61.36	4.960	1.475	0.044	0.268	0.250	0.27
204	62.64	5.172	1.414	0.051	0.296	0.277	0.37
208	63.47	4.862	1.504	0.049	0.302	0.282	0.35
209	63.66	5.149	1.420	0.049	0.287	0.268	0.36
215	64.71	5.004	1.462	0.048	0.290	0.271	0.38
220	65.56	5.572	1.313	0.052	0.281	0.262	0.32
220	65.56	5.287	1.383	0.049	0.279	0.261	0.27
224	66.24	5.315	1.376	0.047	0.267	0.249	0.21
229	67.10	3.120	2.344	0.025	0.239	0.223	0.15
229	67.10	6.051	1.209	0.051	0.255	0.238	0.18
233	67.81	5.728	1.277	0.047	0.246	0.230	0.16
235	68.20	5.928	1.234	0.043	0.219	0.205	0.16
238	69.16	5.681	1.287	0.042	0.221	0.206	0.14
240	69.93	5.870	1.246	0.039	0.201	0.187	0.15
245	71.80	6.338	1.154	0.042	0.202	0.188	0.14
251	74.20	6.126	1.194	0.037	0.180	0.168	0.13
256	76.43	5.648	1.295	0.032	0.173	0.161	0.15
260	78.18	5.143	1.422	0.026	0.154	0.144	0.19
267	82.53	5.600	1.306	0.028	0.152	0.142	0.26
269	83.94	5.658	1.293	0.029	0.153	0.143	0.25

Table B.4: Age-depth and U/Th series data for ML1208 Site 31BB continued

Depth	Age	$^{230}Th_{xs,0}$	Mass Flux	^{232}Th	^{232}Th Flux	Dust Flux	aU
(cm)	(ka)	(dpm g^{-1})	(g cm^{-2} kyr^{-1})	(dpm g^{-1})	(μg cm^{-2} kyr^{-1})	(g m^{-2} yr^{-1})	(ppm)
272	85.01	5.608	1.304	0.029	0.158	0.147	0.24
274	85.31	6.301	1.161	0.035	0.168	0.157	0.27
278	85.87	6.121	1.195	0.038	0.185	0.173	0.26
281	86.27	6.360	1.150	0.043	0.203	0.190	0.26
283	86.54	6.298	1.161	0.044	0.210	0.196	0.26
285	86.80	5.958	1.228	0.040	0.202	0.189	0.26
285	86.80	6.120	1.195	0.042	0.207	0.193	0.27
285	86.80	8.172	0.895	0.060	0.223	0.208	0.20
287	87.06	5.560	1.315	0.039	0.213	0.199	0.27
289	87.31	4.900	1.493	0.035	0.213	0.199	0.26
290	87.44	4.836	1.512	0.032	0.197	0.184	0.24
292	87.70	4.914	1.488	0.031	0.191	0.179	0.24
294	87.96	5.064	1.444	0.029	0.174	0.163	0.28
294	87.96	5.621	1.301	0.034	0.183	0.171	0.25
294	87.96	5.350	1.367	0.033	0.185	0.173	0.24
295	88.08	4.333	1.688	0.030	0.209	0.196	0.20
296	88.21	5.764	1.269	0.031	0.160	0.150	0.22
297	88.34	5.465	1.338	0.031	0.171	0.160	0.22
298	88.47	5.761	1.269	0.031	0.163	0.153	0.21
299	88.60	6.442	1.135	0.039	0.183	0.171	0.24
300	88.73	5.862	1.248	0.032	0.164	0.154	0.19
302	89.00	6.188	1.182	0.034	0.164	0.153	0.18
304	89.27	6.246	1.171	0.032	0.154	0.144	0.16
305	89.41	6.316	1.158	0.033	0.159	0.148	0.16
306	89.54	5.626	1.300	0.036	0.191	0.179	0.17
308	89.83	4.972	1.471	0.034	0.204	0.191	0.17
310	90.13	5.545	1.319	0.037	0.199	0.186	0.19
312	90.68	4.754	1.539	0.034	0.214	0.200	0.17
314	92.18	5.646	1.295	0.028	0.148	0.138	0.15
314	92.18	3.876	1.887	0.023	0.178	0.166	0.14
315	92.92	5.981	1.223	0.029	0.145	0.136	0.19
316	93.66	5.614	1.303	0.027	0.145	0.135	0.18
317	94.40	6.437	1.136	0.034	0.158	0.147	0.21
317	94.40	5.314	1.376	0.028	0.161	0.150	0.20
319	95.90	6.188	1.182	0.032	0.158	0.148	0.23
321	97.13	6.235	1.173	0.033	0.159	0.149	0.25
323	98.28	6.179	1.184	0.032	0.155	0.145	0.28
325	99.42	5.504	1.329	0.029	0.158	0.148	0.33
327	100.57	6.584	1.111	0.033	0.151	0.141	0.40
330	102.46	5.854	1.249	0.030	0.152	0.142	0.35
332	103.76	6.653	1.099	0.034	0.152	0.142	0.35
336	106.31	6.523	1.121	0.036	0.167	0.156	0.30
340	108.49	6.435	1.137	0.034	0.161	0.151	0.25
340	108.49	6.407	1.142	0.035	0.165	0.154	0.27
342	109.34	6.404	1.142	0.031	0.146	0.136	0.27
344	110.19	6.759	1.082	0.033	0.148	0.138	0.28
346	111.04	7.531	0.971	0.039	0.156	0.145	0.28
348	111.90	6.298	1.161	0.034	0.164	0.153	0.22

Table B.5: Age-depth and U/Th series data for ML1208 Site 31BB continued

Depth	Age	$^{230}Th_{xs,0}$	Mass Flux	^{232}Th	^{232}Th Flux	Dust Flux	aU
(cm)	(ka)	(dpm g^{-1})	(g cm^{-2} kyr^{-1})	(dpm g^{-1})	(μg cm^{-2} kyr^{-1})	(g m^{-2} yr^{-1})	(ppm)
350	112.77	6.423	1.139	0.035	0.165	0.155	0.21
352	113.27	6.988	1.047	0.039	0.168	0.157	0.22
354	113.72	6.455	1.133	0.033	0.154	0.143	0.19
356	114.15	8.481	0.862	0.038	0.136	0.127	0.22
358	114.57	9.124	0.802	0.042	0.137	0.128	0.23
360	114.98	8.279	0.883	0.038	0.138	0.129	0.21
362	115.39	8.706	0.840	0.041	0.141	0.132	0.22
364	115.81	7.683	0.952	0.034	0.133	0.125	0.18
366	116.22	7.327	0.998	0.035	0.145	0.135	0.17
368	116.64	7.788	0.939	0.036	0.140	0.131	0.18
370	117.07	8.766	0.834	0.035	0.120	0.112	0.20
372	117.52	7.957	0.919	0.036	0.136	0.127	0.19
373	117.75	6.946	1.053	0.031	0.135	0.126	0.19
374	118.02	6.435	1.137	0.032	0.148	0.138	0.18
376	118.81	5.676	1.289	0.029	0.152	0.142	0.16
378	119.57	7.218	1.013	0.026	0.108	0.101	0.16
380	120.32	7.700	0.950	0.027	0.107	0.100	0.16
382	121.06	6.599	1.108	0.022	0.101	0.094	0.14
384	121.81	7.341	0.996	0.029	0.121	0.113	0.16
386	122.56	7.141	1.024	0.026	0.108	0.101	0.15
388	123.37	6.670	1.097	0.026	0.116	0.108	0.15
390	124.12	6.607	1.107	0.023	0.106	0.099	0.14
392	124.81	6.817	1.073	0.025	0.112	0.105	0.13
394	125.49	5.926	1.234	0.022	0.110	0.103	0.13
396	126.15	5.532	1.322	0.024	0.131	0.123	0.13
398	126.81	5.737	1.275	0.027	0.142	0.132	0.14
398	126.81	5.426	1.348	0.025	0.141	0.131	0.13
400	127.48	5.226	1.399	0.026	0.147	0.138	0.14
402	128.15	7.506	0.974	0.029	0.118	0.110	0.17
403	128.50	9.462	0.773	0.044	0.141	0.132	0.25
403	128.50	6.412	1.141	0.029	0.138	0.129	0.17
404	128.87	6.204	1.179	0.027	0.132	0.123	0.16
408	130.00	5.203	1.406	0.029	0.166	0.156	0.19
408	130.00	5.379	1.360	0.029	0.161	0.151	0.19
410	130.49	5.957	1.228	0.035	0.177	0.165	0.21
410	130.49	5.807	1.259	0.034	0.177	0.166	0.21
411	130.74	6.318	1.158	0.037	0.176	0.164	0.20
412	130.98	6.250	1.170	0.040	0.191	0.179	0.21
412	130.98	6.345	1.153	0.039	0.186	0.174	0.20
413	131.22	6.197	1.180	0.039	0.192	0.180	0.20
414	131.45	5.091	1.437	0.039	0.232	0.216	0.18
417	132.17	3.634	2.013	0.028	0.236	0.221	0.16
418	132.41	5.048	1.449	0.045	0.269	0.251	0.20
418	132.41	3.966	1.844	0.030	0.229	0.214	0.17
418	132.41	3.973	1.841	0.030	0.229	0.214	0.17
420	132.88	4.256	1.718	0.040	0.281	0.263	0.18
422	133.37	4.870	1.502	0.047	0.291	0.272	0.20
424	133.87	4.871	1.501	0.045	0.279	0.260	0.20
424	133.87	4.099	1.785	0.037	0.270	0.252	0.17
425	134.12	4.125	1.773	0.037	0.267	0.250	0.18
424	133.87	4.050	1.806	0.037	0.278	0.260	0.17

Table B.6: Age-depth and U/Th series data for ML1208 Site 31BB continued

Depth	Age	$^{230}Th_{xs,0}$	Mass Flux	^{232}Th	^{232}Th Flux	Dust Flux	aU
(cm)	(ka)	(dpm g^{-1})	(g cm^{-2} kyr^{-1})	(dpm g^{-1})	(μg cm^{-2} kyr^{-1})	(g m^{-2} yr^{-1})	(ppm)
426	134.40	5.195	1.408	0.049	0.282	0.264	0.23
426	134.40	5.136	1.424	0.044	0.259	0.242	0.19
428	134.87	4.520	1.618	0.038	0.254	0.238	0.20
430	135.23	5.602	1.306	0.050	0.268	0.251	0.22
431	135.41	5.488	1.333	0.048	0.265	0.248	0.21
433	135.75	3.889	1.881	0.036	0.280	0.262	0.25
434	135.92	5.947	1.230	0.048	0.245	0.229	0.22
436	136.25	4.833	1.513	0.040	0.249	0.233	0.19
433	135.75	5.159	1.418	0.043	0.249	0.233	0.20
438	136.58	4.108	1.780	0.036	0.266	0.249	0.22
440	136.91	4.427	1.652	0.039	0.264	0.247	0.31
440	136.91	5.527	1.323	0.044	0.239	0.223	0.21
441	137.07	5.480	1.335	0.047	0.257	0.241	0.24
442	137.23	5.262	1.390	0.045	0.257	0.240	0.23
444	137.56	4.780	1.530	0.041	0.257	0.240	0.25
446	137.88	5.374	1.361	0.045	0.250	0.234	0.25
448	138.21	5.780	1.265	0.049	0.257	0.240	0.28
451	138.70	5.513	1.327	0.046	0.253	0.237	0.27
451	138.70	5.785	1.264	0.050	0.261	0.244	0.29
452	138.87	5.475	1.336	0.049	0.271	0.253	0.29
454	139.22	4.598	1.591	0.042	0.275	0.257	0.27
456	139.58	5.053	1.448	0.045	0.269	0.251	0.27
458	139.99	4.309	1.698	0.040	0.281	0.263	0.27
460	140.31	5.211	1.404	0.043	0.250	0.234	0.28
460	140.31	4.918	1.487	0.042	0.255	0.238	0.26
460	140.31	4.302	1.700	0.035	0.244	0.228	0.18
461	140.43	4.022	1.819	0.038	0.286	0.267	0.26
462	140.54	3.841	1.904	0.037	0.293	0.274	0.27
464	140.74	3.684	1.985	0.037	0.299	0.279	0.25
466	140.92	3.889	1.881	0.036	0.280	0.262	0.25
468	141.10	3.672	1.992	0.038	0.313	0.293	0.28
470	141.26	3.555	2.057	0.035	0.294	0.275	0.27
471	141.33	2.911	2.513	0.031	0.324	0.303	0.27
472	141.40	2.812	2.601	0.033	0.351	0.328	0.28
472	141.40	2.973	2.460	0.032	0.321	0.300	0.28

Appendix C

ML1208-17PC Sediment Core Data

Table C.1: Data from ML1208-17PC retrieved from 2,926 m of water at (.48°N, -156.45°W).

Depth	Age	$^{230}Th_{xs,0}$	Mass Flux	^{232}Th	^{232}Th Flux	Dust Flux	aU
(cm)	(ka)	(dpm g^{-1})	(g cm^{-2} kyr^{-1})	(dpm g^{-1})	(μg cm^{-2} kyr^{-1})	(g m^{-2} yr^{-1})	(ppm)
0	4.97	5.099	1.469	0.021	0.127	0.119	0.21
1	5.18	4.213	1.778	0.020	0.146	0.136	0.20
2	5.38	5.281	1.418	0.021	0.120	0.112	0.20
3	5.58	5.053	1.482	0.022	0.132	0.123	0.26
4	5.77	5.125	1.462	0.020	0.120	0.112	0.23
5	5.96	4.983	1.503	0.019	0.118	0.111	0.20
6	6.14	4.025	1.861	0.015	0.118	0.110	0.16
7	6.33	5.136	1.458	0.020	0.118	0.111	0.20
9	6.71	4.786	1.565	0.019	0.123	0.115	0.19
10	6.90	5.069	1.478	0.020	0.121	0.113	0.20
11	7.09	4.586	1.633	0.020	0.134	0.125	0.19
12	7.29	4.512	1.660	0.018	0.121	0.113	0.18
13	7.49	4.780	1.567	0.020	0.126	0.118	0.18
14	7.70	4.562	1.642	0.020	0.136	0.127	0.17
15	7.91	4.490	1.668	0.020	0.136	0.127	0.17
16	8.13	4.694	1.596	0.021	0.139	0.130	0.17
17	8.37	4.316	1.736	0.021	0.149	0.139	0.15
18	8.61	4.452	1.683	0.021	0.148	0.138	0.08
19	8.89	5.080	1.474	0.026	0.156	0.145	0.17
20	9.20	4.280	1.750	0.018	0.128	0.120	0.09
21	9.59	4.796	1.562	0.022	0.140	0.131	0.09
22	10.12	4.307	1.739	0.026	0.184	0.172	0.14
23	10.49	4.371	1.714	0.025	0.176	0.164	0.15
24	10.75	4.909	1.526	0.028	0.178	0.166	0.16
25	10.99	4.189	1.788	0.025	0.185	0.173	0.14
26	11.21	4.086	1.833	0.023	0.175	0.163	0.13
27	11.44	4.291	1.746	0.026	0.185	0.173	0.13
27	11.44	4.295	1.744	0.027	0.192	0.180	0.13
28	11.66	4.205	1.781	0.026	0.190	0.177	0.13
29	11.89	4.146	1.807	0.026	0.196	0.183	0.12
30	12.12	4.198	1.784	0.029	0.211	0.197	0.12
31	12.40	4.167	1.798	0.029	0.216	0.202	0.12
31	12.40	4.510	1.661	0.033	0.228	0.213	0.13
32	12.82	7.798	0.961	0.058	0.228	0.213	0.23
33	13.54	4.489	1.669	0.031	0.217	0.202	0.13
34	14.07	3.936	1.903	0.029	0.227	0.212	0.12
35	14.53	4.693	1.596	0.035	0.233	0.218	0.12
36	14.93	4.465	1.678	0.036	0.246	0.230	0.12
37	15.33	4.328	1.731	0.031	0.221	0.206	0.12
38	15.71	4.319	1.734	0.036	0.258	0.241	0.11
39	16.07	4.111	1.822	0.034	0.259	0.242	0.10
40	16.42	3.967	1.888	0.034	0.265	0.247	0.10
41	16.76	4.440	1.687	0.042	0.294	0.274	0.10
42	17.10	4.744	1.579	0.043	0.280	0.262	0.12
43	17.44	4.112	1.822	0.039	0.289	0.270	0.09
44	17.77	4.284	1.748	0.041	0.293	0.274	0.10
45	18.10	4.423	1.693	0.039	0.271	0.253	0.10

Table C.2: Age-depth and U/Th series data for ML1208 Site 17PC continued

Depth	Age	$^{230}Th_{xs,0}$	Mass Flux	^{232}Th	^{232}Th Flux	Dust Flux	aU
(cm)	(ka)	(dpm g^{-1})	(g cm^{-2} kyr^{-1})	(dpm g^{-1})	(μg cm^{-2} kyr^{-1})	(g m^{-2} yr^{-1})	(ppm)
46	18.42	4.173	1.795	0.038	0.283	0.265	0.09
47	18.73	4.577	1.637	0.043	0.292	0.273	0.10
48	19.05	4.515	1.659	0.040	0.274	0.256	0.09
49	19.37	4.231	1.770	0.040	0.291	0.272	0.10
50	19.70	4.432	1.690	0.042	0.293	0.274	0.11
51	20.04	4.693	1.596	0.043	0.282	0.264	0.08
52	20.37	3.065	2.444	0.028	0.280	0.262	0.05
53	20.72	4.592	1.631	0.042	0.285	0.266	0.09
54	21.08	4.730	1.584	0.044	0.288	0.269	0.10
55	21.45	4.578	1.636	0.042	0.284	0.265	0.10
56	21.85	4.479	1.672	0.044	0.302	0.283	0.12
57	22.27	4.252	1.762	0.040	0.289	0.270	0.10
58	22.76	4.311	1.738	0.039	0.281	0.263	0.09
59	23.39	4.499	1.665	0.040	0.277	0.259	0.09
60	24.31	4.601	1.628	0.041	0.274	0.256	0.11
64	26.59	4.243	1.765	0.040	0.288	0.269	0.24
68	28.37	5.156	1.453	0.045	0.270	0.253	0.85
72	30.08	4.076	1.838	0.038	0.287	0.269	1.32
76	31.88	4.045	1.852	0.038	0.294	0.274	2.63
80	34.44	3.631	2.063	0.036	0.302	0.282	2.92
84	37.05	3.792	1.976	0.037	0.302	0.282	2.38
88	38.84	3.654	2.050	0.034	0.286	0.267	1.89
92	40.53	3.489	2.147	0.028	0.250	0.234	1.09
96	42.30	4.273	1.753	0.037	0.269	0.252	1.21
100	44.43	3.950	1.897	0.031	0.242	0.226	1.10
104	46.43	3.554	2.107	0.029	0.254	0.237	1.21
108	47.28	3.397	2.205	0.032	0.288	0.269	1.20
112	48.00	3.631	2.063	0.031	0.263	0.245	0.74
116	48.65	3.800	1.971	0.030	0.245	0.229	0.54
120	49.26	3.701	2.024	0.027	0.225	0.210	0.31
124	49.87	3.819	1.962	0.030	0.240	0.224	0.32
128	50.48	3.715	2.016	0.028	0.234	0.218	0.33
132	51.09	4.037	1.856	0.030	0.229	0.214	0.51
136	51.70	3.978	1.883	0.030	0.231	0.216	0.78
140	52.34	3.619	2.070	0.026	0.225	0.211	0.73
144	52.95	3.685	2.033	0.027	0.226	0.211	0.85
148	53.61	3.467	2.160	0.026	0.228	0.213	1.02
152	54.32	3.585	2.089	0.026	0.227	0.212	1.27
156	55.13	3.318	2.257	0.027	0.247	0.231	1.28
156	55.13	3.311	2.262	0.029	0.274	0.256	1.35
160	56.26	6.199	1.208	0.052	0.259	0.242	1.77
164	58.52	3.751	1.997	0.031	0.255	0.238	0.58
164	58.52	7.095	1.056	0.060	0.263	0.246	1.18
168	59.97	3.893	1.924	0.039	0.313	0.293	0.39
174	61.94	4.265	1.756	0.043	0.313	0.293	0.29
178	63.20	4.247	1.764	0.041	0.301	0.281	0.24

Table C.3: Age-depth and U/Th series data for ML1208 Site 17PC continued

Depth	Age	$^{230}Th_{xs,0}$	Mass Flux	^{232}Th	^{232}Th Flux	Dust Flux	aU
(cm)	(ka)	(dpm g^{-1})	(g cm^{-2} kyr^{-1})	(dpm g^{-1})	(μg cm^{-2} kyr^{-1})	(g m^{-2} yr^{-1})	(ppm)
182	64.53	4.456	1.681	0.041	0.282	0.264	0.24
186	66.09	5.198	1.441	0.047	0.280	0.262	0.29
188	67.16	4.676	1.602	0.039	0.255	0.238	0.30
192	71.07	4.571	1.639	0.032	0.218	0.204	0.30
198	75.99	5.053	1.482	0.033	0.202	0.189	0.23
202	79.44	4.781	1.567	0.029	0.186	0.174	0.21
208	81.71	4.342	1.725	0.024	0.172	0.160	0.18
210	82.37	4.222	1.774	0.024	0.177	0.165	0.20
212	83.01	4.672	1.603	0.026	0.172	0.161	0.22
214	83.63	4.954	1.512	0.032	0.201	0.188	0.23
218	84.86	4.761	1.573	0.030	0.193	0.181	0.32
220	85.49	4.097	1.828	0.024	0.179	0.167	0.42
222	86.13	3.964	1.890	0.022	0.171	0.160	0.35
224	86.79	4.397	1.703	0.027	0.189	0.177	0.35
226	87.47	4.894	1.531	0.036	0.227	0.212	0.32
228	88.19	5.036	1.487	0.029	0.178	0.167	0.32
230	89.01	4.814	1.556	0.033	0.211	0.197	0.30
232	89.98	4.703	1.593	0.032	0.213	0.199	0.30
234	91.49	5.192	1.443	0.034	0.203	0.190	0.31
238	93.10	4.924	1.521	0.030	0.190	0.177	0.27
242	94.37	4.628	1.618	0.026	0.175	0.164	0.22
246	95.52	4.706	1.592	0.025	0.163	0.152	0.24
248	96.11	4.756	1.575	0.025	0.162	0.151	0.24
254	97.85	4.658	1.608	0.023	0.154	0.144	0.27
258	99.18	4.499	1.665	0.022	0.151	0.141	0.29
262	101.28	4.448	1.684	0.022	0.153	0.143	0.32
264	102.46	4.772	1.570	0.024	0.155	0.145	0.38
268	104.00	4.708	1.591	0.024	0.160	0.150	0.35
272	105.29	4.486	1.670	0.024	0.164	0.153	0.29
276	106.51	4.435	1.689	0.026	0.179	0.167	0.25
281	108.03	4.646	1.612	0.026	0.174	0.163	0.26
283	108.65	4.684	1.599	0.028	0.184	0.172	0.26
285	109.31	4.933	1.519	0.031	0.191	0.179	0.26
289	110.88	4.466	1.677	0.026	0.182	0.170	0.25
293	113.89	4.831	1.551	0.026	0.164	0.154	0.28
295	115.06	5.300	1.413	0.026	0.150	0.140	0.33
297	116.11	5.223	1.432	0.028	0.167	0.156	0.37
298	116.64	4.990	1.511	0.024	0.150	0.140	0.37
299	117.16	5.180	1.458	0.024	0.147	0.137	0.40
300	117.68	4.938	1.518	0.025	0.155	0.145	0.38
303	119.25	4.816	1.555	0.024	0.153	0.143	0.47
304	119.81	4.838	1.548	0.022	0.142	0.132	0.41
305	120.44	4.769	1.571	0.022	0.143	0.134	0.46
305	120.44	4.966	1.508	0.020	0.125	0.117	0.43

Table C.4: Age-depth and U/Th series data for ML1208 Site 17PC continued

Depth	Age	$^{230}Th_{xs,0}$	Mass Flux	^{232}Th	^{232}Th Flux	Dust Flux	aU
(cm)	(ka)	(dpm g^{-1})	(g cm^{-2} kyr^{-1})	(dpm g^{-1})	(μg cm^{-2} kyr^{-1})	(g m^{-2} yr^{-1})	(ppm)
307	122.05	4.171	1.796	0.020	0.145	0.135	0.44
308	122.81	4.463	1.678	0.021	0.148	0.138	0.47
309	123.30	4.266	1.756	0.021	0.149	0.140	0.44
310	123.71	4.635	1.616	0.022	0.146	0.136	0.51
311	124.06	4.148	1.806	0.020	0.151	0.141	0.43
312	124.39	4.274	1.753	0.019	0.134	0.126	0.43
313	124.72	4.100	1.827	0.019	0.147	0.137	0.47
314	125.03	4.518	1.658	0.021	0.143	0.133	0.46
315	125.33	4.157	1.802	0.020	0.149	0.139	0.43
316	125.63	4.644	1.613	0.022	0.148	0.138	0.45
317	125.91	4.591	1.632	0.022	0.146	0.137	0.48
318	126.18	4.227	1.772	0.021	0.150	0.140	0.42
319	126.46	4.788	1.564	0.023	0.147	0.138	0.47
320	126.73	4.724	1.586	0.024	0.154	0.144	0.48
321	127.00	4.510	1.661	0.024	0.166	0.155	0.50
322	127.26	4.720	1.587	0.024	0.159	0.149	0.50
323	127.53	4.360	1.718	0.024	0.169	0.158	0.53
324	127.79	4.308	1.739	0.023	0.168	0.157	0.55
324	127.79	4.944	1.526	0.023	0.146	0.136	0.56
325	128.06	4.090	1.832	0.025	0.188	0.176	0.51
326	128.33	3.552	2.109	0.024	0.206	0.193	0.53
327	128.59	3.801	1.971	0.025	0.204	0.191	0.55
328	128.86	4.019	1.864	0.028	0.213	0.199	0.55
329	129.13	3.271	2.290	0.027	0.255	0.239	0.49
330	129.41	3.065	2.444	0.025	0.257	0.240	0.44
331	129.69	3.855	1.943	0.032	0.255	0.238	0.57
332	129.97	3.710	2.019	0.033	0.271	0.253	0.56
333	130.26	3.254	2.302	0.031	0.295	0.276	0.51
334	130.57	2.867	2.613	0.031	0.330	0.308	0.46
335	130.89	2.943	2.545	0.028	0.298	0.279	0.46
336	131.23	3.199	2.342	0.032	0.308	0.287	0.53
337	131.59	3.349	2.237	0.036	0.334	0.312	0.57
338	131.99	3.280	2.283	0.034	0.320	0.299	0.60
339	132.45	3.146	2.381	0.036	0.352	0.329	0.62
340	133.10	3.082	2.430	0.034	0.338	0.316	0.60
341	133.95	3.016	2.483	0.034	0.348	0.325	0.61
342	134.56	3.358	2.231	0.039	0.358	0.335	0.75
343	135.09	3.177	2.358	0.035	0.344	0.322	0.71
344	135.58	3.638	2.059	0.038	0.322	0.301	0.77
345	136.04	3.352	2.234	0.035	0.326	0.305	0.83
346	136.46	4.372	1.713	0.038	0.270	0.253	1.01
346	136.46	3.878	1.932	0.039	0.311	0.291	0.98
347	136.87	4.186	1.789	0.039	0.289	0.271	1.00
348	137.26	4.237	1.768	0.038	0.273	0.256	0.97
349	137.65	4.529	1.654	0.038	0.262	0.245	1.03

Table C.5: Age-depth and U/Th series data for ML1208 Site 17PC continued

Depth	Age	$^{230}Th_{xs,0}$	Mass Flux	^{232}Th	^{232}Th Flux	Dust Flux	aU
(cm)	(ka)	(dpm g^{-1})	(g cm^{-2} kyr^{-1})	(dpm g^{-1})	(μg cm^{-2} kyr^{-1})	(g m^{-2} yr^{-1})	(ppm)
349	137.65	4.351	1.722	0.039	0.279	0.261	1.03
350	138.03	4.691	1.601	0.042	0.278	0.260	1.09
351	138.40	4.307	1.762	0.038	0.278	0.260	1.02
352	138.79	4.785	1.514	0.042	0.262	0.245	1.14
353	139.17	4.806	1.583	0.043	0.279	0.260	1.12
354	139.56	4.588	1.623	0.042	0.280	0.261	1.03
355	139.95	4.503	1.711	0.042	0.296	0.277	1.05
356	140.34	4.489	1.682	0.042	0.290	0.271	0.95
357	140.75	4.001	1.875	0.038	0.295	0.276	0.88
361	142.52	3.810	1.954	0.033	0.268	0.251	0.62
361	142.52	3.990	1.877	0.039	0.298	0.279	0.66
362	143.09	3.904	1.937	0.037	0.299	0.280	0.65
363	143.88	3.959	1.924	0.036	0.289	0.270	0.62
364	144.77	3.985	1.903	0.037	0.286	0.268	0.60
366	145.89	3.925	1.968	0.036	0.293	0.273	0.56
368	146.81	3.691	2.029	0.035	0.294	0.275	0.50
370	147.65	3.790	1.976	0.037	0.301	0.281	0.46
372	148.47	4.132	1.813	0.040	0.295	0.276	0.48
374	149.28	3.633	2.062	0.035	0.295	0.276	0.42
376	150.1	3.85197304					0.43
378	150.9	3.905000624					0.41
380	151.7	3.860174149					0.40
384	153.8	4.297114009					0.46
386	155.3	4.724985					0.57
390	156.7	4.138883147					0.63
394	157.8	4.093014337					0.98
396	158.3	2.990427644					0.85
398	158.9	3.425696806					1.11
400	159.4	3.666879708					1.21
402	159.9	4.132790507					1.61
404	160.4	4.489021188					1.83
406	160.9	4.985887881					2.01
408	161.4	4.345939229					2.11
410	161.9	4.079619893					1.90
412	162.5	4.190998645					1.94
414	163.0	3.646756835					1.65
416	163.6	3.155689049					1.19
418	164.3	3.843399823					1.33
420	165.0	3.612547924					1.20
422	166.0	3.558557659					1.08
424	167.4	3.178328743					0.93
426	168.3	3.205883296					0.87
428	169.1	3.459639731					0.82

Table C.6: Age-depth and U/Th series data for ML1208 Site 17PC continued

Depth	Age	$^{230}Th_{xs,0}$	Mass Flux	^{232}Th	^{232}Th Flux	Dust Flux	aU
(cm)	(ka)	(dpm g^{-1})	(g cm^{-2} kyr^{-1})	(dpm g^{-1})	(μg cm^{-2} kyr^{-1})	(g m^{-2} yr^{-1})	(ppm)
430	169.8	3.775024402					0.77
434	171.2	3.575672298					0.31
436	171.9	3.567516134					0.32
438	172.6	3.434559941					0.29
440	173.3	3.248582525					0.26
442	173.9	4.007819072					0.57
444	174.7	3.430034587					0.47
446	175.5	3.778756258					0.42
448	176.4	3.881780922					0.26
450	177.7	3.551324923					0.35
452	179.5	3.751103835					0.31
454	180.8	5.03117027					0.36
456	181.9	4.896575169					0.33
458	183.0	4.129562015					0.33
460	184.0	4.642711768					0.36
462	185.1	4.686926231					0.34
464	186.3	3.531739234					0.29
466	187.9	3.637422432					0.30
468	190.3	4.827737127					0.40
470	192.1	5.038646299					0.36
472	193.7	4.005967271					0.35
474	195.4	3.931148192					0.26
476	197.3	6.174499025					0.38
478	199.8	4.059452683					0.28
480	201.9	4.284972696					0.28
482	203.7	5.658893593					0.31
484	205.4	4.094308243					0.26
486	207.2	4.438613537					0.30
488	209.6	4.863631037					0.32
490	210.9	4.783439275					0.30
492	211.8	4.641687735					0.37
494	212.5	4.333684065					0.29
496	213.3	3.998338206					0.45
498	213.9	5.287128619					0.36
500	214.6	5.138802615					0.50
502	215.3	3.939675073					0.41
504	215.9	6.091857499					0.61
506	216.6	3.491811754					0.38
508	217.3	4.815046255					0.28
512	218.9	3.66858071					0.35
514	220.0	3.664167818					0.31
518	223.1	3.382122698					0.30

Table C.7: Age-depth and U/Th series data for ML1208 Site 17PC continued

Depth	Age	$^{230}Th_{xs,0}$	Mass Flux	^{232}Th	^{232}Th Flux	Dust Flux	aU
(cm)	(ka)	(dpm g^{-1})	(g cm^{-2} kyr^{-1})	(dpm g^{-1})	(μg cm^{-2} kyr^{-1})	(g m^{-2} yr^{-1})	(ppm)
520	224.2	3.635421667					0.36
520	224.2	3.266305901					0.30
522	225.2	3.212741332					0.34
524	226.1	3.460126499					0.40
526	227.1	3.591551769					0.42
526	227.1	3.582576133					0.31
528	228.1	3.379786682					0.43
530	229.2	3.644283653					0.49
532	230.5	3.80135563					0.49
534	232.5	3.987320525					0.47
535	233.3	4.355677137					0.50
536	233.9	4.279010615					0.54
537	234.4	4.039338605					0.52
538	235.0	3.930283461					0.59
539	235.5	4.296619005					0.62
540	236.0	3.781663572					0.59
541	236.5	4.008554576					0.62
542	237.0	4.289968515					0.63
543	237.5	4.392362909					0.55
544	238.0	3.83633962					0.61
545	238.5	3.931421785					0.61
546	239.0	3.95229819					0.59
547	239.5	3.68260656					0.55
548	240.1	3.876221398					0.59
549	240.7	3.527732369					0.50
550	241.5	3.878821124					0.51
551	242.5	3.557630129					0.44
552	243.3	3.203792061					0.39
553	243.8	3.343759406					0.38
554	244.3	2.906204365					0.33
555	244.7	3.131342596					0.35
556	245.1	3.023685871					0.32
557	245.5	2.979854449					0.30
558	245.8	3.052350936					0.30
559	246.2	3.08349623					0.30
560	246.5	2.876843377					0.29
561	246.9	2.914626886					0.28
562	247.2	3.123392081					0.31
563	247.5	3.09234046					0.32
564	247.8	2.567001225					0.32
565	248.2	2.720356391					0.36
566	248.5	2.698829082					0.39
567	248.8	2.767179527					0.42
568	249.2	2.700315612					0.46
569	249.5	2.58544759					0.53

Table C.8: Age-depth and U/Th series data for ML1208 Site 17PC continued

Depth	Age	$^{230}Th_{xs,0}$	Mass Flux	^{232}Th	^{232}Th Flux	Dust Flux	aU
(cm)	(ka)	(dpm g^{-1})	(g cm^{-2} kyr^{-1})	(dpm g^{-1})	(μg cm^{-2} kyr^{-1})	(g m^{-2} yr^{-1})	(ppm)
570	249.8	2.474014597					0.53
571	250.2	2.536944709					0.65
572	250.5	2.371258379					0.73
573	250.9	2.347923242					0.77
574	251.3	2.583313166					0.94
575	251.7	3.62548054					1.02
576	252.2	4.378231966					1.13
577	252.7	4.684405096					1.25
578	253.4	4.588150535					1.34
579	254.2	4.470635056					1.46
580	254.7	4.252025113					1.38
582	255.5	3.223895577					1.31
584	256.2	2.667587123					1.29
586	256.8	2.153309906					1.00
588	257.4	1.931308995					0.95
590	257.9	2.098661159					0.78
592	258.5	2.441935348					0.70
594	259.1	2.104671046					0.54
596	259.7	2.342659478					0.53
598	260.2	2.379585948					0.53
600	260.8	2.50916778					0.64
602	261.4	2.756257447					0.76
604	262.0	2.992745937					0.90
606	262.7	3.001714446					1.00
608	263.4	3.024002442					1.19
610	264.4	3.531432484					1.31
612	266.2	5.67727878					1.53
614	267.5	5.475854215					1.71
616	268.6	5.413308454					1.99
618	269.6	2.448470966					1.11
620	270.7	3.300250612					1.39
622	271.7	3.13010254					1.21
624	272.8	1.264692327					0.92
626	274.1	1.7815421					0.74
628	276.2	1.807316437					0.51
630	278.2	2.216412191					0.37
632	279.9	2.282803046					0.31
634	281.5	2.379479867					0.29
636	283.1	2.255131459					0.25
638	284.9	2.348595539					0.24
640	287.4	2.723583394					0.26
642	290.3	2.160432058					0.23
644	292.9	2.772509021					0.29
646	295.6	2.582490214					0.31
648	298.8	2.826490455					0.29

Table C.9: Age-depth and U/Th series data for ML1208 Site 17PC continued

Depth	Age	$^{230}Th_{xs,0}$	Mass Flux	^{232}Th	^{232}Th Flux	Dust Flux	aU
(cm)	(ka)	(dpm g^{-1})	(g cm^{-2} kyr^{-1})	(dpm g^{-1})	(μg cm^{-2} kyr^{-1})	(g m^{-2} yr^{-1})	(ppm)
650	301.2	2.428623993					0.28
652	303.3	2.06990015					0.25
654	305.6	2.162362654					0.24
656	308.5	4.790991071					0.48
658	310.8	6.795438097					0.62
660	312.7	2.864758883					0.31
662	314.6	2.791120075					0.35
664	316.6	2.648302036					0.37
666	319.4	2.612581611					0.47
668	321.4	2.406681026					0.73
670	323.1	3.006013395					0.74
671	323.8	3.334814154					0.74
672	324.6	3.19264668					0.70
673	325.4	4.132923743					0.84
674	326.2	3.14460229					0.82
675	327.1	3.014754497					0.74
676	328.0	2.229671017					0.72
677	329.2	2.418205713					0.67
678	330.1	2.534885949					0.61
679	330.5	2.722552009					0.54
680	330.9	2.149602538					0.47
681	331.2	2.132997627					0.43
682	331.5	1.898757276					0.40
683	331.8	1.948053073					0.39
684	332.1	1.810071784					0.39
685	332.4	1.571948378					0.37
686	332.6	1.72498868					0.37
687	332.9	1.548462854					0.33
688	333.1	1.787639579					0.34
689	333.4	1.521664713					0.33
690	333.6	1.665782007					0.33
691	333.9	1.841355904					0.34
692	334.1	2.014125308					0.35
693	334.3	1.695122001					0.35
694	334.6	1.610347085					0.40
695	334.8	1.699577128					0.43
696	335.0	1.638098389					0.43
697	335.3	1.530086855					0.48
698	335.5	1.095918832					0.48
699	335.8	0.900431696					0.54
700	336.0	0.968629515					0.58
701	336.2	0.786178338					0.58
702	336.5	0.831109322					0.56
703	336.7	1.040801612					0.71
704	337.0	1.463466096					0.73
705	337.2	3.653631329					0.82

Table C.10: Age-depth and U/Th series data for ML1208 Site 17PC continued

Depth	Age	$^{230}Th_{xs,0}$	Mass Flux	^{232}Th	^{232}Th Flux	Dust Flux	aU
(cm)	(ka)	(dpm g^{-1})	(g cm^{-2} kyr^{-1})	(dpm g^{-1})	(μg cm^{-2} kyr^{-1})	(g m^{-2} yr^{-1})	(ppm)
706	337.5	4.010786628					0.86
707	337.7	3.574908805					0.95
708	338.0	4.310827868					0.97
709	338.3	2.895656071					1.00
710	338.6	3.096605775					0.99
711	338.9	3.610296246					0.97
712	339.2	3.175657273					0.98
713	339.5	1.282172418					1.02
714	339.9	1.33258124					0.94
715	340.3	1.193914216					0.91
716	341.0	1.354113743					0.90
717	341.8	1.530934482					0.91
718	342.4	1.410048741					0.87
719	342.9	2.833028392					0.83